Monthly Notices of the ROYAL ASTRONOMICAL SOCIETY

MNRAS **535,** 471–515 (2024) https://doi.org/10.1093/mnras/stae2270
Advance Access publication 2024 October 3

The Type I superluminous supernova catalogue I: light-curve properties, models, and catalogue description

Sebastian Gomez ,[1★] Matt Nicholl ,[2★] Edo Berger ,[3,4] Peter K. Blanchard ,[3,5] V. Ashley Villar ,[3,4] Sofia Rest ,[6] Griffin Hosseinzadeh ,[7] Aysha Aamer ,[2] Yukta Ajay ,[6] Wasundara Athukoralalage ,[3] David C. Coulter ,[1] Tarraneh Eftekhari ,[5†] Achille Fiore ,[8,9] Noah Franz ,[7] Ori Fox ,[1] Alexander Gagliano ,[3,4] Daichi Hiramatsu ,[3,4] D. Andrew Howell ,[10,11] Brian Hsu ,[7] Mitchell Karmen ,[6] Matthew R. Siebert ,[1] Réka Könyves-Tóth ,[12,13,14,15] Harsh Kumar ,[3,4] Curtis McCully ,[10] Craig Pellegrino ,[16] Justin Pierel ,[1‡] Armin Rest [6,1] and Qinan Wang [6]

[1]*Space Telescope Science Institute, 3700 San Martin Drive, Baltimore, MD 21218, USA*
[2]*Astrophysics Research Centre, School of Mathematics and Physics, Queen's University Belfast, Belfast BT7 1NN, UK*
[3]*Center for Astrophysics | Harvard & Smithsonian, 60 Garden Street, Cambridge, MA 02138-1516, USA*
[4]*The NSF AI Institute for Artificial Intelligence and Fundamental Interactions, Cambridge, MA 02138, USA*
[5]*Center for Interdisciplinary Exploration and Research in Astrophysics (CIERA) and Department of Physics and Astronomy, Northwestern University, Evanston, IL 60208, USA*
[6]*Department of Physics and Astronomy, Johns Hopkins University, 3400 North Charles Street, Baltimore, MD 21218, USA*
[7]*Steward Observatory, University of Arizona, 933 North Cherry Avenue, Tucson, AZ 85721, USA*
[8]*Institut für Theoretische Physik, Goethe Universität, Max-von-Laue-Straße 1, D-60438 Frankfurt am Main, Germany*
[9]*INAF – Osservatorio Astronomico di Padova, Vicolo dell'Osservatorio 5, I-35122 Padova, Italy*
[10]*Las Cumbres Observatory, 6740 Cortona Drive, Suite 102, Goleta, CA 93117-5575, USA*
[11]*Department of Physics, University of California, Santa Barbara, CA 93106-9530, USA*
[12]*Konkoly Observatory, Research Center for Astronomy and Earth Sciences, MTA Centre of Excellence, Konkoly Thege Miklos út 15-17., H-1121 Budapest, Hungary*
[13]*CSFK, MTA Centre of Excellence, Konkoly Thege út 15-17., H-1121 Budapest, Hungary*
[14]*Department of Experimental Physics, Institute of Physics, University of Szeged, Dóm tér 9, Szeged 6720, Hungary*
[15]*Gothard Astrophysical Observatory, ELTE Eötvös Loránd University, Szombathely, Hungary*
[16]*Department of Astronomy, University of Virginia, Charlottesville, VA 22904, USA*

Accepted 2024 September 19. Received 2024 August 29; in original form 2024 July 11

ABSTRACT

We present the most comprehensive catalogue to date of Type I superluminous supernovae (SLSNe), a class of stripped-envelope supernovae (SNe) characterized by exceptionally high luminosities. We have compiled a sample of 262 SLSNe reported through 2022 December 31. We verified the spectroscopic classification of each SLSN and collated an exhaustive data set of ultraviolet, optical, and infrared photometry totalling over 30 000 photometric detections. Using these data, we derive observational parameters such as the peak absolute magnitudes, rise and decline time-scales, as well as bolometric luminosities, temperature, and photospheric radius evolution for all SLSNe. Additionally, we model all light curves using a hybrid model that includes contributions from both a magnetar central engine and the radioactive decay of ^{56}Ni. We explore correlations among various physical and observational parameters, and recover the previously found relation between ejecta mass and magnetar spin, as well as the overall progenitor pre-explosion mass distribution with a peak at ≈ 6.5 M$_\odot$. We find no significant redshift dependence for any parameter, and no evidence for distinct subtypes of SLSNe. We find that only a small fraction of SLSNe, < 3 per cent, are best fit with a significant radioactive decay component $\gtrsim 50$ per cent. We provide several analytical tools designed to simulate typical SLSN light curves across a broad range of wavelengths and phases, enabling accurate *K*-corrections, bolometric scaling calculations, and inclusion of SLSNe in survey simulations or future comparison works.

Key words: astronomical data bases: surveys – stars: early type – transients: supernovae.

1 INTRODUCTION

Core-collapse supernovae (CCSNe) result from the deaths of massive stars with zero-age main-sequence (ZAMS) masses $\gtrsim 8\,\mathrm{M}_\odot$

★ E-mail: sgomez@cfa.harvard.edu (SG); M.Nicholl.1@bham.ac.uk (MN)
† NHFP Einstein Fellow.
‡ NHFP Einstein Fellow.

(Woosley & Weaver 1986). Some of these massive stars lose their hydrogen, and in some cases helium, envelopes before undergoing core-collapse, which can lead to either a Type Ib SN if the star is deprived of hydrogen, or a Type Ic/Ic broad-lined (BL) SN if it has lost both its hydrogen and helium (Woosley, Langer & Weaver 1995; Filippenko 1997). Given their light-curve evolution and spectral properties, it has been established that non-interacting stripped-envelope SNe (SESNe) are powered by the radioactive decay of ^{56}Ni synthesized during the explosion (Arnett 1982).

Over a decade ago, a new class of SESNe was discovered and dubbed Type I superluminous SNe (SLSNe), given a lack of hydrogen in their spectra and luminosities up to 100 times larger than normal SESNe (Chomiuk et al. 2011; Quimby et al. 2011c; Gal-Yam 2012, 2019c; Howell 2017; Moriya, Sorokina & Chevalier 2018b). Unlike normal SNe Ib/c, SLSNe cannot be powered by radioactive decay alone, but instead require an additional or alternative power source (Dessart et al. 2012; Inserra et al. 2013; Nicholl et al. 2013; Sukhbold & Woosley 2016; Blanchard et al. 2018c; Margalit et al. 2018a). Possible alternative models include the pair-instability or pulsational pair-instability (PISN or PPISN) mechanism (Heger & Woosley 2002; Woosley, Blinnikov & Heger 2007; Gal-Yam et al. 2009; Kasen, Woosley & Heger 2011; Kozyreva & Blinnikov 2015; Woosley 2017), interaction with circumstellar material (CSM) around the progenitor star (Chevalier & Irwin 2011; Chatzopoulos et al. 2013; Vreeswijk et al. 2017; Yan et al. 2017b), a contribution from jet launching (Soker & Gilkis 2017; Soker 2022), energy injected from a central engine such as a millisecond magnetar (e.g. Kasen & Bildsten 2010; Woosley 2010; Inserra et al. 2013; Chen et al. 2015; Wang et al. 2015; Mazzali et al. 2016; Jerkstrand et al. 2017; Liu, Modjaz & Bianco 2017; Nicholl, Guillochon & Berger 2017c; Yu et al. 2017; De Cia et al. 2018; Dessart 2019; Blanchard et al. 2021c; Lin et al. 2020a; Hsu, Hosseinzadeh & Berger 2021; Omand & Jerkstrand 2023), or fallback accretion from a black hole (Dexter & Kasen 2013; Kasen, Metzger & Bildsten 2016; Moriya, Nicholl & Guillochon 2018a). It has also been suggested that some or all SLSNe could be powered by a combination of these models (Wang et al. 2016; Inserra et al. 2017; Chen et al. 2017b, 2023a, b; Gomez et al. 2022a). These SNe are distinct from the similarly named Type II SLSNe, which are likely powered by the interaction with high amounts of CSM (e.g. Smith et al. 2007; Inserra et al. 2018a; Kangas et al. 2022; Pessi et al. 2024). On this work, we focus exclusively on the hydrogen-poor SLSNe.

As SLSNe fade, their spectra tend to resemble those of SNe Ic and SNe Ic-BL, suggesting these populations are closely related (Pastorello et al. 2010; Inserra et al. 2013; Jerkstrand et al. 2017; Quimby et al. 2018; Blanchard et al. 2019; Nicholl et al. 2019a). In Gomez et al. (2022a), we showed how luminous supernovae (LSNe), or SESNe with peak magnitudes between those of SNe Ic/Ic-BL and SLSNe covering the range of $M_r = -19$ to -20 mag, are likely powered by a combination of a magnetar central engine and radioactive decay (Prentice et al. 2021).

Besides their power source, there are several areas of active investigation regarding the nature of SLSNe, including their spectroscopic and photometric diversity (Nicholl et al. 2015b; Inserra et al. 2017, 2018a; Gal-Yam 2019a; Könyves-Tóth et al. 2020; Könyves-Tóth & Seli 2023), progenitors (Lunnan et al. 2015; Aguilera-Dena et al. 2018; Blanchard et al. 2020b), connection to other transients (Justham, Podsiadlowski & Vink 2014; Greiner et al. 2015; Japelj et al. 2016; Metzger, Berger & Margalit 2017; Margutti et al. 2018; Margalit et al. 2018b; Eftekhari et al. 2021; Gomez et al. 2021c, 2022a; Liu et al. 2022), studies of their environments and host galaxies (Neill et al. 2011; Lunnan et al. 2014; Leloudas et al. 2015b; Angus et al. 2016; Perley et al. 2016; Chen et al. 2017a; Hatsukade et al. 2018; Schulze et al. 2018; Ørum et al. 2020; Hsu et al. 2024), whether they can be used as cosmological probes (Inserra & Smartt 2014; Scovacricchi et al. 2016; Hsu et al. 2021; Inserra et al. 2021), how to find them in large surveys (Tanaka et al. 2012; Villar, Nicholl & Berger 2018; Hsu et al. 2022; Hosseinzadeh et al. 2020; Villar et al. 2020; Gagliano et al. 2023; Gomez et al. 2023b; Sheng et al. 2024), and analyses of early- and late-time 'bumps' in their light curves (Hosseinzadeh et al. 2022; Moriya et al. 2022a; Dong et al. 2023; Zhu et al. 2024). Some of these topics have been addressed in studies of large samples of SLSNe (Nicholl et al. 2015b, 2017c; Perley et al. 2016; De Cia et al. 2018; Liu et al. 2017; Quimby et al. 2018; Lunnan et al. 2018c; Angus et al. 2019; Hinkle, Shappee & Tucker 2023), with the largest study totalling 78 events (Chen et al. 2023a, b). Here, we provide a compilation that is not limited to a single survey, but encompasses the full parameter space of known SLSNe with a sample size more than triple that of the previous largest sample.

In this work, we include all known SLSNe discovered any time before 31 December 2022, totalling 262 events. We verify their spectroscopic classification as SLSNe, and include all their publicly available photometry, in addition to photometry from our own Finding Luminous and Exotic Extragalactic Transients (FLEET) follow-up program (Gomez et al. 2020a, 2023a). We model their light curves with a magnetar plus radioactive decay model, and provide both physical and observational parameters for the entire sample. This represents the first data release (DR1) of what will be a series of data releases on SLSNe, including a study on the photospheric spectra of SLSNe (Aamer et al., in preparation) and their late-time nebular spectra (Blanchard et al., in preparation). All data and products are publicly available on GitHub[1] and Zenodo (Gomez 2024). The GitHub repository also contains PYTHON scripts that can be used to either reproduce the plots in this paper, or to include the parameters of all known SLSNe in other works. We provide a `get_references` function that we encourage users to use to obtain and cite the original sources of data used in this work.

The structure of this paper is as follows. In Section 2, we describe the sample of SLSNe and how their data were compiled. In Section 3, we present our light-curve modelling and population properties, and describe the results of this analysis in Sections 4 and 5. We outline the main conclusions in Section 6. In Section 7, we include a detailed description of the open-source catalogue and PYTHON examples on how to use the tools provided. In the appendices, we include details about each SN used in this sample. Magnitudes referenced in this paper are quoted in the AB system unless otherwise stated. Throughout the paper, we assume a flat lamda-cold dark matter cosmology based on the Planck 2018 results with $H_0 = 67.8$ km s^{-1} Mpc^{-1} and $\Omega_m = 0.308$ (Planck Collaboration VI 2020).

2 SLSN SAMPLE AND DATA

2.1 Sample definition

We compile a sample of all known SLSNe discovered before 31 December 2022, and aim to include all their available photometry. The SNe in this sample are compiled from the Open Supernova Catalog[2] (OSC; Guillochon et al. 2017), the Transient Name Server

[1] https://github.com/gmzsebastian/SLSNe
[2] https://github.com/astrocatalogs/supernovae

(TNS),[3] the List of SLSNe,[4] the Weizmann Interactive Supernova Data Repository (WISeREP; Yaron & Gal-Yam 2012),[5] a literature search, and our FLEET follow-up program (Gomez et al. 2020a, 2023a). We include every object that has ever been claimed to be an SLSN in any of these sources. For a sample of SNe that include ambiguous objects that lie in between SLSNe and normal Type Ib/c SNe, see Gomez et al. (2022a).

To confirm their nature as SLSNe we require at least one public spectrum for each SN. We obtain these spectra from either the OSC, TNS, WISeREP, published works, or our FLEET program. To verify that the SNe in this sample are consistent with being SLSNe we visually match their spectra to reference spectra from known SLSNe. Special care is taken for SNe that have not yet been presented in a refereed publication. We show the spectra of all 54 unpublished SLSNe, as well as their best-matching templates in Fig. 1. The individual references for the spectra used are listed in the appendices. We divide the sample of 262 SNe into 168 'gold', 70 'silver', and 24 'bronze' SLSNe. Gold SLSNe have spectra consistent with an SLSN and photometry available before and after peak in more than one band. We list the conditions that lead to a silver or bronze label in Table 1 and all SLSNe sorted under these three quality labels in the appendices.

In addition to the sample of confirmed SLSNe, we include a list of nine objects that have been previously suggested to be SLSNe, but which we argue are likely not SLSNe. These objects, along with the list of all SLSNe are included in the appendices with individual notes on each object, including their peculiarities, as well as the sources of their discovery and data. In Fig. 2, we show a histogram of all SLSNe included in this work (gold, silver, and bronze) as a function of their discovery year. The number of SLSNe discovered after 2022 declined since both the FLEET and Zwicky Transient Facility (ZTF) follow-up programs decreased their focus on classifying SLSNe after this point. For all subsequent analyses and plots, we include only the 238 gold and silver SLSNe and refer to this as the 'full sample' or 'all SLSNe', unless otherwise stated.

2.2 Photometry

We compiled ultraviolet (UV), optical, and infrared (IR) photometry of all SLSNe from a variety of sources. Photometry from the ZTF (Bellm et al. 2019; Graham et al. 2019) is taken either from the public archive using alert photometry form the Automatic Learning for the Rapid Classification of Events broker (Förster et al. 2021), or from our own photometry done on raw ZTF images obtained from the NASA/IPAC Infrared Science Archive.[6] We include photometry from the Asteroid Terrestrial-impact Last Alert System (ATLAS; Tonry et al. 2018; Smith et al. 2020), the All Sky Automated Survey for SuperNovae (ASAS-SN; Shappee et al. 2014; Kochanek et al. 2017; Hart et al. 2023), the *Gaia Science* Alerts (GSA; Wyrzykowski 2016), the Optical Gravitational Lensing Experiment (OGLE; Wyrzykowski et al. 2014), the Catalina Real Time Transient Survey (CRTS; Drake et al. 2009a), the Pan-STARRS Survey for Transients (Huber et al. 2015), the Dark Energy Survey (DES; Angus et al. 2019), and the Swift Optical/Ultraviolet Supernova Archive (SOUSA; Brown et al. 2014). In addition to data available from public repositories, we collect photometry from individual publications that have these data available, either from the supplementary materials of their journals, the TNS, WISeREP, the OSC, or private communication with the authors. The individual data sources, as well as any details pertaining to the photometry of each individual SN are listed in the appendices.

Additionally, we include photometry from our FLEET follow-up program (Gomez et al. 2020a, 2023a). Images from this program were taken with either the KeplerCam imager on the 1.2-m telescope at the Fred Lawrence Whipple Observatory (FLWO), the Low Dispersion Survey Spectrograph (LDSS3C; Stevenson et al. 2016) or Inamori–Magellan Areal Camera and Spectrograph (IMACS; Dressler et al. 2011), both on the Magellan Clay 6.5-m telescopes at Las Campanas Observatory, or Binospec (Fabricant et al. 2019) on the MMT 6.5-m telescope. We also include *gri* images taken by the Global Supernova Project (GSP) with the Las Cumbres Observatory's global telescope network (Las Cumbres; Brown et al. 2013).

We perform photometry on all images in a uniform way. Instrumental magnitudes were measured by modelling the point spread function (PSF) of each image using field stars and fitting the model PSF to the target. The magnitudes are then calibrated to AB magnitudes from the PS1/3π catalogue (Chambers et al. 2016). For the majority of sources, we separate the flux of the SN from its host galaxy by doing difference imaging using a pre-explosion PS1/3π template for comparison. We subtract the PS1/3π template from the science images using HOTPANTS (Becker 2015). There are 13 sources that lie outside the PS1/3π footprint. For these, we use photometry exclusively from either previously published works that accounted for the contribution of the host, or difference photometry from ATLAS or OGLE. To process the ATLAS photometry, we use `ATClean`, a new pipeline designed to use the fluxes and uncertainties from the ATLAS forced photometry service (Shingles et al. 2021) to produce binned and statistically cleaned photometry (Rest et al. 2024). For some sources, we determine the host galaxy contribution to be negligible and report PSF photometry taken directly from the science images without subtracting a template. Notes on the data reduction procedure for individual SN are listed in the appendices.

For the photometry that is not corrected for foreground Milky Way extinction, we correct it using the dust maps from Schlafly & Finkbeiner (2011) and the ASTROPY (Astropy Collaboration 2018) implementation of the Gordon et al. (2023) extinction law. This recent extinction law measurement represents the only one that provides accurate measurements extending from 912 Å to 32 μm (Gordon, Cartledge & Clayton 2009; Fitzpatrick et al. 2019; Gordon et al. 2021; Decleir et al. 2022), with the most significant deviations from the more commonly used (Cardelli, Clayton & Mathis 1989) extinction law occurring in the IR, above $\sim 1\mu$m. In a few cases, the existing SLSN photometry is already provided corrected for extinction, in which case we do not apply any additional corrections. We do not include photometry that is already corrected for intrinsic host galaxy extinction, but instead leave this as a free parameter in our models.

In Fig. 3, we show a 2D histogram of all detections of the full sample as a function of rest-frame wavelength and phase. Throughout this work, we define phase as rest-frame days from observed r-band peak, unless otherwise stated. The histogram contains more than 33 265 detections for the 238 SLSNe in the full sample. We include lines to demarcate the 1st and 99th percentile coverage in terms of wavelength and phase. While there are ample optical observations of SLSNe during peak, there are very few observations of SLSNe bluewards of 1900 Å, redwards of 8600 Å, or later than 320 d after

[3] https://www.wis-tns.org/
[4] https://slsn.info/
[5] https://www.wiserep.org/
[6] https://irsa.ipac.caltech.edu/Missions/ztf.html

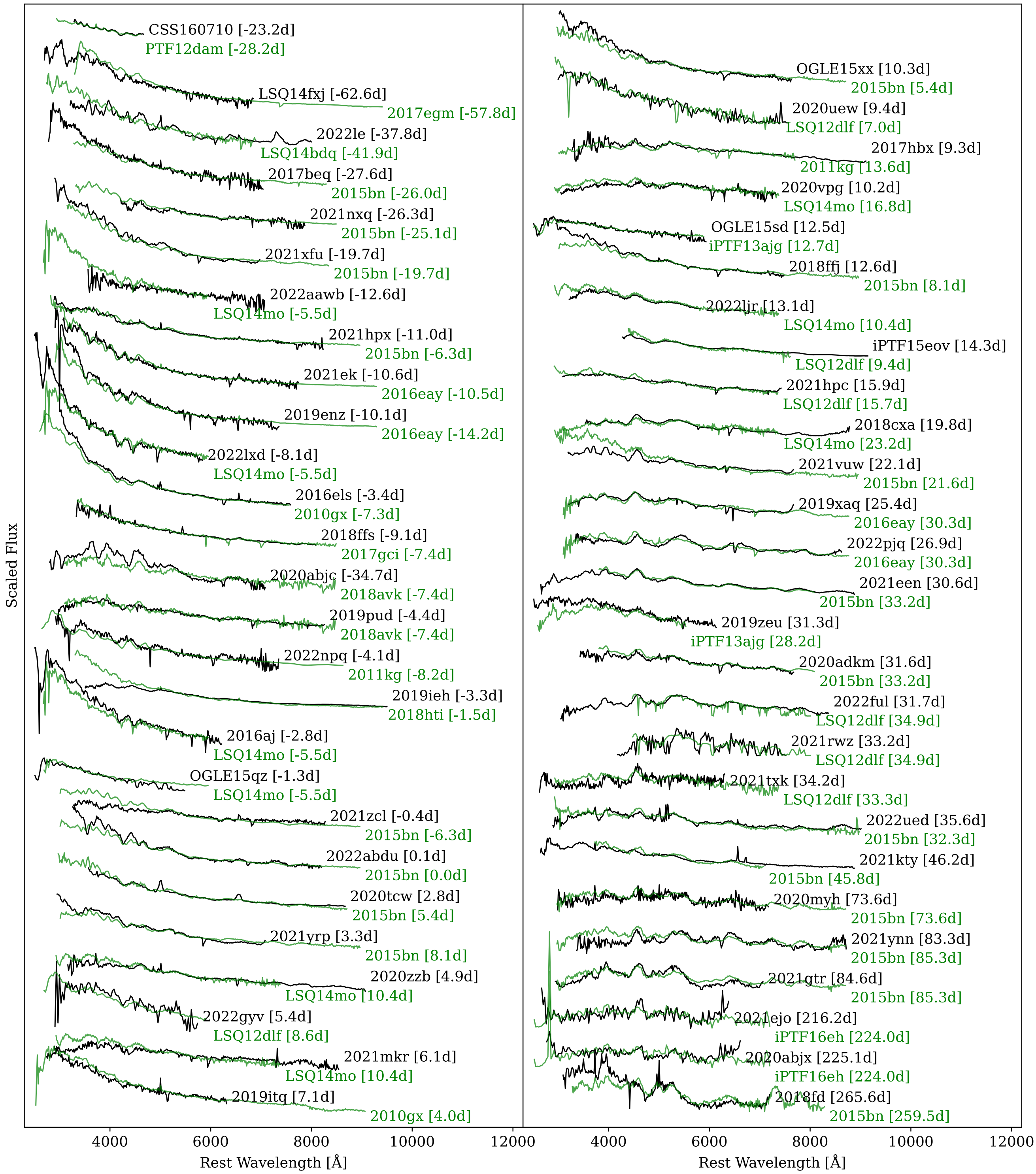

Figure 1. A representative spectrum for each SLSN in our sample that has not yet been presented in a refereed publication is shown in black, along with the corresponding best-matching spectrum from known SLSNe in green, used to verify their classification. The phase in brackets represents rest-frame days from peak. Individual sources and references for each SLSN are listed in the appendices.

peak. The sample has a mean value of 130 detections per SN, and a median of 78.

The peak of the redshift distribution of the full sample of SLSNe is $z \approx 0.26$, which depends on the depth of the surveys finding these SLSNe. Most SLSNe were discovered by relatively shallow surveys like ZTF and ATLAS, which have a magnitude limit of $m_r \sim 20.5$, and only a few SLSNe were found by deeper surveys like DES or the PS1 Medium Deep Survey (MDS; McCrum et al. 2015; Lunnan et al. 2018c), which have a limit of $m_r \sim 23.5$. In Fig. 4, we show the peak absolute magnitude in r band of the full

Table 1. SLSNe label criteria.

Criteria	Objects
Gold	
Spectrum consistent with an SLSN and multiband photometry before and after peak	(168) : 2005ap, 2007bi, 2009jh, 2010gx, 2010hy, 2010kd, 2010md, 2011ke, 2011kg, 2012il, 2013dg, 2015bn, 2016ard, 2016eay, 2016inl, 2017dwh, 2017egm, 2017ens, 2017gci, 2018avk, 2018bgv, 2018bsz, 2018bym, 2018cxa, 2018ffj, 2018ffs, 2018gbw, 2018gft, 2018hpq, 2018hti, 2018ibb, 2018kyt, 2018lfd, 2018lfe, 2018lzv, 2018lzx, 2019aamp, 2019aamq, 2019aamr, 2019aams, 2019aamt, 2019aamu, 2019aamv, 2019aamx, 2019bgu, 2019cca, 2019cdt, 2019cwu, 2019dgr, 2019dlr, 2019enz, 2019eot, 2019gfm, 2019gqi, 2019hno, 2019itq, 2019kcy, 2019kwq, 2019kws, 2019kwt, 2019kwu, 2019lsq, 2019neq, 2019nhs, 2019otl, 2019pud, 2019qgk, 2019sgg, 2019sgh, 2019szu, 2019ujb, 2019vvc, 2019xaq, 2019xdy, 2019zbv, 2019zeu, 2020abjc, 2020adkm, 2020afag, 2020afah, 2020ank, 2020aup, 2020auv, 2020dlb, 2020exj, 2020fvm, 2020htd, 2020iyj, 2020jii, 2020kox, 2020qef, 2020qlb, 2020rmv, 2020tcw, 2020uew, 2020vpg, 2020wnt, 2020xga, 2020xgd, 2020xkv, 2020zbf, 2020znr, 2020zzb, 2021bnw, 2021een, 2021ejo, 2021ek, 2021fpl, 2021gtr, 2021hpc, 2021hpx, 2021kty, 2021mkr, 2021nxq, 2021txk, 2021vuw, 2021xfu, 2021ynn, 2021yrp, 2021zcl, 2022abdu, 2022ful, 2022le, 2022ljr, 2022lxd, 2022npq, 2022pjq, 2022ued, DES14S2qri, DES14X2byo, DES14X3taz, DES15E2mlf, DES15X1noe, DES15X3hm, DES16C2aix, DES16C3dmp, DES17X1amf, DES17X1blv, iPTF13ajg, iPTF13ehe, iPTF15eov, iPTF16eh, LSQ12dlf, LSQ14bdq, LSQ14mo, OGLE15qz, PS110awh, PS110bzj, PS110ky, PS110pm, PS111afv, PS111aib, PS111ap, PS111bdn, PS112bqf, PS112cil, PS113or, PS114bj, PS15cjz, PTF09atu, PTF09cnd, PTF10uhf, PTF10vqv, PTF12dam, PTF12mxx, SCP06F6, SNLS06D4eu, and SNLS07D2bv
Silver	
No photometry before or after peak	(26): 1999as, 2002gh, 2006oz, 2011kf, 2016aj, 2016els, 2016wi, 2018fd, 2018gkz, 2018lzw, 2020myh, DES16C2nm, DES16C3ggu, iPTF13bdl, iPTF13bjz, iPTF13cjq, iPTF13dcc, iPTF16bad, LSQ14an, PS110ahf, PS111bam, PS112bmy, PS113gt, PTF10bfz, PTF10nmn, and SSS120810
Source was also classified as an LSN	(21): 1991D, 2009cb, 2011kl, 2012aa, 2013hy, 2018beh, 2019dwa, 2019gam, 2019hge, 2019ieh, 2019J, 2019obk, 2019pvs, 2019unb, 2020fyq, 2021lwz, DES14C1rhg, DES15C3hav, iPTF16asu, PTF12gty, and PTF12hni
Spectra have low signal-to-noise ratio but are consistent with an SLSN	(12): 2019aamw, 2020abjx, 2021rwz, 2022aawb, DES14C1fi, DES14E2slp, DES15S1nog, DES17C3gyp, PS111tt, PTF10aagc, PTF10iam, and SNLS07D3bs
Photometry is only available in one band	(7): 2017jan, CSS160710, OGLE15sd, OGLE15xl, OGLE15xx, OGLE16dmu, and PTF10bjp
Redshift is uncertain, but the closest estimate implies a peak absolute magnitude brighter than $M_r = -20$ mag	(2): 2017hbx and 2022gyv
Signs of high extinction with an uncertain measurement	(2): 2018don and 2020onb
Bronze	
There are no public spectra of the source available	(12): 2011ep, 2018hsf, 2018jfo, 2020aewh, 2020wfh, CSS140925, MLS121104, PSNJ000123, SDSS17789, SN1000, SN2213, and UID30901
Previously classified as an SLSN, but more consistent with a SN Ic	(4): 2018fcg, 2021uvy, 2021ybf, and DES16C3cv
Redshift is uncertain, and the closest estimate implies a peak absolute magnitude dimmer than $M_r = -20$ mag	(2): 2019une and 2022ojm
Has less than three data points of photometry	(4): 1999bz, 2014bl, 2017beq, and LSQ14fxj
Spectroscopic classification cannot be accurately determined due to low signal-to-noise spectra	(2): ASASSN15no and PS112zn

Notes. We divide the full sample of SLSNe into a gold, silver, and bronze sample. All gold SLSNe have spectra that are consistent with an SLSN and photometry available before and after peak in more than one band. The criteria used to rank silver and bronze SNe are applied sequentially. Objects are listed under the first criterion that applies, with the number of objects that fall into each criterion in parenthesis.

sample as a function of redshift, with representative surveys marked with different colours. We derive the r-band maximum from models to the light curves, which are all measured in a uniform rest-frame r band and with both intrinsic and Milky Way extinction corrections applied. The sample of spectroscopically confirmed SLSNe does not extend down to the photometric limit of ~ 23.5 given that we are usually constrained by the shallower limit of spectroscopic observations. On the right panel of Fig. 4, we also show the total radiated energy during the first 200 d of the light curve as a function of redshift for the full sample. Of the full sample, 99 per cent of SLSNe have a total radiated energy $E_{\rm rad} < 4.7 \times 10^{51}$ erg, above which there is a sharp drop-off, seen in the histogram on the right panel of Fig. 4.

3 METHODS

3.1 Light-curve modelling

We model the light curves of all SLSNe using the Modular Open-Source Fitter for Transients (MOSFIT) package, a flexible PYTHON code that uses the EMCEE (Foreman-Mackey et al. 2013) implementation of Markov chain Monte Carlo to fit the light curves of transients

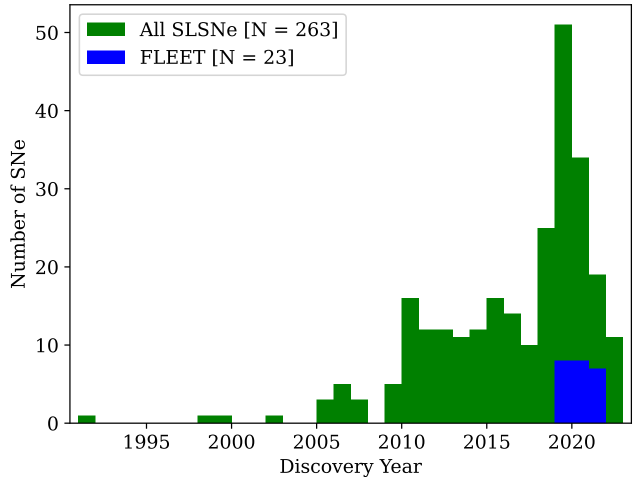

Figure 2. Histogram of the discovery year of all SLSNe in this work, including the bronze sample. In blue, we show the SLSNe discovered as part of our FLEET observational program, which contributed to the peak of SLSN discoveries in 2020–2022.

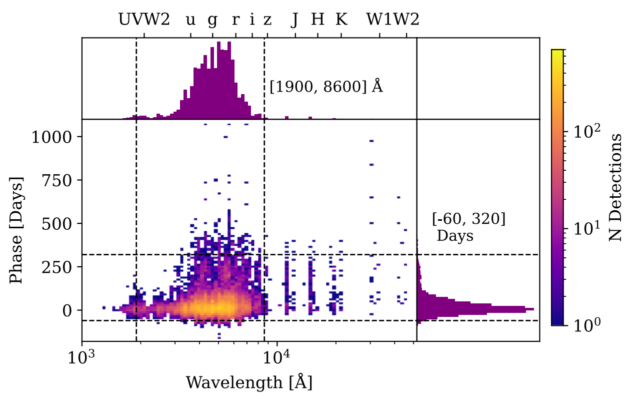

Figure 3. 2D histogram of rest-frame phase in days versus rest-frame wavelength for all photometric measurements of the full sample of SLSNe. The dashed lines represent the 1st and 99th percentile of each histogram, emphasizing the abundance of optical data within a few months of peak brightness.

using a variety of different power sources (Guillochon et al. 2018). Here, we assume a magnetar central engine to be the dominant power source of SLSNe. Additionally, we account for contributions from radioactive decay, recognized as the primary power source in Type Ic SNe, the less luminous analogues to SLSNe. The choice to model the light curves with a magnetar central engine comes from the fact that this model has been able to accurately reproduce the light curves (e.g. Nicholl et al. 2017c), late-time evolution (e.g. Kasen & Bildsten 2010), and spectra (e.g. Mazzali et al. 2016) of most SLSNe. A significant advantage of this model is its ability to replicate the light curves of SLSNe with a minimal set of parameters, particularly when compared to more complex models such as those powered by CSM interaction (e.g. Chevalier & Irwin 2011; Chatzopoulos et al. 2013; Chen et al. 2023b). Modelling the entire data set with distinct models is beyond the scope of this work. Regardless of the model choice, some physical parameters such as the ejecta mass and velocity, should still correlate with the diffusion time-scale, which is related to the duration of the light curve. Additionally, we use these models to derive model-independent properties from the light curves of SLSNe.

The parameters being fit in the models, their prior ranges, units, and definitions are listed in Table 2. The original magnetar model used in MOSFIT is defined in Nicholl et al. (2017c). The models, priors, and parameter constraints used here are identical to those used to model LSNe in Gomez et al. (2022a). The main difference from the original Nicholl et al. (2017c) models and the ones used to model LSNe is the inclusion of an additional radioactive decay component. We also allow for the suppression α of the flux bluewards of some wavelength λ_0 to vary between 0 and 5, as opposed to being fixed to 1. Given that the value of the neutron star mass $M_{\rm NS}$ has little to no effect on the output light curve, we impose a Gaussian prior of $M_{\rm NS} = 1.7 \pm 0.2\,{\rm M}_\odot$ motivated by the typical masses of neutron stars (Özel & Freire 2016). We run each model with 150 walkers and test for convergence by ensuring that the models reach a potential scale reduction factor of < 1.3 (Gelman & Rubin 1992), which corresponds to a few $\times 10^4$ steps, depending on the SN. We show the light curves and best-model fits of all Gold SLSNe in Fig. 5. We are able to reproduce the light curves of the full sample of SLSNe with this model. After accounting for the model variance σ, all SLSNe have a reduced χ^2 values less than 1.7.

We use the posterior distribution of all the best-fitting parameters from MOSFIT to calculate the values of additional physical parameters. We use the individual values of all walkers to obtain the most accurate estimate for the mean value and correlations between these derived parameters. We include measurements for the total nickel mass $M_{\rm Ni}$, as well as for the initial magnetar spin-down luminosity L_0 and spin-down time $t_{\rm SD}$. The latter two parameters are included to allow for a direct comparison to the model of Omand & Sarin (2024), where these parameters are defined. We also include a measurement of the kinetic energy, $\mathrm{KE} = (3/10) M_{\rm ej} V_{\rm ej}^2$, the radiative efficiency between luminosity L and kinetic energy $\epsilon = L/\mathrm{KE}$, and a measurement of $f_{\rm mag}$, or the fraction of the total luminosity during the first 200 d that comes from the magnetar contribution, as opposed to radioactive decay.

Lastly, we use the MOSFIT light-curve models to calculate a series of observational parameters. We provide rest-frame light curves for all SLSNe by generating MOSFIT models based on the best-fitting parameters of each SLSN, but at a fixed distance of 10 pc and with no host extinction. These models represent rest-frame SLSN light curves in $ugrizy$, UVBRIJHKs, and all *Swift* bands. We do not include models redder than $\lambda = 1.58\ \mu$m, since observations in these bands have been shown to be heavily affected by emission from dust (Chen et al. 2021; Sun, Xiao & Li 2022), and the models would therefore not be representative of real SLSN observations. We use these rest-frame models to measure values for Δm_{15}, the magnitudes by which an SN fades 15 d after maximum in B band; τ_e, the number of days it takes for an SN to fade from bolometric peak by a factor of e; τ_1, the number of days it takes for an SN to fade by 1 mag in r band; $\tau_{\rm rise}$, the number of days it takes an SN to go from explosion determined from the MOSFIT model to r-band peak; $M_{\rm max}$, the peak absolute magnitude in rest-frame r band; $L_{\rm max}$, the bolometric luminosity at peak; and $E_{\rm rad}$, the total radiated energy during the first 200 d after explosion.

3.2 EXTRABOL

To measure the bolometric properties of each SLSN, including their luminosities, temperatures, and radii, we model each light curve using EXTRABOL (Thornton et al. 2024), a Gaussian Process implementation of the GEORGE (Foreman-Mackey 2015) package,

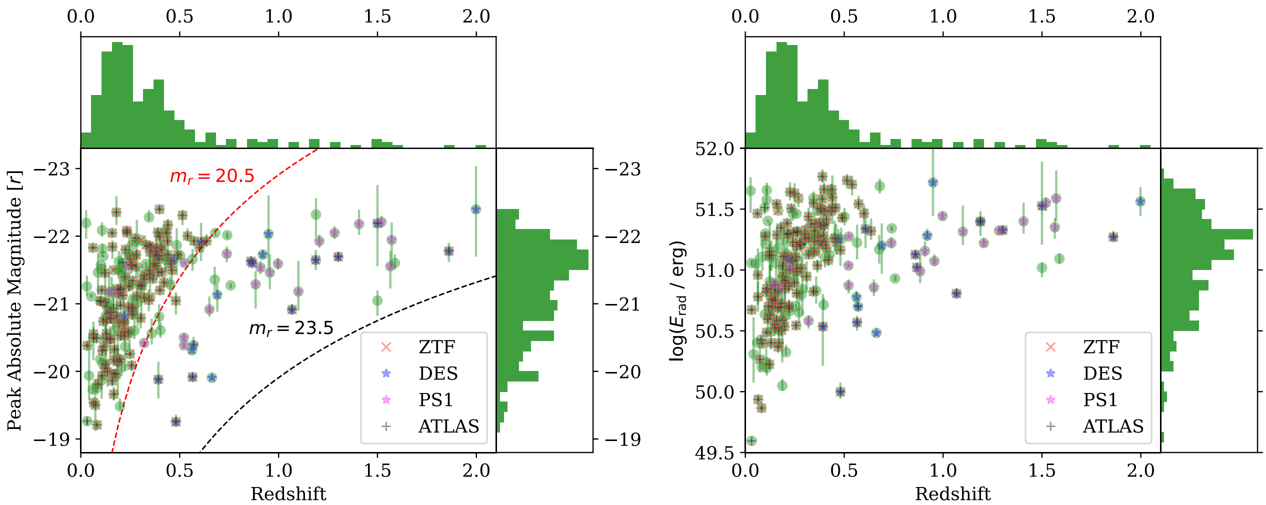

Figure 4. Left: peak absolute magnitude in rest-frame r band as a function of redshift for the full SLSN sample. In red, blue, and pink, we show SLSNe detected in several large surveys: ZTF, DES, and PS1, respectively. The red dashed line indicates the nominal magnitude limit of ZTF, and the black line the limit for PS1 and DES (we note that SLSNe from PS1 and DES are further limited by a rough spectroscopic follow-up limit of $\sim$ 22.5 mag). Right: total radiated energy $E_{\rm rad}$ during the first 200 d of the light curve for the full SLSN sample.

Table 2. MOSFIT parameter definitions.

	Prior	Units	Definition
$M_{\rm ej}$	[0.1, 100]	$M_\odot$	Ejecta mass
$f_{\rm Ni}$	log((0, 0.5])		Nickel mass as a fraction of the ejecta mass
$V_{\rm ej}$	log([10^3, 10^5])	km s^{-1}	Ejecta velocity
$M_{\rm NS}$	1.7 ± 0.2	$M_\odot$	Neutron star mass
$P_{\rm spin}$	[0.7, 30]	ms	Magnetar spin
$B_\perp$	log((0, 15])	10^{14} G	Magnetar magnetic field strength
$\theta_{\rm BP}$	[0, $\pi/2$]	rad	Angle of the dipole moment
$t_{\rm exp}$	[0, 200]	d	Explosion time relative to first data point
$T_{\rm min}$	[3000, 10000]	K	Photosphere temperature floor
λ_0	[2000, 6000]	Å	Flux below this wavelength is suppressed by α
α	[0, 5]		Slope of the wavelength suppression
$n_{H,\rm host}$	log([10^{16}, 10^{23}])	cm^{-2}	Column density in the host galaxy
κ	[0.01, 0.34]	cm^{2}g^{-1}	Optical opacity
κ_γ	log([0.01, 0.5])	cm^{2}g^{-1}	Gamma-ray opacity
σ	[10^{-3}, 10^2]		Uncertainty required for $\chi^2_r = 1$

Notes. Parameters used in the MOSFIT model, their priors, units, and definitions. Priors noted in log have a log-flat prior, priors without it are flat in linear space, and priors with a centre and error bars have a Gaussian distribution.

based on the original SUPERBOL (Nicholl 2018) code. Unlike MOSFIT, which produces smoothly evolving light curves, the EXTRABOL model allows us to account for short-term variability, such as bumps or undulations, that the MOSFIT model cannot reproduce. We limit the EXTRABOL models only to SLSNe that have at least three detections in three distinct bands to obtain a more robust fit to the data in terms of phase and wavelength. We find that EXTRABOL tends to overpredict UV magnitudes when no UV observations are available, particularly at very early or late phases. To mitigate this issue, we include additional model photometry derived from the MOSFIT model, corresponding to the model magnitude of the SN in every observed band at the time of the first and last detections. We find this addition helps EXTRABOL produce much more reliable results in the interpolation.

Additionally, we measure the rate of change of the photospheric radius as a function of phase by fitting a straight line to the EXTRABOL models from explosion to peak bolometric luminosity. We use this value to approximate the photospheric velocity of the SLSNe, and refer to it as the 'blackbody velocity' to distinguish it from a direct measurement of the photospheric velocity.

4 POPULATION PROPERTIES

In this section, we describe basic observational properties of the SLSN population based on the parameters described in Section 3. Since some of the properties described here, such as the peak luminosity or rise time, are derived from the light-curve models, we consider them to be largely model independent.

4.1 The mean SLSN

We use the rest-frame MOSFIT light-curve models of all SLSNe to create a map of their mean evolution as a function of phase and wavelength. The mean is calculated by averaging the magnitudes of all models of all SLSNe at each phase and wavelength. The resulting mean values and corresponding $\pm 1\sigma$ range in magnitudes are shown in Fig. 6. This map provides an estimate of the mean AB magnitude and scatter of SLSNe at any wavelength between 2100 and 16 000 Å and any phase between −23 and 243 d. For ease of use, we provide a version of this map as a function of days from peak, and another as a function of days after explosion in the data repository.

While the light curves used to generate this map were generated using the common filters listed in Section 3, we provide an option to estimate the mean magnitude of SLSNe at any arbitrary wavelength and phase by interpolating this map. For example, in Fig. 7, we show the mean evolution of SLSNe in $griz$ bands, as well as the individual light curves of each SLSN in grey.

Figure 5. Light curves and best-fitting MOSFIT models for all 168 gold SLSNe, shown in order of discovery date. Upper limits are shown as inverted triangles.

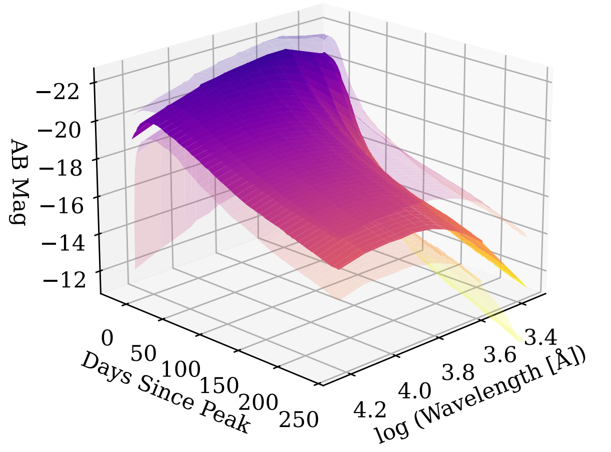

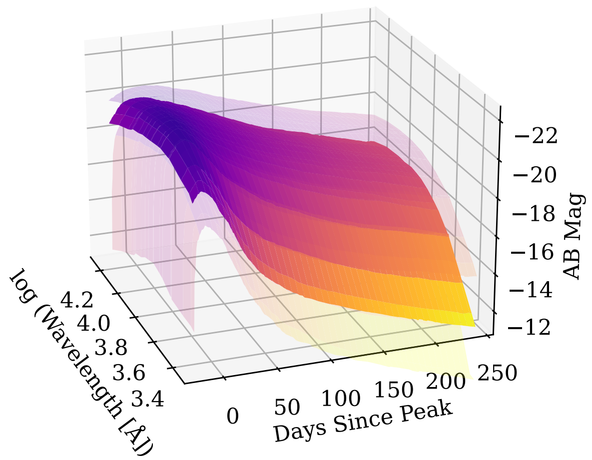

Figure 6. 3D visualization seen from two vantage points of the mean absolute AB magnitude as a function of phase and rest-frame wavelength for the full sample of SLSNe. The solid contour shows the mean of the distribution, while the shaded contours represent the $\pm 1\sigma$ range in the population. The colour represents the AB magnitude.

4.2 *K*-corrections

If one observes an SN at a redshift z through a filter with an effective wavelength $\lambda_{\rm obs}$ and measures a magnitude $m_{\rm obs}$, these observations are actually probing the spectral energy distribution (SED) of the SN at $\lambda_{\rm rest} = \lambda_{\rm obs}/(1+z)$ with a magnitude $m_{\rm rest}$. If the goal is to measure the absolute magnitude of the SN in the rest frame, this can be calculated as $M_{\rm rest} = m_{\rm obs} - \mu - K$, where μ is the distance modulus and K is the K-correction (Hogg et al. 2002). If the SNs were to have a flat SED with constant luminosity λL_λ, the K-correction would be simply $K = -2.5\log_{10}(1+z)$. Real SNe however do not have a flat SED, which requires us to know, or assume, the colour of the SED to account for the difference in magnitude between $m_{\rm rest}$ and $m_{\rm obs}$, and derive an accurate K-correction. A more accurate K-correction is $K = (m_{\rm rest} - m_{\rm obs}) - 2.5\log_{10}(1+z)$. While the most accurate K-correction value will depend on the specific SED of each SN, we can estimate the mean K-correction value for the SLSN population at large and use this to obtain a rapid approximation of their rest-frame magnitude. We use the 3D map shown in Fig. 6 to derive these mean K-correction values for SLSNe as a function of wavelength and phase.

We provide a PYTHON script for calculating K-corrections that takes in values for $\lambda_{\rm obs}$, z, and phase, as well as an optional output wavelength to which the data will be corrected $\lambda_{\rm output}$. If no value for $\lambda_{\rm output}$ is provided, this is assumed to be $\lambda_{\rm output} = \lambda_{\rm rest} = \lambda_{\rm obs}/(1+z)$. The code will calculate the mean colour difference between $m_{\rm rest}$ and $m_{\rm obs}$ to derive the K-correction. A demonstration of how to run the code is provided in Section 7. We show an example of these corrections applied to three representative SLSNe in Fig. 8. We show how our method generally provides more accurate rest-frame light curves than the simplistic $+2.5\log_{10}(1+z)$ correction, with the exception of SNe with a redshift $\gtrsim 1$. For these high-redshift SNe, we recommend using a filter with a $\lambda_{\rm obs}$ closer to the desired $\lambda_{\rm rest}$, if available. For example, for an SN at $z = 0.9$, z-band observations with $\lambda_{\rm obs} \sim 8920$ Å are actually probing $\lambda_{\rm rest} \sim 4690$ Å. This value is much closer to the rest-frame wavelength of g band at ~ 4670 Å. In this case, using z-band observations would provide a much better estimate of the rest-frame g-band magnitude than observed g band would.

4.3 Bolometric scaling

We use the MOSFIT light-curve models to derive a relation between the observed photometry and the bolometric luminosity of SLSNe. For each SN, we calculate the ratio between its monochromatic luminosity measured in an observed filter $\lambda L_\lambda[{\rm erg\ s^{-1}}]$ and its bolometric luminosity $L_{\rm Bol}[{\rm erg\ s^{-1}}]$ as a function of phase. This way we create a map of the mean ratio between L_λ and $L_{\rm Bol}$ as a function of phase and wavelength for all SLSNe. We show this map in Fig. 9, which we fit with a 2D fourth-degree polynomial shown in equation (1), where ϕ is the phase and λ is the wavelength. Using this equation, we derive a functional form of the mean value of $L_\lambda/L_{\rm Bol}$ as a function of phase and wavelength. This scaling can then be applied to any observed photometry between 2100 and 16 000 Å and any phase between −50 and 250 d to obtain an estimate of the bolometric luminosity of an SLSN

$$P(\phi, \lambda) = \sum_{i=0}^{4} \sum_{j=0}^{4-i} a_{ij}\phi^i \lambda^j. \tag{1}$$

Applying this bolometric scaling to the light curves of SLSNe also helps shifts the peak of the monochromatic light curve closer to the time of bolometric peak. In Fig. 10, we show how the mean time of light-curve peak varies as a function of rest-frame wavelength. Light curves observed in filters with rest-frame wavelengths bluer than ~ 2700 Å peak before bolometric peak, and redder filters peak after bolometric peak. This also means that filters with rest-frame wavelengths close to ~ 2700 Å provide the most accurate estimates of bolometric peak for SLSNe. After applying our bolometric scaling correction to the light curves of all SLSNe, we see this relation becomes much flatter, particularly for wavelengths $\lesssim 10000$ Å. In Section 7, we show code examples on how users can apply these corrections to any SLSN.

4.4 Evolution

In Fig. 11, we show the evolution of the bolometric luminosity, photospheric radius, and temperature for all SLSNe, as well as a blackbody velocity derived from the EXTRABOL models in Section 3.2. We see that SLSNe have initial temperatures of $T \sim 10000 - 15000$ K, and then settle into a mean temperature of $T \sim 7000$ K. The typical radius of SLSNe expands from an initial $R \sim 2 \times 10^{15}$ to $\sim 5 \times 10^{15}$ cm before receding back to a radius of $R \sim 2 \times 10^{15}$ cm, in line

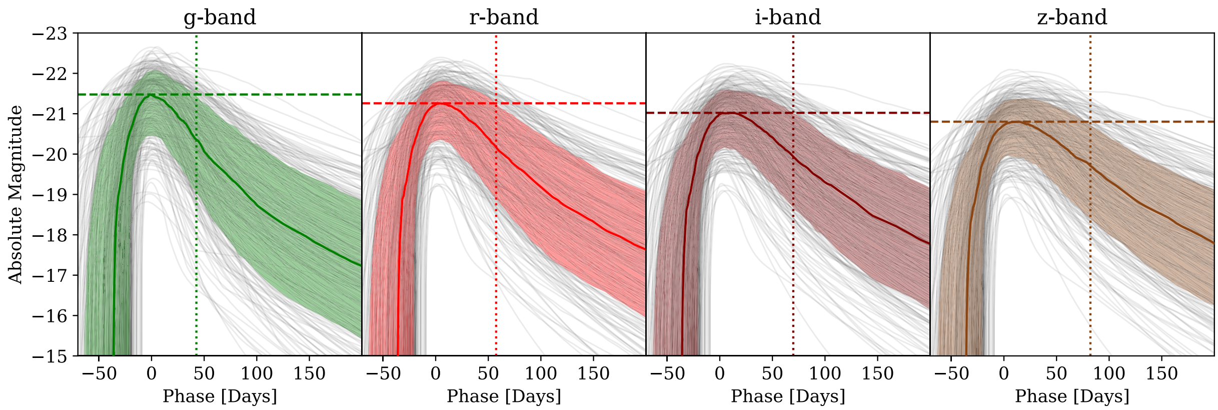

Figure 7. Rest-frame absolute magnitude light curves in the *griz* bands for the full sample of SLSNe as a function of phase from their respective peaks. The grey lines show the light curves of each individual SLSN, while the solid colour curves and shaded regions represent the mean evolution of the full sample and their 1σ ranges, respectively. The horizontal dashed and vertical dotted lines demarcate the mean peak magnitude in each band and the mean τ_e decline time-scale in each band.

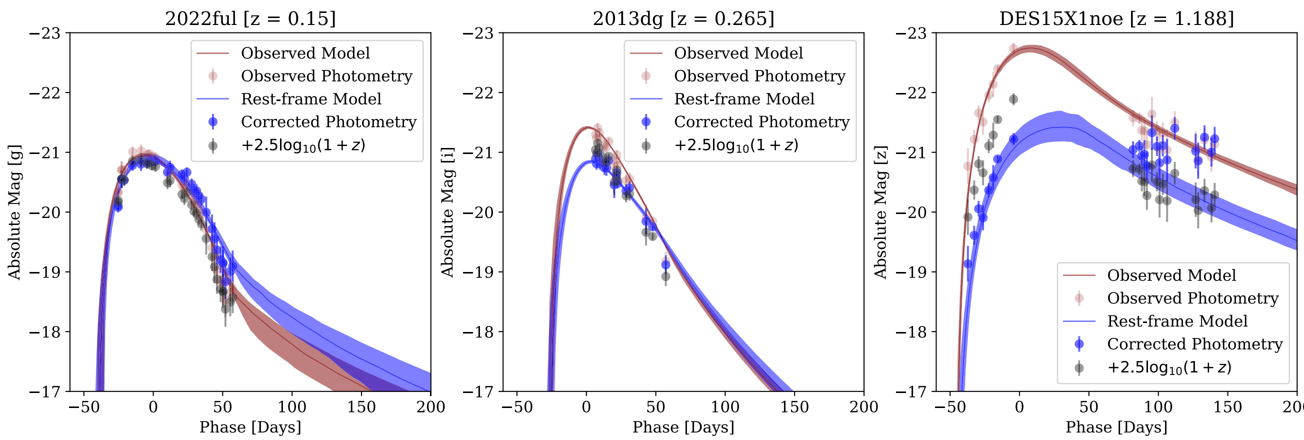

Figure 8. Example of applying our optimal *K*-correction model to a few representative SLSNe, spanning a broad range of redshifts. The brown points and shaded regions represent the observed photometry and best-fitting model, respectively. The blue points and shaded regions are the same data, but after applying our *K*-correction model. The black points represent the same photometry but modified using only a simple *K*-correction of $+2.5\log_{10}(1+z)$. Our method outperforms the simple *K*-correction for most cases.

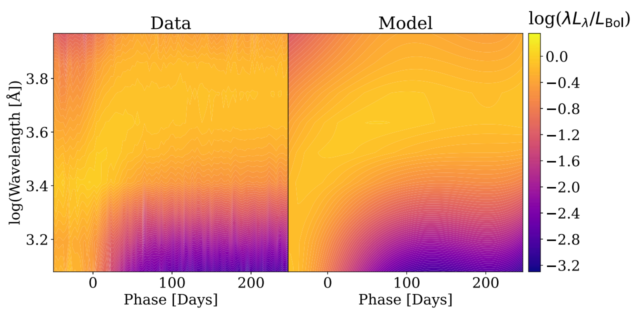

Figure 9. Bolometric correction ratio $\lambda L_\lambda/L_{\rm Bol}$ as a function of phase and rest-frame wavelength. The left panel shows the data representing the mean value of $\lambda L_\lambda/L_{\rm Bol}$ for the full sample of SLSNe, while the right panels shows a fourth-order 2D polynomial fit to these data.

with expectations from models of homologous expansion of SNe (Liu et al. 2018b). While these measurements are consistent with previous results (e.g. Lunnan et al. 2018c; Chen et al. 2023a; Hinkle et al. 2023), the larger sample size used here allows us to constrain the decrease in photospheric radius ~ 50 d after peak, not clearly evident in previous studies, which in turn allows us to measure the velocity at which the blackbody radius evolves.

We use the rest-frame light-curve models from MOSFIT to calculate the mean colour evolution for SLSNe for a series of filter pairs. In Fig. 12, we show this evolution, where we see SLSNe tend to be blue before peak with a mean colour of $g-r\sim -0.2$ before reddening with time to typical values of $g{-}r\sim 0.2-0.8$.

We find the mean duration for an SLSN to reach peak from explosion is $\tau_{\rm rise}=27^{+25}_{-13}$ d. This parameter is tightly correlated with the decline time τ_e, which has a mean value of $\tau_e=44^{+38}_{-18}$ d, as shown in Fig. 13. These parameters are similarly correlated with both τ_1 and Δm_{15}. We fit the relation between various rise and decline time-scales and find the following correlations:

$$\log(\Delta m_{15}) = (-0.51\pm 0.01)\times \log(\tau_1) + (1.32\pm 0.01)$$
$$\log(\tau_e) = (0.82\pm 0.02)\times \log(\tau_1) + (0.35\pm 0.04)$$
$$\log(\Delta m_{15}) = (-0.59\pm 0.02)\times \log(\tau_{\rm rise}) + (1.00\pm 0.02)$$
$$\log(\tau_e) = (1.00\pm 0.03)\times \log(\tau_{\rm rise}) - (0.20\pm 0.05).$$

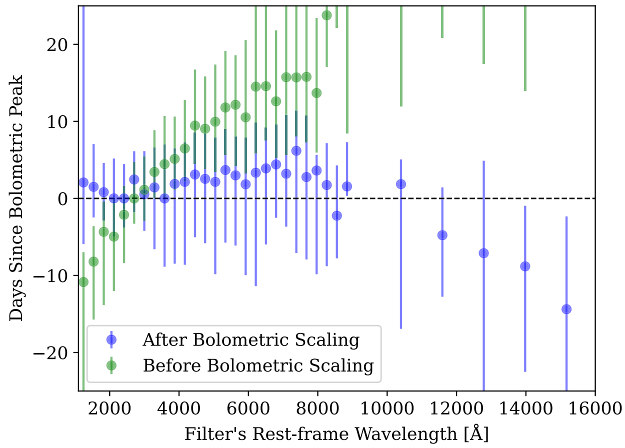

Figure 10. The mean time of light-curve peak relative to the peak of the bolometric light curve as a function of the rest-frame wavelength for the full sample, shown before (green) and after (blue) applying a bolometric scaling. Before bolometric scaling, it is evident the peak time evolves as a function of wavelength.

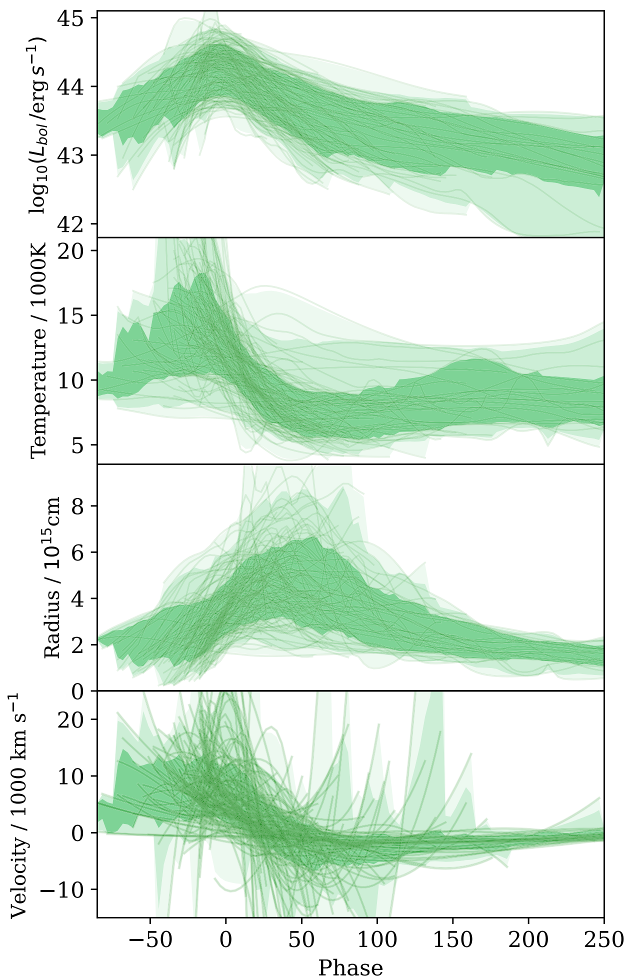

Figure 11. Bolometric luminosity, and photospheric temperature, radius, and velocity as a function of phase for the full sample. These parameters are derived from the EXTRABOL model fits to the light curves. The shaded regions represent the $\pm$ 1σ, 2σ, and 3σ ranges.

De Cia et al. (2018) studied a sample of 26 SLSNe and was able to measure the decline rates of 13 of these. The authors found all measured decline rates to be consistent with the rate of decay of ^{56}Co to ^{56}Fe of 0.0098 mag d^{-1}, assuming full trapping of the decay process. We perform a similar experiment here, and manage to measure the decline rates of 105 SLSNe at 100 d post-explosion, but find only $\sim$ 17 per cent of these to have a decline rate consistent with the radioactive decay of ^{56}Co, while all other SLSNe decline faster than this. Therefore, we conclude these slow decline rates are most likely the low end of a distribution of SLSNe decline rates and do not necessarily imply these are radioactively dominated tails.

4.5 Extreme SLSNe

In this section, we outline the properties of the SLSNe with the most extreme observational parameters. The SLSNe with the brightest rest-frame r-band magnitudes are DES16C2nm with $m_r = -22.67 \pm 0.53$ and SCP06F6 with $m_r = -22.55 \pm 0.21$, each $\sim 2\sigma$ brighter than the mean of the distribution. However, these two SLSNe are found at relatively large redshifts of $z = 1.998$ and 1.189 and their peak r-band estimates have a large uncertainty since we have to extrapolate their observed magnitudes into rest-frame r band. SN 2020dlb has a similarly bright peak magnitude of $m_r = -22.44 \pm 0.05$, or $\sim 1.7\sigma$ brighter than the mean SLSN, but with a much better constrained measurement and at a redshift of only $z = 0.398$, making it the brightest relatively nearby SLSN to date.

The SLSN with the highest peak bolometric luminosity is SN 2017ens, which reached a luminosity of $\log(L) = 45.3 \pm 0.1$ erg s^{-1}, or $\sim 2.7\sigma$ brighter than the mean of the SLSN distribution. This excess luminosity seen in SN 2017ens might be due to additional energy input from interaction with CSM (Chen et al. 2018). The SLSNe with the highest total integrated radiated energy during the first 200 d after explosion are PTF12dam and SN 2020afag, both with a total radiated energy of $\log(E_{\rm rad}) \approx 51.8$ erg, or $\sim 1.9\sigma$ above the mean of the distribution. For a discussion on the dimmest SLSNe, see Gomez et al. (2022a), where we describe the continuum formed between SLSNe and Type Ic/Ic-BL SNe. The furthest SLSN found to date is DES16C2nm at a redshift of $z = 1.998$, while the closest one is SN 2018bsz at a redshift of $z = 0.0267$.

The SLSN with the slowest rise time in our sample is PS1-14bj, which took $\tau_{\rm rise} = 129 \pm 4.6$ d to reach its peak, or $\sim 4.0\sigma$ slower than the mean of the SLSN distribution. The SLSN with the slowest ejecta velocity is SN 2022le, with a best fit of $V_{\rm ej} = 1030 \pm 30$ km s^{-1} and a corresponding blackbody velocity of $V_{\rm BB} \approx 1190$ km s^{-1}, each around $\sim 1.9\sigma$ slower than the mean of the population. SN 2022le took a notably long $\tau_1 = 210 \pm 9$ d to fade from peak by 1 mag, a significant $\sim 4.5\sigma$ longer than the mean SLSN population.

5 RESULTS

In this section, we discuss the results derived from the MOSFIT model fits. Additionally, we include comparisons to the observational parameters derived in Section 4 and previous studies.

5.1 Parameter distributions

In Table 3, we list the mean values and 1σ scatter for all physical and observational parameters presented in this work. The distributions of the best-fitting values as well as their correlations for the full SLSN population are shown in Fig. 14. We use the full sample of SLSNe, including an exploration of all their physical and observational parameters, to attempt to separate SLSNe into distinct groups with

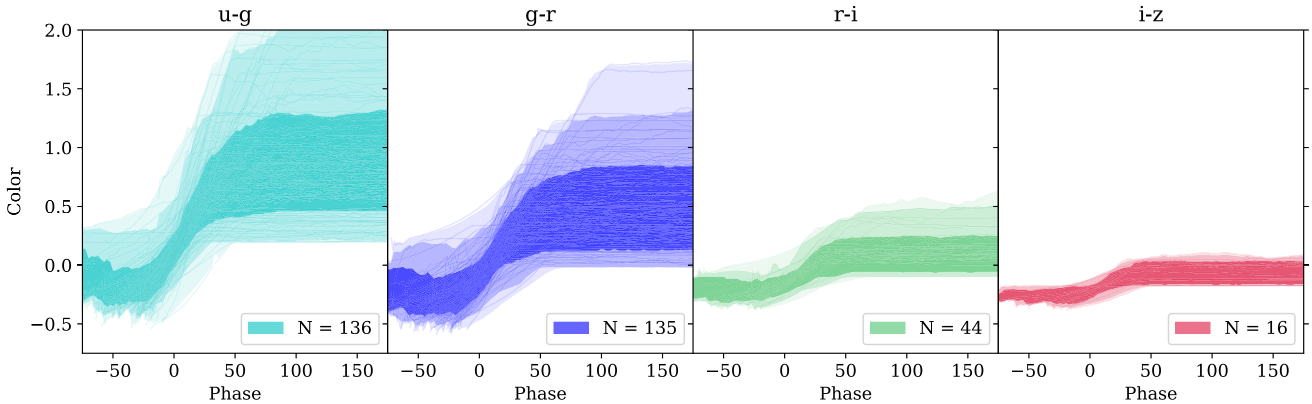

Figure 12. Rest-frame colours as a function of phase, derived from an interpolation of the SLSNe light curves using MOSFIT. We only include N objects for which there are observations available in the interpolated filters. The shaded regions represent the $\pm$ 1σ, 2σ, and 3σ ranges. The redder filter pairs have a smaller span in colours in part because the shape of the SED flattens out at redder wavelengths, but these are also less well measured given that there are fewer observations available in these filters.

the aim of determining whether there are distinct classes of SLSNe. We use the SCIKIT-LEARN (Pedregosa et al. 2011) implementation of the K-means clustering algorithm, a popular method for partitioning a data set into distinct, non-overlapping clusters which assigns each data point to its nearest cluster centre, with the goal of minimizing the variance within each cluster. The most significant clustering separation we find has two clusters with a silhouette coefficient of 0.13, which roughly separates the most luminous SLSNe from the least luminous ones. A silhouette coefficient this low suggests that the clusters are weakly distinguished from each other (Rousseeuw 1987). This means we are unable to find any significant separation in the existing SLSN population, and SLSNe appear to be drawn from a mostly continuous distribution, at least based on photometry alone (Inserra et al. 2018a; Quimby et al. 2018). Future studies that include spectroscopic parameters of SLSNe might find a different conclusion.

We caution that the value of $M_{\rm NS}$ has very little effect on the light curve, and its posterior distribution is therefore largely unconstrained and dominated almost entirely by the choice of prior. Similarly, any value of $n_{\rm H,host}$ below $\sim 10^{-18}$ cm^{-2} reflects effectively no extinction and is therefore unconstrained.

5.2 Magnetar parameters

In Fig. 15, we show the key magnetar parameters $P_{\rm spin}$ and $B_{\perp}$ for the full population of SLSNe. We include the trend lines from Nicholl et al. (2017c) that show different ratios of magnetar time-scale $t_{\rm mag}$ to diffusion time-scale $t_{\rm diff}$ for a fixed ejecta mass of $M_{\rm ej} = 9.3$ M$_{\odot}$, equal to the mean of the SLSN population. Most of the SLSNe lie above the $t_{\rm mag}/t_{\rm diff} = 0.1$ line, suggesting that for fast spin periods, the magnetar loses energy quickly, but that enough rotational power is left to produce a long diffusion time-scale. While almost all of the brightest SLSNe with $M_r \sim -22$ mag have a strong preference for short spin periods $\lesssim 4$ ms, not all SLSNe with short spin periods are brighter than this. This implies that while high rotational energy is key to producing luminous SLSNe, other parameters such as having a large ejecta mass can contribute as well. Hinkle et al. (2023) studied a sample of 27 SLSNe and found a tentative correlation between ejecta mass and magnetic field strength. We determine that this correlation was most likely an artefact of the small sample size, given that we see no evidence for a correlation between these two parameters.

In Fig. 16, we show the total KE of the SLSN population as a function of the magnetar spin period $P_{\rm spin}$. It is not surprising that

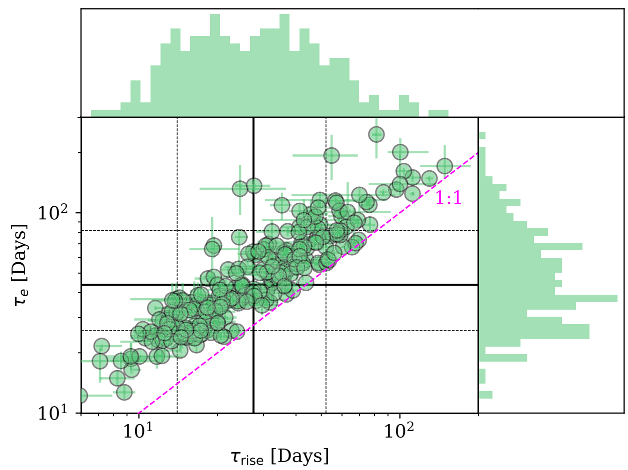

Figure 13. The e-fold decline time $\tau_{\rm e}$ as a function of rise time $\tau_{\rm rise}$ for the full sample of SLSNe. The solid and dashed lines show the mean and 1σ values of these parameters, respectively. The pink line shows the one-to-one correspondence.

this correlation tracks the evolution of the total energy of a magnetar with an assumed mass of 1.7 M$_{\odot}$, since most of the KE of the SLSNe is dominated by the magnetar contribution.

We calculate $f_{\rm mag}$, or the fraction of the total radiated energy that comes from the magnetar component during the first 200 d. For the SLSNe with a measurable radioactive decay contribution, we find that its fractional contribution tends to flatten after $\sim$ 100 d. We aim to determine which SLSNe have a non-negligible contribution from radioactive decay. On the left panel of Fig. 17, we show the $f_{\rm mag}$ value distribution for all SLSNe as a function of $P_{\rm spin}$. We find that $\sim$ 6 per cent of SLSNe have a contribution from radioactive decay in which the lower bound of the best-fitting $f_{\rm mag}$ value is still above 10 per cent, and only $\sim$ 2.5 per cent above 50 per cent. The only six SLSNe with a mean magnetar contribution $f_{\rm mag} < 0.5$ are SN 2020abjc, SN 2020rmv, SN 2020vpg, SN 2021lwz, iPTF13bdl, and iPTF13bjz, all relatively dim and slowly declining SLSNe. On the right panel of Fig. 17, we show how SLSNe with high $\tau_{\rm rise}$ values are the most likely to be powered by at least some contribution from

Table 3. Mean and standard deviation of various observational and physical parameters.

Parameter	Value	Parameter	Value	Parameter	Value	Parameter	Value
z	$0.26^{+0.3}_{-0.13}$	$\log(L_{\max}/\mathrm{erg\ s^{-1}})$	$44.3^{+0.3}_{-0.5}$	$M_{\mathrm{Ni}}/\mathrm{M_\odot}$	$0.3^{+1.9}_{-0.2}$	$\log(n_{H,\mathrm{host}}/\mathrm{cm^{-2}})$	$18.2^{+0.5}_{-0.4}$
$t_{\mathrm{rise}}/\mathrm{d}$	27^{+25}_{-13}	$P_{\mathrm{spin}}/\mathrm{ms}$	$2.4^{+3.0}_{-1.2}$	$\log(\mathrm{KE/erg\ s^{-1}})$	51.4 ± 0.4	$\lambda/\mathrm{Å}$	3400^{+1000}_{-700}
τ_1/d	53^{+35}_{-20}	$\log(B_\perp/G)$	14.2 ± 0.4	$\log(L_0/\mathrm{erg\ s^{-1}})$	$45.8^{+1.9}_{-1.3}$	α	$1.7^{+1.5}_{-1.3}$
$\tau_{\mathrm{e}}/\mathrm{d}$	44^{+38}_{-18}	$T_{\min}/\mathrm{K}$	6500^{+1700}_{-1400}	$\log(t_{\mathrm{SD}}/\mathrm{s})$	5.7 ± 1.0	$(M_{\mathrm{NS}}/\mathrm{M_\odot})^a$	1.72 ± 0.04
$\Delta m_{15}/\mathrm{mag}$	$0.2^{+0.2}_{-0.1}$	$V_{\mathrm{ej}}/1000\ \mathrm{km\ s^{-1}}$	$6.8^{+3.4}_{-2.0}$	f_{mag}	$1.0^{+0.0}_{-0.1}$	$(\theta_{\mathrm{BP}}/\mathrm{rad})^a$	$1.0^{+0.1}_{-0.2}$
$M_{\max}/\mathrm{mag}$	$-21.3^{+0.9}_{-0.6}$	$M_{\mathrm{ej}}/\mathrm{M_\odot}$	$9.3^{+12.9}_{-4.8}$	ϵ	$0.5^{+0.6}_{-0.3}$	$(\kappa/\mathrm{cm^2 g^{-1}})^b$	$0.08^{+0.11}_{-0.05}$
m_r/mag	$19.2^{+1.4}_{-1.2}$	f_{Ni}	$0.02^{+0.14}_{-0.02}$	A_V/mag	$0.0009^{+0.0022}_{-0.0005}$	$(\kappa_\gamma/\mathrm{cm^2 g^{-1}})^b$	$0.06^{+0.07}_{-0.05}$
$E_{\mathrm{rad}}/\mathrm{erg}$	$51.1^{+0.3}_{-0.5}$						

Notes. List of all parameters for SLSNe, their mean value, and 1σ ranges. We include observational and physical parameters. For definitions of the physical parameters, see Table 2. z is the redshift, τ_{rise} is the time from explosion to peak, τ_1 is the time it takes the SN to decline by 1 mag, τ_{e} is the time it takes the SN to decline by a factor of e, Δm_{15} is the magnitudes by which an SN fades 15 d after maximum in B band, $M_{\max}$ is the peak rest-frame r-band magnitude, m_r is the peak observed r-band magnitude, E_{rad} is the total radiated energy of the SN during the first 200 d, $L_{\max}$ is the luminosity at peak, M_{Ni} is the nickel mass, KE is the kinetic energy, L_0 and t_{SD} are the initial magnetar spin-down luminosity and spin-down time from Omand & Sarin (2024), f_{mag} is the fraction of the total luminosity due to the magnetar contribution, ϵ is the radiative efficiency, and A_V is the intrinsic host extinction in V band.
[a] These parameters are mostly unconstrained by the data and the posterior is highly dependent on the choice of prior.
[b] These parameters are only constrained for a fraction events.

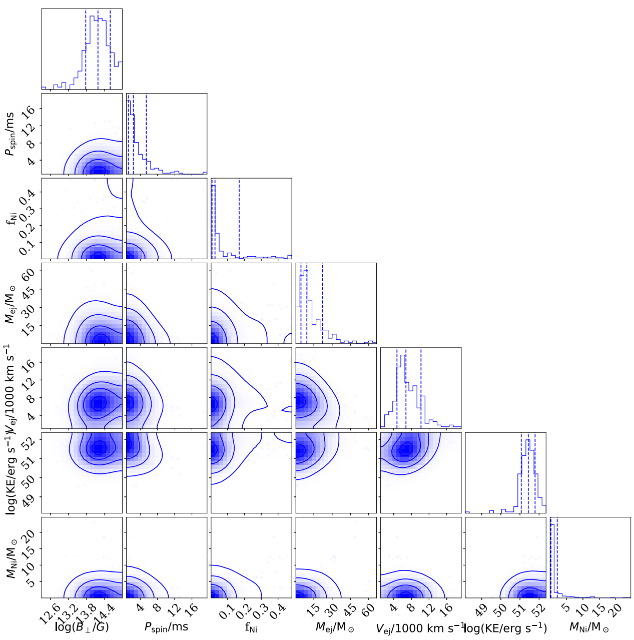

Figure 14. Corner plot showing the correlation between the most critical physical parameters for the full sample, defined in Table 2. The histograms show the marginalized distribution of each parameter, as well as the mean and $\pm 1\sigma$ range.

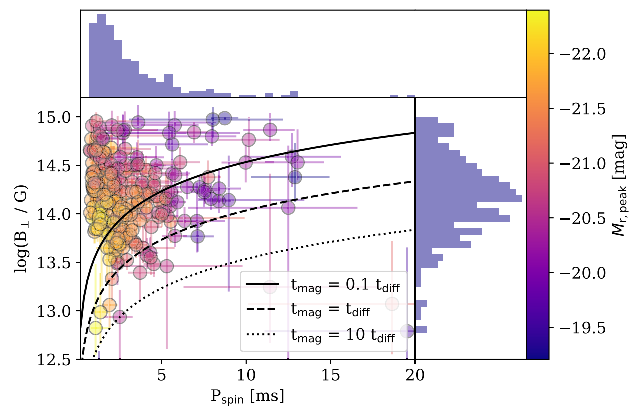

Figure 15. Magnetic field versus spin period for the full sample, colour coded by peak absolute magnitude in rest-frame r band. The black lines show trends for different ratios of the magnetar to diffusion time-scales, assuming the mean ejecta mass and KE for the sample, as listed in Table 3. For very fast spin periods, the magnetar time-scale can be much shorter than the diffusion time-scale.

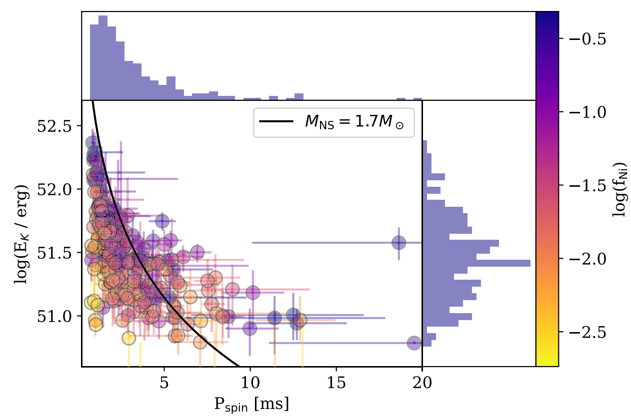

Figure 16. KE versus spin period for the full sample of SLSNe, colour coded by ^{56}Ni fraction. The black line represents the magnetar energy for a 1.7 $\mathrm{M_\odot}$ neutron star, which tracks the observed trend well.

radioactive decay. This is particularly true for SLSNe with peak r-band magnitudes dimmer than ~ -21 mag.

We test the effects of removing the radioactive decay component from the light-curve models of the seven SLSNe with the lowest f_{mag} values, SN 2020abjc, SN 2020rmv, SN 2020vpg, SN 2021lwz, iPTF13bdl, and iPTF13bjz. In Fig. 18, we show the best-fitting parameters for these four SNe modelled with a pure magnetar model to explore how this model compares to the standard magnetar plus radioactive decay model. The magnetar-only models of all SLSNe, except for SN 2021lwz, have values of M_{ej}, V_{ej}, $B_\perp$, and P_{spin} that remain consistent within 1σ when compared to the magnetar plus radioactive decay models, although with systematically lower values of P_{spin} and higher values of $B_\perp$.

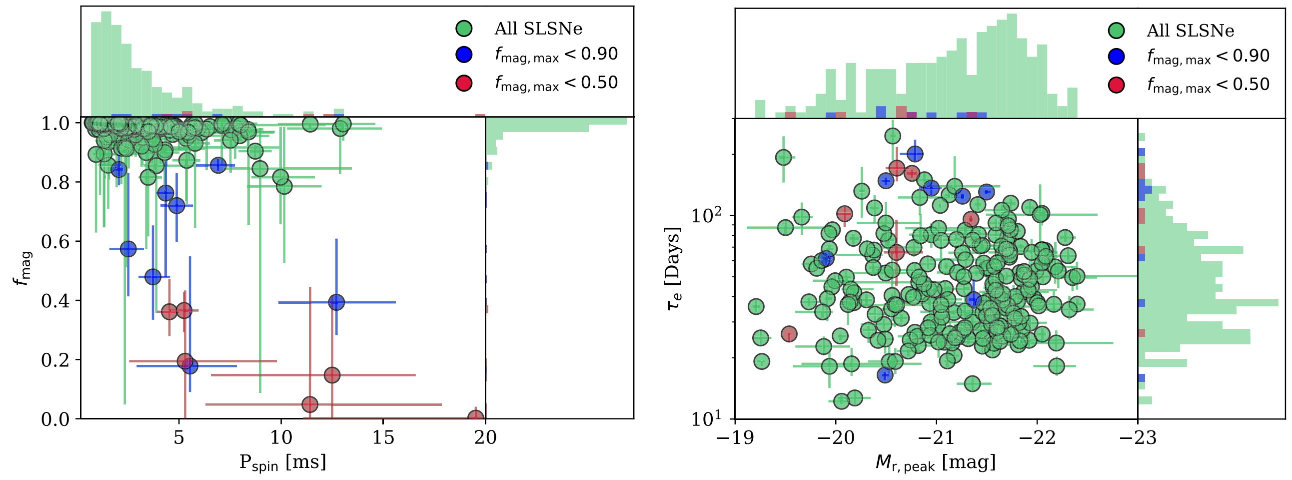

Figure 17. Left: the fraction of total radiated energy produced by a magnetar (f_{mag}), as opposed to radioactive decay, as a function of P_{spin}. The blue and red points mark SLSNe in which more than 10 per cent and 50 per cent, respectively, of the radiated energy is from radioactive decay. Right: the e-fold decline time τ_e as a function of peak r-band magnitude M_r for the full sample of SLSNe. The SLSNe with the highest fraction of radioactive decay input are slowly declining and relatively dim.

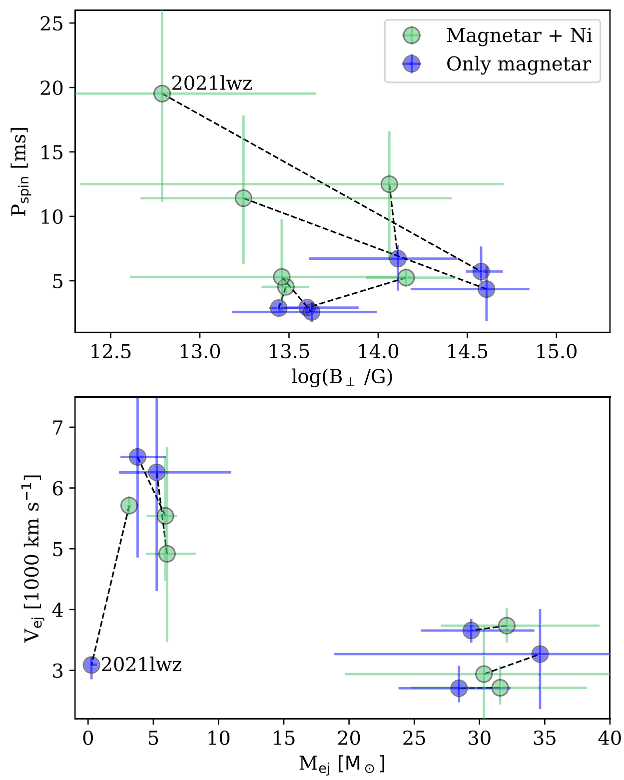

Figure 18. Key physical parameters for the six SLSNe with the smallest f_{mag} values (SN 2020abjc, SN 2020rmv, SN 2020vpg, SN 2021lwz, iPTF13bdl, and iPTF13bjz). In green, we show the parameters from our fiducial magnetar plus radioactive decay model, and in blue, the corresponding best-fitting values after removing the radioactive decay component from the model. The parameters for the pure magnetar model deviate by more than 1σ from the magnetar plus radioactive decay model only for SN 2021lwz. This implies that a large radioactive decay contribution is not required for most SLSNe.

SN 2021lwz is a relatively dim rapidly evolving SLSN and the only one in our sample for which we do see a significant change in the best-fitting parameters after removing the radioactive decay component. We find significantly lower values of M_{ej}, V_{ej}, P_{spin}, and a significantly higher value of $B_\perp$. While both models provide good fits to the light curves of SN 2021lwz, the standard magnetar plus radioactive decay model has a Bayesian Information Criterion (BIC; Schwarz 1978) value of 68, while the pure magnetar model has a BIC value of 63. This implies that the lower number of parameters in the pure magnetar model is preferred over the marginal gains in likelihood from the standard magnetar plus radioactive decay model. Effectively this means that all SLSNe in our sample can be fit with a pure magnetar central engine model.

In Fig. 19, we show how the best-fitting nickel mass varies as a function of ejecta mass, and mark in blue and red the SLSNe with the highest contributions from radioactive decay. A large value for the nickel fraction or nickel mass does not necessarily imply the light curve will be dominated by radioactive decay. Some SLSNe with high f_{Ni} values are still dominated by powerful magnetars with fast spin periods, whose contribution is able to overpower any contribution from radioactive decay. For these SLSNe, the posterior of the nickel mass and fraction are largely unconstrained, given that it is easy to hide large amounts of radioactive material under the large luminosity of the magnetar component.

5.3 Progenitor pre-explosion mass distribution

We measure the progenitor mass distribution for all SLSNe by summing the posterior of their ejecta mass and their corresponding posterior for the best-fitting neutron star mass. The mass of the neutron star has little effect on the output light curves. For most SLSNe, the neutron star mass posterior is largely unconstrained and dominated by the prior of 1.7 ± 0.2 M$_\odot$. We show the resulting progenitor mass distribution in Fig. 20, which has a peak of ≈ 6.5 M$_\odot$, extending as low as ~ 2 M$_\odot$ and up to ~ 40 M$_\odot$. While there is a non-zero number of samples outside this range, these are not statistically significant. We fit the tail of the pre-explosion mass distribution, from 7 to 40 M$_\odot$ with a single power law and find a best-fitting slope of $\alpha = -1.48 \pm 0.05$. Alternatively, using

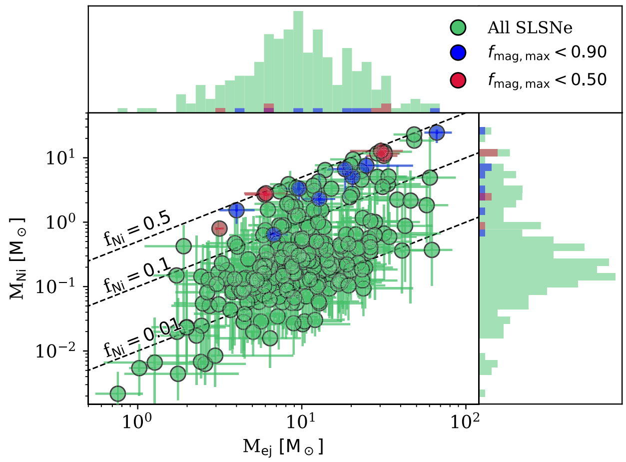

Figure 19. Nickel mass as a function of ejecta mass for the full sample. The dashed lines mark nickel fractions of 0.01, 0.1, and 0.5. The blue and red points show the SLSNe with a contribution from radioactive decay > 0.1 and > 0.5, respectively. A large nickel fraction or nickel mass does not necessarily imply the SN will be dominated by the contribution from radioactive decay. In some cases, large amounts of nickel can be hidden without having an impact on the magnetar dominated light curves.

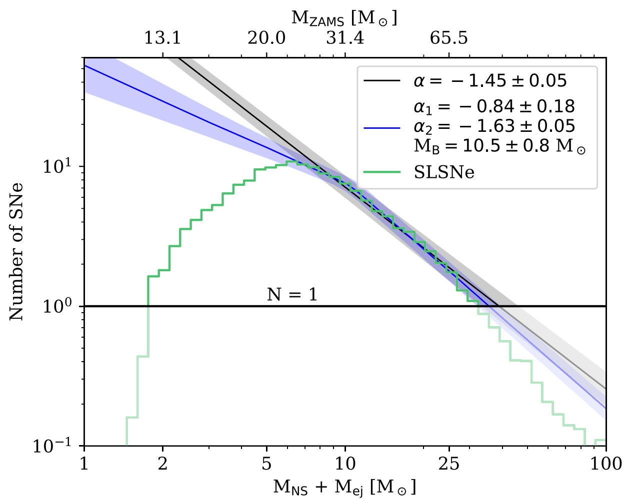

Figure 20. Progenitor pre-explosion mass distribution for the full sample of SLSNe. The green line shows a histogram of the joint posterior. The black line is the best-fitting single power-law model, and the blue line is the best-fitting broken power law to the tail of the distribution, with a break at ≈ 17 M$_\odot$. Samples below the horizontal line at $N = 1$ are not statistically significant. The top axis is derived from the correlation between the CO core mass of low-metallicity stars and their ZAMS from Sukhbold, Woosley & Heger (2018).

a broken power law, we find slopes of $\alpha_1 = -0.78 \pm 0.21$ and $\alpha_2 = -1.68 \pm 0.06$ with a break at $M_B = 10.7 \pm 0.8$ M$_\odot$. With a reduced χ^2 value of $\chi^2/\text{d.o.f.} = 3.04$, the broken power law is a better fit than the single power law with $\chi^2/\text{d.o.f.} = 34.8$. The existence of a broken power law implies that there might be multiple progenitor channels at play when producing SLSNe, leading to the distinct slopes in the high-end mass distribution. The slopes found here are steeper than the $\alpha_1 = -0.41 \pm 0.06$ and $\alpha_2 == -1.26 \pm 0.06$ found by Blanchard et al. (2020b). We find that the decline at the low end of the distribution is shallower than the one seen in the sample of 62 SLSNe from Blanchard et al. (2020b). We are able to recover the slopes found in Blanchard et al. (2020b) if we restrict our sample to the same 62 SLSNe used in that work, albeit with a break at $M_B = 10.6 \pm 0.8$ M$_\odot$, higher than the $M_B = 8.6$ M$_\odot$ found in Blanchard et al. (2020b).

However, we note that the distribution of posteriors can vary with sample size, suggesting that there may be a sample size-dependent bias, due to the noisy mass measurements from our sample. Poorly constrained posteriors can 'smooth' the slope of this power law as the posteriors spread their support across wide mass ranges. To test for this bias, we measure the value of the best-fitting slope as a function of number of SNe included in the sample. We run this test on 500 random subsamples of 10–238 SLSNe and find no correlation between sample size and best-fitting slope. We determine that $N \sim 110$ SLSNe are necessary and sufficient to obtain a confident measurement of the slope and its corresponding uncertainty given that their values remain largely constant for samples larger than this. An exploration of possible observational biases was carried out in Blanchard et al. (2020b), who found a slight bias against the lowest progenitors with $M \lesssim 6$ M$_\odot$, which effectively slightly flattens the distribution, but not significantly enough to change the results.

We compare our results with the CCSNe explosion models from Sukhbold et al. (2018), who evolve a set of stars with ZAMS from 12 to 60 M$_\odot$ at low metallicity, which should be the most representative of SLSNe progenitors. We equate our pre-explosion mass distribution measurements with the CO-mass measurements of the low-metallicity models from Sukhbold et al. (2018) to derive an estimate of the ZAMS masses of the progenitors of SLSNe. We find a corresponding peak of the distribution of $M_{\rm ZAMS} \sim 23$ M$_\odot$, with a low end of $M_{\rm ZAMS} \sim 13$ M$_\odot$ and extending beyond the most massive 60 M$_\odot$ progenitors presented in Sukhbold et al. (2018). Models for oxygen-zone emission from Jerkstrand et al. (2017) found that at least 10 M$_\odot$ of oxygen is required to reproduce the spectra of a small sample of SLSNe, which translates to a ZAMS mass of ~ 40 M$_\odot$. The fact that we see a large population of SLSNe with progenitor masses lower than this might indicate that these are underestimated, or that not all SLSNe have such a high oxygen mass requirement.

In Gomez et al. (2022a), we found the pre-explosion mass distribution of LSNe peaks at ~ 5 M$_\odot$, and below ~ 4 M$_\odot$ for SNe Ic/Ic-BL. The fact that we see a turnover below ~ 6 M$_\odot$ for SLSNe suggests there might be a fundamental limit or mechanism that governs the minimum mass of progenitors capable of producing SLSNe that becomes relevant for stars below $M_{\rm ZAMS} \sim 23$ M$_\odot$, or that stars with CO-cores below ~ 6 M$_\odot$ are less efficient at producing SLSNe. Blanchard et al. (2020b) studied the possibility that this could be due to an observational bias, and concluded that observational biases had little effect on the measured pre-explosion mass distribution. It is possible this is an effect of the low metallicity required to produce SLSNe. For example, Aguilera-Dena et al. (2023) claim that Type Ic SN progenitors likely experience additional mass loss during their evolution, either from winds or a different mechanism, leading to their lower pre-explosion mass distribution.

5.4 Lack of redshift dependence

We find no strong correlation with redshift for any physical or observational parameter. The parameter with the strongest correlation with redshift is the spin period, which we find has a mean value of $P_{\rm spin} = 2.6^{+3.3}_{-1.3}$ ms for SLSNe closer than $z = 0.5$ and $P_{\rm spin} = 2.1^{+0.9}_{-1.5}$ ms for SLSNe further than $z = 0.5$. This difference is not statistically significant enough to claim a redshift dependence. Moreover, the difference goes away completely when we consider only SLSNe

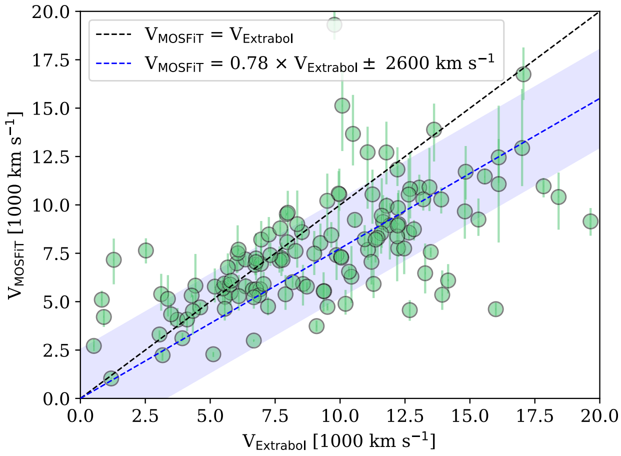

Figure 21. Velocity derived from the EXTRABOL models compared to the ejecta velocity derived from the MOSFIT models a sample of 136 SLSNe. The black line shows the 1-to-1 correspondence between the two values, while the blue line is a best-fitting line of the correlation with the y-intercept fixed at 0. We find the two measurements of velocity to be generally consistent.

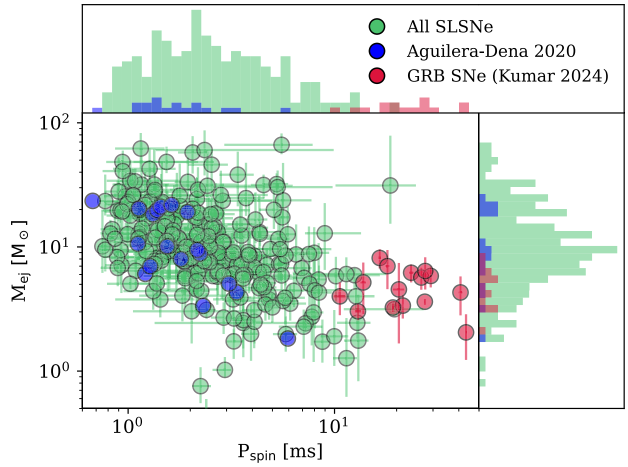

Figure 22. Ejecta mass versus spin period for the full sample shown in green. We find the trend seen previously in Blanchard et al. (2020b), with a general absence of events with low ejecta mass and rapid spin. Also shown are models of SLSNe explosions from Aguilera-Dena et al. (2020, blue) and fits to GRB-SNe using a magnetar model from Kumar et al. (2024, red).

brighter than $M_r = -21.5$ mag, suggesting this is simply an observational bias that makes SLSNe with slow P_{spin} values harder to observe at further distances. This is consistent with previous findings from Hsu et al. (2021) and De Cia et al. (2018).

5.5 Velocity

In the bottom panel of Fig. 11, we show how typical SLSNe begin with a blackbody velocity of $V \sim 10,000$ km s^{-1} and remain constant before reaching peak, after which the photosphere begins to recede deeper into the ejecta. We compare the ejecta velocity from MOSFIT to the blackbody velocity derived from the photospheric radius evolution measured with EXTRABOL, measured before peak. We are able to obtain this measurement with EXTRABOL for 136 SLSNe, other SLSNe do not have enough photometry to fit with EXTRABOL. In Fig. 21, we show how these two measurements compare. We find good agreement between the two methods, but find that the ejecta velocity from MOSFIT is around 20 per cent lower then the velocity derived from EXTRABOL, with an intrinsic scatter of ~ 2600 km s^{-1}. We find that the time of maximum photospheric radius measured from EXTRABOL is slightly sooner than the time when homologous expansion stops in MOSFIT. This difference likely leads to the lower velocity estimates from MOSFIT when compared to EXTRABOL.

5.6 Radiative efficiency

We calculate the radiative efficiency ϵ by dividing the total radiated energy over the first 200 d of an SN by the total KE. SLSNe are known to have high radiative efficiencies, but if we use the ejecta velocity from MOSFIT to calculate ϵ we find ~ 15 SLSNe with an $\epsilon > 1$. If we instead assume the higher velocity derived from the EXTRABOL models, the number of SLSNe with $\epsilon > 1$ goes down to 0, after accounting for the uncertainties in the value of ϵ. Both the radiated and KE are dominated by the magnetar spin-down. Our models suggest that most of the energy goes into accelerating the ejecta, but for the SLSNe with rapid spin periods, a higher fraction of the magnetar energy goes into radiation, particularly if they have low ejecta velocity, making these SLSNe very efficient emitters.

5.7 Comparison to other works

The models from Aguilera-Dena et al. (2020) evolve a set of low-metallicity, rapidly rotating stars with pre-explosion masses ranging from $M_{Init} = 4$ to $45\,M_\odot$. These models are thought to represent the progenitors of magnetar-powered transients such as SLSNe. In Fig. 22, we show how the spin period and ejecta mass measurements from Aguilera-Dena et al. (2020) compare to the best-fitting MOSFIT parameter for our sample of SLSNe. We find that the general correlation between P_{Spin} and M_{ej} found in the Aguilera-Dena et al. (2020) models, originally presented in Blanchard et al. (2020b), is still true, with some additional scatter likely due to the inclusion of a radioactive decay component in our models.

In Fig. 22, we also show a comparison to the P_{Spin} and M_{ej} values measured for a set of Gamma-ray burst (GRB) SNe from Kumar et al. (2024), who fit the light curves of these SNe with a magnetar central engine model. If GRB SNe are powered by SNe, we see that the general trend continues, as SNe with lower ejecta masses seem to have higher spin periods, or less powerful magnetars. The mean of the population of GRB SNe has a spin period $P_{Spin} = 21.42$ ms, which is slower than the slowest spin period of $P_{Spin} = 19.83$ ms found in the SLSN population. GRB SNe show a mean ejecta mass value of $M_{ej} = 4.8\,M_\odot$, which corresponds to the ~ 13th percentile of the SLSNe population.

For comparisons of SLSNe to the general population of SESNe, we direct the reader to Gomez et al. (2022a). In that study, we presented a connection between the 'normal' Type Ic/Ic-BL SNe and SLSNe. We concluded that LSNe, which by definition span a range of peak magnitudes from $M_r = -19$ to -20, straddle the line between SNe Ic/Ic-BL and SLSNe in terms of not only their luminosities, but also their power sources, duration, and physical parameters.

6 CONCLUSIONS

We have presented the largest sample of Type I SLSNe to date, encompassing all publicly known SLSNe and their photometry up until 2022 December 31, totalling 262 events. Of those, we determined 238 have enough photometry and spectroscopy to be robustly classified as 'gold' or 'silver' SLSNe. We use this sample of SLSNe to conduct our analysis, from which we derive our conclusions.

(i) The SLSN population has a mean rise time of $\tau_{\rm rise} = 27^{+25}_{-13}$ d, and a mean *e*-folding decline time of $\tau_e = 44^{+38}_{-18}$ d.

(ii) The mean peak rest-frame *r*-band absolute magnitude is $M_r = -21.3^{+0.9}_{-0.6}$, and the mean peak bolometric luminosity is $\log L_{\rm max} = 44.3^{+0.3}_{-0.5}$ erg s^{-1}.

(iii) SLSNe have mean ejecta masses of $M_{\rm ej} = 9.3^{+12.9}_{-4.8}$ M$_\odot$ and mean ejecta velocities derived from MOSFIT models of $V_{\rm ej} = 6800^{+3400}_{-2000}$ km s^{-1}.

(iv) We use the blackbody radius evolution from EXTRABOL to estimate the velocity of the photosphere and find these values to be ~ 20 per cent lower, but still consistent, with the ejecta velocities derived from MOSFIT.

(v) The inferred mean blackbody radius reaches a peak of $\approx 5 \times 10^{15}$ cm at ≈ 50 d post-peak, and then declines to $\approx 2 \times 10^{15}$ cm at $\gtrsim 200$ d after peak.

(vi) The mean magnetar central engine parameters are $P_{\rm spin} = 2.4^{+3.0}_{-1.2}$ ms and $\log(B_\perp/G) = 14.2 \pm 0.4$.

(vii) A magnetar central engine model is able to fit the light curves of effectively all SLSNe without additional energy sources.

(viii) Radioactive heating from ^{56}Ni decay does not have a noticeable contribution in most SLSNe, with the exception of a few of some slowly declining, relatively dim SLSNe.

(ix) We do not find a correlation between ejecta mass and magnetic field strength, as suggested by Hinkle et al. (2023).

(x) We find no significant redshift-dependence for any physical or observational parameter.

(xi) We find no strong evidence for subtypes of SLSNe when considering the full range of observed and physical properties. For example, SLSNe do not split between slow and rapid subpopulations, but instead form a smooth continuum.

(xii) We find the late-time decline rates for most SLSNe to be faster than the expectation from radioactive ^{56}Co decay. SLSNe with decline rates consistent with that of ^{56}Co decay can be explained by simply representing the slow end of the distribution of decline rates.

(xiii) The progenitor pre-explosion mass distribution peaks at ≈ 6.5 M$_\odot$, which roughly corresponds to a ZAMS mass of $M_{\rm ZAMS} \sim 23$ M$_\odot$.

(xiv) The progenitor pre-explosion mass distribution extends as low as ≈ 2 M$_\odot$ and up to ≈ 40 M$_\odot$, with a broken-power-law distribution with a break at $M_B = 10.7 \pm 0.8$ M$_\odot$.

Starting in 2025, the Vera C. Rubin Observatory Legacy Survey of Space and Time (Rubin; Ivezić et al. 2019) is planned to commence and expected to discover $\sim 10^4$ SLSNe in the Wide-Fast-Deep survey (Villar et al. 2018). Similarly, in 2027 the Nancy Grace Roman Space Telescope (*Roman*; Spergel et al. 2015) is scheduled to launch and find SLSNe to $z \sim 5$ (Moriya, Quimby & Robertson 2022b; Gomez et al. 2023b). Finding these SNe will allow us to constrain their event rate as a function of redshift, and test how star formation varies with redshift for the most massive progenitor stars (e.g. Madau & Dickinson 2014; Frohmaier et al. 2021). The catalogue presented here can be used to simulate observations of SLSNe that Rubin and *Roman* will observe, to help us better prepare for these surveys. Once these surveys begin, their discoveries will allow us to push the boundaries of our understanding of the SLSN population.

7 CATALOGUE DESCRIPTION

We provide the entire catalogue, including all the photometry, models, and derived parameters as an open-source tool available on GitHub. The package can be easily installed via PYPI with a `pip install slsne` command. Additionally, we provide PYTHON examples on how to access different components of the catalogue and use them to either reproduce plots on this paper or for comparison to other studies. The catalogue is open-source and flexible enough for anyone to contribute their data via a pull request. While we list some examples of how to use the code here, we encourage users to reference the documentation[7] for the must up-to-date syntax and code examples.

In Listing 1, we provide examples on how to obtain the light curves of either individual SLSNe, or light curves for the full sample. These tools can be used to create comparisons such as the one shown in Fig. 7. In Listings 2 and 3, we show examples on how to obtain an accurate *K*-correction or bolometric scaling as a function of wavelength and phase for any SLSN. In Listing 4, we show an example on how to obtain a set of parameters from the SLSN population. For more examples, including scripts used to reproduce the plots in this paper, we encourage the reader to visit the GitHub repository of the catalogue.

We encourage users to cite the original sources of data for all SNe used. Therefore, we provide a function named `get_references`, which can take in a list of SN names, and return all the bibcode entries used for those SNe. If no list is provided, the function will print all the bibcode entries used for all photometry used in this work.

Listing 1. Example of how to obtain the rest-frame model light curves of all SLSNe, as well as a single SLSN.

```
from slsne.lcurve import get_all_lcs
# Get light curves of all SLSNe in r-band
(dim, mean, high), (time_samples, lightcurves) = get_all_lcs('r')
# Get a single light curve
time_samples, r_2018lfe = get_all_lcs('r', names = '2018lfe')
```

Listing 2. Example of how to calculate the *K*-correction for the observed photometry of an SLSN.

```
from slsne.lcurve import get_kcorr, fit_map
from slsne.utils import get_lc
# Import a SLSN light curve, and define a redshift and peak date
phot = get_lc('2013dg')
redshift = 0.265
peak = 56447.62
# Fit the best scaling for the SLSN map
stretch, amplitude, offset = fit_map(phot, redshift, peak = peak)
# Get corresponding K-correction for the photometry
K_corr = get_kcorr(phot, redshift, peak = peak, stretch = stretch,
offset = offset)
# Apply the K-correction to the photometry
corr_mag = phot['Mag'] - K_corr
```

Listing 3. Example of how to calculate the bolometric scaling for an SLSN.

```
from slsne.lcurve import get_bolcorr
from slsne.utils import calc_flux_lum, get_lc
# Import a SLSN light curve
phot = get_lc('2018lfe')
redshift = 0.35
peak = 58468.55
# Calculate the phase with respect to peak
phot['Phase'] = (phot['MJD'] - peak) / (1 + redshift)
# Measure the bolometric scaling
```

[7]https://slsne.readthedocs.io

```
bol_scaling = get_bolcorr(phot, redshift, peak)
# The scaling can then be applied to the luminosity as
F_lambda, L_lambda = calc_flux_lum(phot, redshift)
L_bol = L_lambda.value / bol_scaling
```

Listing 4. Example of how to obtain a sample of parameters. If no `param _names` is specified, all parameters will be returned.

```
from slsne.utils import get_params
# Get the parameters
params = get_params(param_names = ['Pspin','mejecta'])
# The format of the output parameters is an Astropy Table
Pspin_med Pspin_up Pspin_lo mejecta_med mejecta_up mejecta_lo
--------- -------- -------- ----------- ---------- ----------
3.8508    5.3963   2.4987   2.877       4.5832     1.2612
```


ACKNOWLEDGEMENTS

We thank Yuri Beletsky for observing most of the spectra and photometry from the Magellan Telescopes. We thank referee T.-W. Chen for useful comments towards the improvement of this manuscript. SG is supported by an STScI Postdoctoral Fellowship. MN is supported by the European Research Council (ERC) under the European Union's Horizon 2020 research and innovation programme (grant agreement no. 948381) and by UK Space Agency grant no. ST/Y000692/1. This project was supported in part by the Transients Science@Space Telescope group. TE is supported by NASA through the NASA Hubble Fellowship grant HST-HF2-51504.001-A awarded by the Space Telescope Science Institute, which is operated by the Association of Universities for Research in Astronomy, Inc., for NASA, under contract NAS5-26555. This work is supported by the National Science Foundation under cooperative agreement PHY-2019786 (The NSF AI Institute for Artificial Intelligence and Fundamental Interactions, http://iaifi.org/). AF acknowledges the support by the State of Hesse within the Research Cluster ELEMENTS (project ID 500/10.006). VAV acknowledges support from the NSF through grant AST-2108676. RKT is supported by the NKFIH/OTKA FK-134432 and the NKFIH/OTKA K-142534 grants of the National Research, Development and Innovation (NRDI) Office of Hungary. NF acknowledges support from the National Science Foundation Graduate Research Fellowship Program under grant no. DGE-2137419. The LCO group is supported by NSF grants AST-1911151 and 1911225.

W. M. Keck Observatory and MMT Observatory access was supported by Northwestern University and the Center for Interdisciplinary Exploration and Research in Astrophysics (CIERA). This paper includes data gathered with the 6.5-m Magellan Telescopes located at Las Campanas Observatory, Chile. Observations reported here were obtained at the MMT Observatory, a joint facility of the University of Arizona and the Smithsonian Institution. IRAF is written and supported by the National Optical Astronomy Observatories, operated by the Association of Universities for Research in Astronomy, Inc. under cooperative agreement with the National Science Foundation. This work makes use of observations from Las Cumbres Observatory global telescope network. Operation of the Pan-STARRS1 telescope is supported by the National Aeronautics and Space Administration under grant nos NNX12AR65G and NNX14AM74G issued through the NEO Observation Program. This work has made use of data from the European Space Agency (ESA) mission *Gaia* (https://www.cosmos.esa.int/gaia), processed by the *Gaia* Data Processing and Analysis Consortium (DPAC, https://www.cosmos.esa.int/web/gaia/dpac/consortium). Funding for the DPAC has been provided by national institutions, in particular the institutions participating in the *Gaia* Multilateral Agreement. This research has made use of the SIMBAD database, operated at CDS, Strasbourg, France. Based on observations obtained with MegaPrime/MegaCam, a joint project of Canada–France–Hawaii Telescope (CFHT) and CEA/IRFU, at the CFHT which is operated by the National Research Council (NRC) of Canada, the Institut National des Science de l'Univers of the Centre National de la Recherche Scientifique (CNRS) of France, and the University of Hawaii. This work is based in part on data products produced at TERAPIX available at the Canadian Astronomy Data Centre as part of the CFHT Legacy Survey, a collaborative project of NRC and CNRS. This research has made use of the NASA/IPAC Extragalactic Database, which is funded by the National Aeronautics and Space Administration and operated by the California Institute of Technology. This research has made use of NASA's Astrophysics Data System. This research has made use of the NASA/IPAC Infrared Science Archive, which is funded by the National Aeronautics and Space Administration and operated by the California Institute of Technology. This work made use of *Swift*/UVOT data reduced by P. J. Brown and released in the SOUSA. SOUSA is supported by NASA's Astrophysics Data Analysis Program through grant NNX13AF35G. This work makes use of the WISeREP (https://www.wiserep.org).

Facilities: ADS, ASAS, *Gaia*, IRSA, OGLE, OSC, Las Cumbres, PS1, Sloan, SO, *Swift*, TNS, *WISE*.

Software: ASTROPY (Astropy Collaboration 2018), EXTINCTION (Barbary 2016), DUST_EXTINCTION (Gordon 2024), MATPLOTLIB (Hunter 2007), EMCEE (Foreman-Mackey et al. 2013), EXTRABOL (Thornton et al. 2024), NUMPY (van der Walt, Colbert & Varoquaux 2011), SCIKIT-LEARN (Pedregosa et al. 2011), MOSFIT (Guillochon et al. 2018), PYRAF (Science Software Branch at STScI 2012), SAOIMAGE DS9 (Smithsonian Astrophysical Observatory 2000), SLSNE (Gomez 2024), CORNER (Foreman-Mackey 2016), HOTPANTS (Becker 2015), FLEET (Gomez et al. 2020b), and GEORGE (Foreman-Mackey 2015).

DATA AVAILABILITY

All the data, models, and derived parameters used in this work are provided on GitHub[8] and Zenodo (Gomez 2024).

REFERENCES

Aamer A., O'Neill D., Ridley E., Sheng X., Lyman J., Nicholl M., Yaron O., 2022, Transient Name Server Classification Report, 291, 1
Aamer A. et al., 2024, MNRAS, 527, 11970
Aguilera-Dena D. R., Langer N., Moriya T. J., Schootemeijer A., 2018, ApJ, 858, 115
Aguilera-Dena D. R., Langer N., Antoniadis J., Müller B., 2020, ApJ, 901, 114
Aguilera-Dena D. R., Müller B., Antoniadis J., Langer N., Dessart L., Vigna-Gómez A., Yoon S.-C., 2023, A&A, 671, A134
Anderson J. P. et al., 2018, A&A, 620, A67
Angus C., 2022, Transient Name Server Classification Report, 1769, 1
Angus C. R., Levan A. J., Perley D. A., Tanvir N. R., Lyman J. D., Stanway E. R., Fruchter A. S., 2016, MNRAS, 458, 84
Angus C. R., Jones S., Angus C. R., Jones S., Frohmaier C., Yaron O., Knezevic N., 2017, Transient Name Server Classification Report, 1495, 1
Angus C. R. et al., 2019, MNRAS, 487, 2215
Arcavi I., Pellegrino C., 2022, Transient Name Server Classification Report, 3660, 1

[8] https://github.com/gmzsebastian/SLSNe

Arcavi I. et al., 2012, ApJ, 756, L30
Arcavi I. et al., 2016, ApJ, 819, 35
Arcavi I., Burke J., Hiramatsu D., McCully C., Howell D. A., Valenti S., 2018, Astron. Telegram, 12183, 1
Arnett W. D., 1982, ApJ, 253, 785
Astropy Collaboration, 2018, AJ, 156, 123
Ayala B., Gutierrez C., Kravtsov T., Yaron O., 2022a, Transient Name Server Classification Report, 2393, 1
Ayala B. et al., 2022b, Transient Name Server AstroNote, 177, 1
Barbarino C. et al., 2021, A&A, 651, A81
Barbary K., 2016, Extinction V0.3.0. Zenodo, available at: https://zenodo.org/records/804967
Barbary K. et al., 2009, ApJ, 690, 1358
Becker A., 2015, Astrophysics Source Code Library, record ascl:1504.004
Bellm E. C. et al., 2019, PASP, 131, 018002
Benetti S., Branch D., Turatto M., Cappellaro E., Baron E., Zampieri L., Della Valle M., Pastorello A., 2002, MNRAS, 336, 91
Benetti S. et al., 2018, MNRAS, 476, 261
Berger E. et al., 2012, ApJ, 755, L29
Berlind P., Calkins M., Jha S., 1999, IAU Circ., 7162, 3
Bhirombhakdi K., Chornock R., Margutti R., Nicholl M., Metzger B. D., Berger E., Margalit B., Milisavljevic D., 2018, ApJ, 868, L32
Blanchard P., Gomez S., Berger E., Nicholl M., Kattner S., Weiner B., 2018a, Astron. Telegram, 11714, 1
Blanchard P., Nicholl M., Berger E., 2018b, Transient Name Server Classification Report, 2018-2025, 1
Blanchard P. K. et al., 2018c, ApJ, 865, 9
Blanchard P. K., Nicholl M., Berger E., Chornock R., Milisavljevic D., Margutti R., Gomez S., 2019, ApJ, 872, 90
Blanchard P., Gomez S., Hosseinzadeh G., Berger E., 2020a, Transient Name Server Classification Report, 3871, 1
Blanchard P. K., Berger E., Nicholl M., Villar V. A., 2020b, ApJ, 897, 114
Blanchard P., Berger E., Gomez S., Hosseinzadeh G., 2021a, Transient Name Server Classification Report, 276, 1
Blanchard P., Chornock R., Nicholl M., Berger E., Gomez S., Hosseinzadeh G., 2021b, Transient Name Server Classification Report, 2021-1566, 1
Blanchard P. K., Berger E., Nicholl M., Chornock R., Gomez S., Hosseinzadeh G., 2021c, ApJ, 921, 64
Blanchard P. K., Davis K., Bustamante-Rosell M. J., French K. D., Villar V. A., Yadavalli S. K., Foley R. J., Tinyanont S., 2022a, Transient Name Server AstroNote, 101, 1
Blanchard P. K., Davis K., Bustamante-Rosell M. J., French K. D., Villar V. A., Yadavalli S. K., Foley R. J., Tinyanont S., 2022b, Transient Name Server Classification Report, 1188, 1
Bose S. et al., 2018, ApJ, 853, 57
Brown T. M. et al., 2013, PASP, 125, 1031
Brown P. J., Breeveld A. A., Holland S., Kuin P., Pritchard T., 2014, Ap&SS, 354, 89
Bruch R., Anderson J., Gutierrez C., Irani I., 2021, Transient Name Server Classification Report, 3392, 1
Campbell H. et al., 2014, Astron. Telegram, 6524, 1
Cardelli J. A., Clayton G. C., Mathis J. S., 1989, ApJ, 345, 245
Cartier R. et al., 2022, MNRAS, 514, 2627
Casas R. et al., 2016, Astron. Telegram, 8717, 1
Chambers K. C. et al., 2016, preprint (arXiv:1612.05560)
Chatzopoulos E., Wheeler J. C., Vinko J., 2009, ApJ, 704, 1251
Chatzopoulos E., Wheeler J. C., Vinko J., Horvath Z. L., Nagy A., 2013, ApJ, 773, 76
Chen T., 2019, Transient Name Server Classification Report, 938, 1
Chen T. W. et al., 2015, MNRAS, 452, 1567
Chen T. W. et al., 2017b, A&A, 602, A9
Chen T. W. et al., 2018, ApJ, 867, L31
Chen T. W. et al., 2019, Astron. Telegram, 12604, 1
Chen T. W. et al., 2021, preprint (arXiv:2109.07942)
Chen T.-W. et al., 2013, ApJ, 763, L28
Chen Z. H. et al., 2023a, ApJ, 943, 41
Chen Z. H. et al., 2023b, ApJ, 943, 42
Chen T.-W., Smartt S. J., Yates R. M., Nicholl M., Krühler T., Schady P., Dennefeld M., Inserra C., 2017a, MNRAS, 470, 3566
Chevalier R. A., Irwin C. M., 2011, ApJ, 729, L6
Chomiuk L. et al., 2011, ApJ, 743, 114
Chu M., Dahiwale A., Fremling C., 2021a, Transient Name Server Classification Report, 2748, 1
Chu M., Dahiwale A., Fremling C., 2021b, Transient Name Server Classification Report, 3171, 1
Chu M., Dahiwale A., Fremling C., 2022, Transient Name Server Classification Report, 1071, 1
Cikota A. et al., 2018, MNRAS, 479, 4984
Clark P., McBrien O., Magee M., Yaron O., Knezevic N., 2018, Transient Name Server Classification Report, 2100, 1
Cooke J. et al., 2012, Nature, 491, 228
Dahiwale A., Fremling C., 2019, Transient Name Server Classification Report, 2889, 1
Dahiwale A., Fremling C., 2020a, Transient Name Server Classification Report, 1494, 1
Dahiwale A., Fremling C., 2020b, Transient Name Server Classification Report, 1504, 1
Dahiwale A., Fremling C., 2020c, Transient Name Server Classification Report, 1667, 1
Dahiwale A., Fremling C., 2020d, Transient Name Server Classification Report, 1756, 1
Dahiwale A., Fremling C., 2021, Transient Name Server Classification Report, 1234, 1
Dahiwale A., Dugas A., Fremling C., 2019a, Transient Name Server Classification Report, 2859, 1
Dahiwale A., Fremling C., Sharma Y., 2019b, Transient Name Server Classification Report, 2837, 1
Davis K., Foley R., Dimitriadis G., Soto K. D., 2022, Transient Name Server Classification Report, 1881, 1
De Cia A. et al., 2018, ApJ, 860, 100
Deckers M., Prentice S., Maguire K., Dimitriadis G., Magee M., Harvey L., Terwel J., 2021a, Transient Name Server AstroNote, 136, 1
Deckers M., Prentice S., Maguire K., Dimitriadis G., Magee M., Harvey L., Terwel J., 2021b, Transient Name Server Classification Report, 1365, 1
Decleir M. et al., 2022, ApJ, 930, 15
Deng J. S., Hatano K., Nakamura T., Maeda K., Nomoto K., Nugent P., Aldering G., Branch D., 2001, in Inoue H., Kunieda H., eds, ASP Conf. Proc. Vol. 251, New Century of X-ray Astronomy. Astron. Soc. Pac., San Francisco, p. 238
Dessart L., 2019, A&A, 621, A141
Dessart L., Hillier D. J., Waldman R., Livne E., Blondin S., 2012, MNRAS, 426, L76
Dexter J., Kasen D., 2013, ApJ, 772, 30
Dong S., 2017, Transient Name Server Classification Report, 2017-1527, 1
Dong S., 2018, Transient Name Server Classification Report, 673, 1
Dong S. et al., 2018, Astron. Telegram, 11654, 1
Dong X.-F., Liu L.-D., Gao H., Yang S., 2023, ApJ, 951, 61
Drake A. J. et al., 2009a, ApJ, 696, 870
Drake A. J. et al., 2009b, Central Bureau Electronic Telegram, 1958, 1
Drake A. J. et al., 2011, Astron. Telegram, 3343, 1
Drake A. J. et al., 2012, Astron. Telegram, 3873, 1
Drake A. J. et al., 2013, Central Bureau Electronic Telegram, 3560, 1
Drake A. J., Djorgovski S. G., Mahabal A. A., Graham M. J., Stern D., Catelan M., Christensen E., Larson S. M., 2016, Astron. Telegram, 9319, 1
Dressler A. et al., 2011, PASP, 123, 288
Eftekhari T. et al., 2021, ApJ, 912, 21
Elias-rosa N., 2016, Transient Name Server Classification Report, 2016-791, 1
Fabricant D. et al., 2019, PASP, 131, 075004
Fatkhullin T., Gabdeev M., 2012, Astron. Telegram, 4599, 1
Filippenko A. V., 1997, ARA&A, 35, 309
Fiore A. et al., 2021, MNRAS, 502, 2120
Fiore A. et al., 2022, MNRAS, 512, 4484
Fiore A. et al., 2024, MNRAS, 527, 6473

Fitzpatrick E. L., Massa D., Gordon K. D., Bohlin R., Clayton G. C., 2019, ApJ, 886, 108
Foreman-Mackey D., 2015, Astrophysics Source Code Library, record ascl:1511.015
Foreman-Mackey D., 2016, J. Open Source Softw., 1, 24
Foreman-Mackey D., Hogg D. W., Lang D., Goodman J., 2013, PASP, 125, 306
Förster F. et al., 2021, AJ, 161, 242
Fraser M., Reynolds T., Mattila S., Yaron O., 2016, Transient Name Server Classification Report, 521, 1
Fremling C., Dahiwale A., 2019a, Transient Name Server Classification Report, 2852, 1
Fremling C., Dahiwale A., 2019b, Transient Name Server Classification Report, 1774, 1
Fremling C., Sharma Y., 2018, Transient Name Server Classification Report, 815, 1
Fremling C., Dugas A., Sharma Y., 2018a, Transient Name Server Classification Report, 1232, 1
Fremling C., Dugas A., Sharma Y., 2018b, Transient Name Server Classification Report, 2145, 1
Fremling C., Dugas A., Sharma Y., 2018c, Transient Name Server Classification Report, 1411, 1
Fremling C., Dugas A., Sharma Y., 2018d, Transient Name Server Classification Report, 1416, 1
Fremling C., Dugas A., Sharma Y., 2018e, Transient Name Server Classification Report, 1870, 1
Fremling C., Dugas A., Sharma Y., 2018f, Transient Name Server Classification Report, 1877, 1
Fremling C., Dahiwale A., Dugas A., 2019a, Transient Name Server Classification Report, 1923, 1
Fremling C., Dugas A., Sharma Y., 2019b, Transient Name Server Classification Report, 188, 1
Fremling C., Dugas A., Sharma Y., 2019c, Transient Name Server Classification Report, 32, 1
Fremling C., Dugas A., Sharma Y., 2019d, Transient Name Server Classification Report, 598, 1
Fremling C., Dugas A., Sharma Y., 2019e, Transient Name Server Classification Report, 636, 1
Fremling C., Dugas A., Sharma Y., 2019f, Transient Name Server Classification Report, 747, 1
Fremling C., Dugas A., Sharma Y., 2019g, Transient Name Server Classification Report, 799, 1
Fremling C., Dugas A., Sharma Y., 2019h, Transient Name Server Classification Report, 952, 1
Fremling C., Sharma Y., Dahiwale A., 2019i, Transient Name Server Classification Report, 1838, 1
Frohmaier C. et al., 2019, Transient Name Server AstroNote, 27, 1
Frohmaier C. et al., 2021, MNRAS, 500, 5142
Fulton M., Smith K. W., Moore T., Srivastav S., Bruch R. J., 2022a, Transient Name Server Classification Report, 584, 1
Fulton M. et al., 2022b, Transient Name Server AstroNote, 55, 1
Fulton M. et al., 2022c, Transient Name Server Classification Report, 2128, 1
Gagliano A., Contardo G., Foreman-Mackey D., Malz A. I., Aleo P. D., 2023, ApJ, 954, 6
Gal-Yam A., 2012, Science, 337, 927
Gal-Yam A., 2019a, ApJ, 882, 102
Gal-Yam A., 2019b, Transient Name Server Classification Report, 423, 1
Gal-Yam A., 2019c, ARA&A, 57, 305
Gal-Yam A., Cenko S. B., Fox D. B., Leonard D. C., Moon D. S., Sand D. J., Soderberg A. M., 2007, in AIP Conf. Proc. Vol. 924, The Multicolored Landscape of Compact Objects and their Explosive Origins. Am. Inst. Phys., New York, p. 297
Gal-Yam A. et al., 2009, Nature, 462, 624
Gal-Yam A. et al., 2017, GCN Circ., 20721, 1
Galbany L. et al., 2014, Astron. Telegram, 6622, 1
Garcia-Zamora E. M. et al., 2018, Astron. Telegram, 12344, 1
Gelman A., Rubin D. B., 1992, Stat. Sci., 7, 457
Gillanders J., Srivastav S., Fulton M., Shingles L. J., Smith K. W., Zimmerman E., 2021, Transient Name Server Classification Report, 86, 1
Gkini A. et al., 2024, A&A, 685, A20
Gomez S., 2019, Transient Name Server Classification Report, 2019-1246, 1
Gomez S., 2024, gmzsebastian/SLSNe: SLSNe Version 0.1.0, v0.1.0. Zenodo, available at: https://zenodo.org/records/13732133
Gomez S., Berger E., Blanchard P. K., Hosseinzadeh G., Nicholl M., Villar V. A., Yin Y., 2020a, ApJ, 904, 74
Gomez S., Berger E., Blanchard P. K., Hosseinzadeh G., Nicholl M., Villar V. A., Yin Y., 2020b, FLEET Finding Luminous and Exotic Extragalactic Transients, 1.0.0. Zenodo, available at: https://zenodo.org/records/4013965
Gomez S., Hosseinzadeh G., Berger E., Blanchard P., 2020c, Transient Name Server Classification Report, 3149, 1
Gomez S., Hosseinzadeh G., Berger E., Blanchard P., 2020d, Transient Name Server Classification Report, 3506, 1
Gomez S., Berger E., Blanchard P., Nicholl M., 2021a, Transient Name Server Classification Report, 564, 1
Gomez S., Berger E., Blanchard P., Nicholl M., 2021b, Transient Name Server Classification Report, 1675, 1
Gomez S., Berger E., Hosseinzadeh G., Blanchard P. K., Nicholl M., Villar V. A., 2021c, ApJ, 913, 143
Gomez S., Hosseinzadeh G., Berger E., Blanchard P., 2021d, Transient Name Server Classification Report, 565, 1
Gomez S., Hosseinzadeh G., Berger E., Blanchard P., 2021e, Transient Name Server Classification Report, 1647, 1
Gomez S., Hosseinzadeh G., Berger E., Blanchard P., 2021f, Transient Name Server Classification Report, 1716, 1
Gomez S., Hosseinzadeh G., Berger E., Blanchard P., 2021g, Transient Name Server Classification Report, 2719, 1
Gomez S., Hosseinzadeh G., Berger E., Blanchard P., 2021h, Transient Name Server Classification Report, 3270, 1
Gomez S., Hosseinzadeh G., Blanchard P., Berger E., 2021i, Transient Name Server Classification Report, 3662, 1
Gomez S., Hosseinzadeh G., Blanchard P., Berger E., 2021j, Transient Name Server Classification Report, 3444, 1
Gomez S., Berger E., Nicholl M., Blanchard P. K., Hosseinzadeh G., 2022a, ApJ, 941, 107
Gomez S., Hiramatsu D., Blanchard P., Berger E., 2022b, Transient Name Server Classification Report, 777, 1
Gomez S., Berger E., Blanchard P. K., Hosseinzadeh G., Nicholl M., Hiramatsu D., Villar V. A., Yin Y., 2023a, ApJ, 949, 114
Gomez S. et al., 2023b, preprint (arXiv:2306.17233)
Gomez S. et al., 2024, preprint (arXiv:2408.15397)
Gonzalez E. P., Hiramatsu D., Burke J., Howell D. A., McCully C., Pellegrino C., 2021, Transient Name Server Classification Report, 1220, 1
Gordon K., 2024, dust_extinction, v1.4.1. Zenodo, available at: https://zenodo.org/records/11235336
Gordon K. D., Cartledge S., Clayton G. C., 2009, ApJ, 705, 1320
Gordon K. D. et al., 2021, ApJ, 916, 33
Gordon K. D., Clayton G. C., Decleir M., Fitzpatrick E. L., Massa D., Misselt K. A., Tollerud E. J., 2023, ApJ, 950, 86
Graham M. J. et al., 2011a, Astron. Telegram, 3477, 1
Graham M. J. et al., 2011b, Central Bureau Electronic Telegram, 2787, 1
Graham M. J. et al., 2019, PASP, 131, 078001
Greiner J. et al., 2015, Nature, 523, 189
Gromadzki M., Wevers T., Lyman J., Yaron O., 2018, Transient Name Server Classification Report, 1396, 1
Gromadzki M., Ihanec N., Moran S., Yaron O., 2020, Transient Name Server Classification Report, 3372, 1
Gromadzki M., Cartier R., Yaron O., 2021, Transient Name Server Classification Report, 3651, 1
Gromadzki M. et al., 2022, Transient Name Server AstroNote, 253, 1
Guillochon J., Parrent J., Kelley L. Z., Margutti R., 2017, ApJ, 835, 64
Guillochon J., Nicholl M., Villar V. A., Mockler B., Narayan G., Mandel K. S., Berger E., Williams P. K. G., 2018, ApJS, 236, 6
Guillou L. L., 2016, Transient Name Server Classification Report, 2016-148, 1

Gullin S., 2019, Bachelor's thesis, Stockholm University, available at: https://www.diva-portal.org/smash/get/diva2:1330469/FULLTEXT01.pdf
Gutiérrez C. P. et al., 2022, MNRAS, 517, 2056
Hart K. et al., 2023, preprint (arXiv:2304.03791)
Harvey L., Deckers M., Dimitriadis G., Burgaz U., Yaron O., 2022a, Transient Name Server Classification Report, 2997, 1
Harvey L. et al., 2022b, Transient Name Server AstroNote, 213, 1
Hatano K., Maeda K., Deng J. S., Nomoto K., Branch D., Nugent P., Aldering G., 2001, in Inoue H., Kunieda H., eds, ASP Conf. Ser. Vol. 251, New Century of X-ray Astronomy. Astron. Soc. Pac., San Francisco, p. 244
Hatsukade B. et al., 2018, ApJ, 857, 72
Heger A., Woosley S. E., 2002, ApJ, 567, 532
Hinkle J., 2022, Transient Name Server Classification Report, 601, 1
Hinkle J. T., Shappee B. J., Tucker M. A., 2023, preprint (arXiv:2309.03270)
Hiramatsu D., Arcavi I., Burke J., Hosseinzadeh G., Howell D. A., Mccully C., Valenti S., 2018, Transient Name Server Classification Report, 2018-679, 1
Hogg D. W., Baldry I. K., Blanton M. R., Eisenstein D. J., 2002, preprint(arXiv:astro-ph/0210394)
Hosseinzadeh G. et al., 2020, ApJ, 905, 93
Hosseinzadeh G., Berger E., Metzger B. D., Gomez S., Nicholl M., Blanchard P., 2022, ApJ, 933, 14
Howell D. A., 2017, in Alsabti A. W., Murdin P., eds, Handbook of Supernovae. Springer International Publishing AG, p. 431
Howell D. A. et al., 2013, ApJ, 779, 98
Hsu B., Hosseinzadeh G., Berger E., 2021, ApJ, 921, 180
Hsu B., Hosseinzadeh G., Villar V. A., Berger E., 2022, ApJ, 937, 13
Hsu B., Blanchard P. K., Berger E., Gomez S., 2024, ApJ, 961, 169
Huber M. et al., 2015, Astron. Telegram, 7153, 1
Hueichapan E. D. et al., 2022, MNRAS, 513, 2965
Hunter J. D., 2007, Comput. Sci. Eng., 9, 90
Ihanec N., Gromadzki M., Byrne R., Brennan S., Fraser M., Irani I., 2020a, Transient Name Server Classification Report, 3411, 1
Ihanec N., Gromadzki M., Wevers T., Irani I., 2020b, Transient Name Server Classification Report, 3296, 1
Ihanec N., Gromadzki M., Wevers T., Irani I., 2020c, Transient Name Server Classification Report, 3486, 1
Inserra C., Smartt S. J., 2014, ApJ, 796, 87
Inserra C. et al., 2012, Astron. Telegram, 4329, 1
Inserra C. et al., 2013, ApJ, 770, 128
Inserra C. et al., 2017, MNRAS, 468, 4642
Inserra C., Prajs S., Gutierrez C. P., Angus C., Smith M., Sullivan M., 2018a, ApJ, 854, 175
Inserra C. et al., 2018b, MNRAS, 475, 1046
Inserra C. et al., 2021, MNRAS, 504, 2535
Ivezić Ž. et al., 2019, ApJ, 873, 111
Izzo L. et al., 2018, A&A, 610, A11
Jaeger T. D., Huber M., 2020, Transient Name Server Classification Report, 3720, 1
Japelj J., Vergani S. D., Salvaterra R., Hunt L. K., Mannucci F., 2016, A&A, 593, A115
Jerkstrand A. et al., 2017, ApJ, 835, 13
Justham S., Podsiadlowski P., Vink J. S., 2014, ApJ, 796, 121
Kangas T. et al., 2022, MNRAS, 516, 1193
Kann D. A. et al., 2019, A&A, 624, A143
Kasen D. N., 2004, PhD thesis, University of California, Berkeley, California, USA
Kasen D., Bildsten L., 2010, ApJ, 717, 245
Kasen D., Woosley S. E., Heger A., 2011, ApJ, 734, 102
Kasen D., Metzger B. D., Bildsten L., 2016, ApJ, 821, 36
Kasliwal M. M. et al., 2009, Central Bureau Electronic Telegram, 1732, 1
Kirshner R. P., Oemler A. J., Schechter P. L., Shectman S. A., 1983, AJ, 88, 1285
Knop R. et al., 1999, IAU Circ., 7128, 1
Kochanek C. S. et al., 2017, PASP, 129, 104502
Kodros J., Cenko S. B., Li W., Filippenko A. V., Kandrashoff M. T., Silverman J. M., 2010, Central Bureau Electronic Telegram, 2461, 1
Könyves-Tóth R., Seli B., 2023, ApJ, 954, 44
Könyves-Tóth R., Thomas B. P., Vinkó J., Wheeler J. C., 2020, ApJ, 900, 73
Kostrzewa-Rutkowska Z., Kozłowski S., Wyrzykowski Ł., Djorgovski S. G., Glikman E., Mahabal A. A., Koposov S., 2013, ApJ, 778, 168
Kostrzewa-Rutkowska Z., Wyrzykowski L., Kozlowski S., Udalski A., Greiner J., Knust F., 2015, Astron. Telegram, 8314, 1
Kostrzewa-rutkowska Z., Callis E., Fraser M., Yaron O., 2018, Transient Name Server Classification Report, 1212, 1
Kozyreva A., Blinnikov S., 2015, MNRAS, 454, 4357
Kozyreva A., Shingles L., Baklanov P., Mironov A., Schneider F. R. N., 2024, A&A, 689, A60
Kumar A. et al., 2020, ApJ, 892, 28
Kumar A. et al., 2021, MNRAS, 502, 1678
Kumar A. et al., 2024, MNRAS, 531, 3297
Le Breton R. et al., 2015, Astron. Telegram, 8437, 1
Le Guillou L. et al., 2015, Astron. Telegram, 7102, 1
Lee C.-H., 2020, Astron. Nachr., 341, 651
Leloudas G. et al., 2012, A&A, 541, A129
Leloudas G. et al., 2015a, ApJ, 815, L10
Leloudas G. et al., 2015b, MNRAS, 449, 917
Leloudas G. et al., 2017, ApJ, 837, L14
Li W., Rui L., Wang X., Yang Q., Wu X., Zhang T., 2014a, Astron. Telegram, 6183, 1
Li W.-x., Wang X.-f., Mo J., Zhang T.-m., Brimacombe J., Masi G., 2014b, Central Bureau Electronic Telegram, 3895, 1
Li S., Liang Y.-F., Liao N.-H., Lei L., Fan Y.-Z., 2024, preprint (arXiv:2407.05968)
Lin W. L., Wang X. F., Wang L. J., Dai Z. G., 2020a, ApJ, 903, L24
Lin W. L. et al., 2020b, MNRAS, 497, 318
Lin W. et al., 2023, Nat. Astron., 7, 779
Liu Y.-Q., Modjaz M., Bianco F. B., 2017, ApJ, 845, 85
Liu L.-D., Wang L.-J., Wang S.-Q., Dai Z.-G., 2018a, ApJ, 856, 59
Liu L.-D., Zhang B., Wang L.-J., Dai Z.-G., 2018b, ApJ, 868, L24
Liu J.-F., Zhu J.-P., Liu L.-D., Yu Y.-W., Zhang B., 2022, ApJ, 935, L34
Lunnan R., Schulze S., 2021, Transient Name Server Classification Report, 207, 1
Lunnan R. et al., 2013, ApJ, 771, 97
Lunnan R. et al., 2014, ApJ, 787, 138
Lunnan R. et al., 2015, ApJ, 804, 90
Lunnan R. et al., 2016, ApJ, 831, 144
Lunnan R., Yan L., Fremling C., Dugas A., Sharma Y., Schulze S., Perley D. A., 2018a, Astron. Telegram, 11986, 1
Lunnan R. et al., 2018b, Nat. Astron., 2, 887
Lunnan R. et al., 2018c, ApJ, 852, 81
Lunnan R. et al., 2020, ApJ, 901, 61
Lyman J., Homan D., Magee M., Yaron O., 2017a, Transient Name Server Classification Report, 881, 1
Lyman J., Homan D., Magee M., Yaron O., 2017b, Transient Name Server Classification Report, 1534, 1
Madau P., Dickinson M., 2014, ARA&A, 52, 415
Magee M., Terwel J., Prentice S., Harvey L., Strotjohann N. L., 2021, Transient Name Server Classification Report, 338, 1
Mahabal A. A., Drake A. J., 2010, Astron. Telegram, 2508, 1
Mahabal A. A. et al., 2010, Astron. Telegram, 2490, 1
Margalit B., Metzger B. D., Berger E., Nicholl M., Eftekhari T., Margutti R., 2018a, MNRAS, 481, 2407
Margalit B., Metzger B. D., Thompson T. A., Nicholl M., Sukhbold T., 2018b, MNRAS, 475, 2659
Margutti R. et al., 2018, ApJ, 864, 45
Matheson T., Filippenko A. V., Li W., Leonard D. C., Shields J. C., 2001, AJ, 121, 1648
Mattila S. et al., 2016, Astron. Telegram, 9308, 1
Maund J. R. et al., 2021, MNRAS, 503, 312
Mazzali P. A., Sullivan M., Pian E., Greiner J., Kann D. A., 2016, MNRAS, 458, 3455
Mcbrien O., Clark P., Kankare E., Yaron O., Knezevic N., 2018, Transient Name Server Classification Report, 587, 1
McCrum M. et al., 2014, MNRAS, 437, 656
McCrum M. et al., 2015, MNRAS, 448, 1206

Metzger B. D., Berger E., Margalit B., 2017, ApJ, 841, 14
Moriya T. J., Nicholl M., Guillochon J., 2018a, ApJ, 867, 113
Moriya T. J., Sorokina E. I., Chevalier R. A., 2018b, Space Sci. Rev., 214, 59
Moriya T. J., Mazzali P. A., Tanaka M., 2019, MNRAS, 484, 3443
Moriya T. J., Murase K., Kashiyama K., Blinnikov S. I., 2022a, MNRAS, 513, 6210
Moriya T. J., Quimby R. M., Robertson B. E., 2022b, ApJ, 925, 211
Nagele C., Umeda H., Maeda K., 2024, ApJ, 972, 11
Neill J., 2017, Transient Name Server Classification Report, 1084, 1
Neill J. D. et al., 2011, ApJ, 727, 15
Nicholl M., 2018, Res. Notes Am. Astron. Soc., 2, 230
Nicholl M. et al., 2013, Nature, 502, 346
Nicholl M. et al., 2014, MNRAS, 444, 2096
Nicholl M. et al., 2015a, ApJ, 807, L18
Nicholl M. et al., 2015b, MNRAS, 452, 3869
Nicholl M. et al., 2016a, ApJ, 826, 39
Nicholl M. et al., 2016b, ApJ, 828, L18
Nicholl M., Berger E., Margutti R., Blanchard P. K., Guillochon J., Leja J., Chornock R., 2017a, ApJ, 845, L8
Nicholl M., Berger E., Margutti R., Blanchard P. K., Milisavljevic D., Challis P., Metzger B. D., Chornock R., 2017b, ApJ, 835, L8
Nicholl M., Guillochon J., Berger E., 2017c, ApJ, 850, 55
Nicholl M., Gomez S., Blanchard P., Berger E., 2018a, Transient Name Server Classification Report, 653, 1
Nicholl M. et al., 2018b, ApJ, 866, L24
Nicholl M., Berger E., Blanchard P. K., Gomez S., Chornock R., 2019a, ApJ, 871, 102
Nicholl M., Short P., Lawrence A., Ross N., Smartt S., Oates S., 2019b, Transient Name Server Classification Report, 2271, 1
Nugent P. E., 2007, Central Bureau Electronic Telegram, 929, 1
Omand C. M. B., Jerkstrand A., 2023, A&A, 673, A107
Omand C. M. B., Sarin N., 2024, MNRAS, 527, 6455
Ørum S. V., Ivens D. L., Strandberg P., Leloudas G., Man A. W. S., Schulze S., 2020, A&A, 643, A47
Ouyed R., Leahy D., 2013, Res. Astron. Astrophys., 13, 1202
Özel F., Freire P., 2016, ARA&A, 54, 401
Pan Y. C. et al., 2017, MNRAS, 470, 4241
Papadopoulos A. et al., 2015, MNRAS, 449, 1215
Pastorello A. et al., 2010, ApJ, 724, L16
Pearce A., Napoleao T. A., Baransky A., 1999, IAU Circ., 7157, 4
Pedregosa F. et al., 2011, J. Mach. Learn. Res., 12, 2825
Perez-Fournon I. et al., 2020, Astron. Telegram, 13936, 1
Perez-Fournon I. et al., 2022, Transient Name Server Classification Report, 2201, 1
Perley D. A. et al., 2016, ApJ, 830, 13
Perley D., Yan L., Andreoni I., Karambelkar V., Sharma Y., De K., Fremling C., Kulkarni S., 2019a, Transient Name Server Classification Report, 1712, 1
Perley D., Yan L., Lunnan R., Gal-Yam A., Schulze S., Yaron O., 2019b, Transient Name Server Classification Report, 2829, 1
Perley D., Yan L., Lunnan R., Gal-Yam A., Schulze S., Yaron O., 2019c, Transient Name Server Classification Report, 1186, 1
Perley D. A., Yan L., Gal-Yam A., Schulze S., Taggart K., Bruch R., Sollerman J., 2019d, Transient Name Server AstroNote, 79, 1
Perley D., Sollerman J., Fremling C., Dahiwale A., Walters R., 2020a, Transient Name Server Classification Report, 3125, 1
Perley D. A., Taggart K., Dahiwale A., Fremling C., 2020b, Transient Name Server Classification Report, 1749, 1
Perley D. A., Yao Y., Chen T., Schulze S., Sharma Y., Ho A. Y. Q., Yan L., Kulkarni S. R., 2021, Transient Name Server Classification Report, 1649, 1
Perley Y., Group Z. S. , 2022a, Transient Name Server Classification Report, 49, 1
Perley D., Meynardie W., Chu M., Fremling C., 2022b, Transient Name Server Classification Report, 3555, 1
Pessi P. J. et al., 2024, preprint (arXiv:2408.15086)
Planck Collaboration VI, 2020, A&A, 641, A6
Poidevin F. et al., 2020a, Astron. Telegram, 13489, 1
Poidevin F. et al., 2020b, Transient Name Server Classification Report, 500, 1
Poidevin F. et al., 2021, Transient Name Server Classification Report, 2271, 1
Poidevin F., Omand C. M. B., Pérez-Fournon I., Clavero R., Shirley R., Marques-Chaves R., Jimenez Angel C., Geier S., 2022a, MNRAS, 511, 5948
Poidevin F. et al., 2022b, Transient Name Server Classification Report, 1175, 1
Poidevin F. et al., 2022c, Transient Name Server Classification Report, 3606, 1
Poidevin F. et al., 2022d, Astron. Telegram, 15811, 1
Poidevin F. et al., 2023, MNRAS, 521, 5418
Prajs S. et al., 2017, MNRAS, 464, 3568
Prentice S. et al., 2016, Astron. Telegram, 9542, 1
Prentice S. J., Maguire K., Skillen K., Magee M. R., Clark P., 2019, Transient Name Server Classification Report, 2339, 1
Prentice S. J. et al., 2021, MNRAS, 508, 4342
Prieto J. L. et al., 2012, Astron. Telegram, 3883, 1
Pursiainen M., Castro-Segura N., Smith M., Yaron O., 2018, Transient Name Server Classification Report, 2184, 1
Pursiainen M. et al., 2022, A&A, 666, A30
Quimby R., 2009, Central Bureau Electronic Telegram, 2000, 1
Quimby R., Mondol P., Hoeflich P., Wheeler J. C., Gerardy C., Roman B., Riley V., 2005, Central Bureau Electronic Telegram, 116, 1
Quimby R. M., Aldering G., Wheeler J. C., Höflich P., Akerlof C. W., Rykoff E. S., 2007, ApJ, 668, L99
Quimby R. M., Kulkarni S. R., Ofek E., Kasliwal M. M., Levitan D., Gal-Yam A., Cenko S. B., 2010a, Astron. Telegram, 2492, 1
Quimby R. M. et al., 2010b, Astron. Telegram, 2740, 1
Quimby R. M., Gal-Yam A., Arcavi I., Yaron O., Horesh A., Mooley K., 2011a, Astron. Telegram, 3841, 1
Quimby R. M., Sternberg A., Matheson T., 2011b, Astron. Telegram, 3344, 1
Quimby R. M. et al., 2011c, Nature, 474, 487
Quimby R. M. et al., 2013a, Central Bureau Electronic Telegram, 3461, 1
Quimby R. M. et al., 2013b, Central Bureau Electronic Telegram, 3464, 1
Quimby R. M. et al., 2018, ApJ, 855, 2
Rest S. et al., 2024, preprint (arXiv:2405.03747)
Ridley E., Gompertz B., Nicholl M., Galbany L., Yaron O., 2021, Transient Name Server Classification Report, 2795, 1
Rousseeuw P. J., 1987, J. Comput. Appl. Math., 20, 53
Roy R., 2012, PhD thesis, Aryabhatta Research Institute of Observational Sciences (ARIES), Manora Peak, Nainital 263 129, India
Roy R. et al., 2016, A&A, 596, A67
Saito S. et al., 2020, ApJ, 894, 154
Sako M. et al., 2018, PASP, 130, 064002
Schlafly E. F., Finkbeiner D. P., 2011, ApJ, 737, 103
Schulze S. et al., 2018, MNRAS, 473, 1258
Schulze S. et al., 2021, ApJS, 255, 29
Schulze S. et al., 2024, A&A, 683, A223
Schwarz G., 1978, Ann. Stat., 6, 461
Science Software, 2012, Astrophysics Source Code Library, record ascl:1207.011
Scovacricchi D., Nichol R. C., Bacon D., Sullivan M., Prajs S., 2016, MNRAS, 456, 1700
Shappee B. J. et al., 2014, ApJ, 788, 48
Sheng X. et al., 2024, MNRAS, 531, 2474
Shingles L. et al., 2021, Transient Name Server AstroNote, 7, 1
Shivvers I. et al., 2019, MNRAS, 482, 1545
Short P., Nicholl M., Muller T., Angus C., Yaron O., 2019, Transient Name Server Classification Report, 772, 1
Smartt S. J. et al., 2011, Astron. Telegram, 3351, 1
Smartt S. J. et al., 2012, Astron. Telegram, 3918, 1
Smartt S. J., Nicholl M., Inserra C., Wright D., Chen T. W., Lawrence A., Mead A., 2013, Astron. Telegram, 5128, 1
Smith M., 2019, Transient Name Server Classification Report, 522, 1
Smith N. et al., 2007, ApJ, 666, 1116
Smith M. et al., 2014, Astron. Telegram, 6739, 1

Smith M. et al., 2016, ApJ, 818, L8
Smith M. et al., 2018, ApJ, 854, 37
Smith K. W. et al., 2020, PASP, 132, 085002
Smith K. W., Fulton M., Moore T., Srivastav S., Yaron O., 2022, Transient Name Server Classification Report, 583, 1
Smithsonian Astrophysical, 2000, Astrophysics Source Code Library, record ascl:0003.002
Soker N., 2022, ApJ, 935, 108
Soker N., Gilkis A., 2017, ApJ, 851, 95
Sollerman J., 2022, Transient Name Server Classification Report, 1899, 1
Spergel D. et al., 2015, preprint (arXiv:1503.03757)
Srivastav S. et al., 2021, Transient Name Server AstroNote, 11, 1
Srivastav S., Fulton M., Moore T., Yaron O., 2022a, Transient Name Server Classification Report, 667, 1
Srivastav S. et al., 2022b, Transient Name Server AstroNote, 61, 1
Stevance H. F., Eldridge J. J., 2021, MNRAS, 504, L51
Stevenson K. B., Bean J. L., Seifahrt A., Gilbert G. J., Line M. R., Désert J.-M., Fortney J. J., 2016, ApJ, 817, 141
Stoughton C. et al., 2002, AJ, 123, 485
Sukhbold T., Woosley S. E., 2016, ApJ, 820, L38
Sukhbold T., Woosley S. E., Heger A., 2018, ApJ, 860, 93
Sun L., Xiao L., Li G., 2022, MNRAS, 513, 4057
Taddia F. et al., 2018, A&A, 609, A106
Taddia F. et al., 2019, A&A, 621, A71
Tanaka M., Moriya T. J., Yoshida N., Nomoto K., 2012, MNRAS, 422, 2675
Terreran G., 2020a, Transient Name Server Classification Report, 2618, 1
Terreran G., 2020b, Transient Name Server Classification Report, 2902, 1
Terreran G., 2020c, Transient Name Server Classification Report, 3507, 1
Terreran G., Blanchard P. K., Berton M., Paterson K., Kilpatrick C. D., Coppejans D. L., 2020a, Astron. Telegram, 14027, 1
Terreran G. et al., 2020b, Astron. Telegram, 13970, 1
Terwel J. et al., 2021, Transient Name Server AstroNote, 51, 1
Thornton I., Villar V. A., Gomez S., Hosseinzadeh G., 2024, villrv/extrabol: RNAAS Release, v1.0.1. Zenodo, available at: https://zenodo.org/records/10652250
Thornton I., Villar V. A., Gomez S., Hosseinzadeh G., 2024, Res. Notes Am. Astron. Soc., 8, 48
Tinyanont S., Dimitriadis G., Foley R. J., 2020, Astron. Telegram, 14180, 1
Tinyanont S. et al., 2023, ApJ, 951, 34
Tonry J. L. et al., 2018, PASP, 130, 064505
van der Walt S., Colbert S. C., Varoquaux G., 2011, Comput. Sci. Eng., 13, 22
Villar V. A., Nicholl M., Berger E., 2018, ApJ, 869, 166
Villar V. A. et al., 2020, ApJ, 905, 94
Vinko J., Wheeler J. C., Chatzopoulos E., Marion G. H., Caldwell J., 2010a, Central Bureau Electronic Telegram, 2476, 1
Vinko J. et al., 2010b, Central Bureau Electronic Telegram, 2556, 1
Vreeswijk P. M. et al., 2014, ApJ, 797, 24
Vreeswijk P. M. et al., 2017, ApJ, 835, 58
Wang S. Q., Wang L. J., Dai Z. G., Wu X. F., 2015, ApJ, 799, 107
Wang S. Q., Liu L. D., Dai Z. G., Wang L. J., Wu X. F., 2016, ApJ, 828, 87
Weil K. E., Milisavljevic D., 2020, Transient Name Server Classification Report, 3413, 1
Weil K. E., Milisavljevic D., 2021, Transient Name Server Classification Report, 2881, 1
Weil K. E., Subrayan B. M., Milisavljevic D., 2021a, Transient Name Server Classification Report, 2270, 1
Weil K. E. et al., 2021b, Transient Name Server AstroNote, 182, 1
Weil K. E. et al., 2021c, Transient Name Server AstroNote, 222, 1
West S. L. et al., 2023, A&A, 670, A7
Whitesides L. et al., 2017, ApJ, 851, 107
Woosley S. E., 2010, ApJ, 719, L204
Woosley S. E., 2017, ApJ, 836, 244
Woosley S. E., Weaver T. A., 1986, ARA&A, 24, 205
Woosley S. E., Langer N., Weaver T. A., 1995, ApJ, 448, 315
Woosley S. E., Blinnikov S., Heger A., 2007, Nature, 450, 390
Wright D. et al., 2012, Astron. Telegram, 4313, 1
Wyrzykowski Ł., 2016, in Różańska A., Bejger M., eds, 37th Meeting of the Polish Astronomical Society, Vol. 3. p. 65
Wyrzykowski Ł. et al., 2014, Acta Astron., 64, 197
Wyrzykowski Ł. et al., 2015a, Astron. Telegram, 8486, 1
Wyrzykowski L. et al., 2015b, Astron. Telegram, 8485, 1
Xiang D., Rui L., Wang X., Song H., Xiao F., Zhang T., Zhang J., 2017, Transient Name Server Classification Report, 2017-599, 1
Yan L., 2020, Transient Name Server Classification Report, 2262, 1
Yan L., ZTF SLSN group, 2022, Transient Name Server Classification Report, 45, 1
Yan L. et al., 2015, ApJ, 814, 108
Yan L. et al., 2017a, ApJ, 840, 57
Yan L. et al., 2017b, ApJ, 848, 6
Yan L., Chen Z., Perley D., Schulze S., Taggart K., Gal-Yam A., 2019a, Transient Name Server Classification Report, 2041, 1
Yan L., Perley D., Lunnan R., Schulze S., Gal-Yam A., Taggart K., Yaron O., Velzen S. V., 2019b, Transient Name Server AstroNote, 45, 1
Yan L., Lunnan R., Perley D., Schulze S., Chen T. W., 2020a, Transient Name Server Classification Report, 3639, 1
Yan L., Perley D., Schulze S., Cook D., Chen T. W., Gal-Yam A., Lunnan R., Taggart K., 2020b, Transient Name Server Classification Report, 1736, 1
Yan L. et al., 2020c, ApJ, 902, L8
Yan L., Lunnan R., Perley D., Schulze S., Chen T. W., 2021, Transient Name Server Classification Report, 451, 1
Yan L., De K., Adams S., Anderoni I., ZTF SLSN group, 2022a, Transient Name Server Classification Report, 46, 1
Yan L., Schulze S., ZTF SLSN group, 2022b, Transient Name Server Classification Report, 47, 1
Yan L., Perley, Ho, Yao, Group Z. S., 2023, Transient Name Server Classification Report, 2023-2127, 1
Yao Y., Hammerstein E., Gezari S., Velzen S. V., Somalwar J., Kulkarni S., 2021a, Transient Name Server Classification Report, 2535, 1
Yao Y., Velzen S. V., Tzanidakis A., Gezari S., Hammerstein E., Somalwar J., Kulkarni S., 2021b, Transient Name Server Classification Report, 1614, 1
Yaron O., Gal-Yam A., 2012, PASP, 124, 668
Yin Y., Gomez S., Berger E., Hosseinzadeh G., Nicholl M., Blanchard P. K., 2022, ApJ, 931, 32
Yoshida T., Okita S., Umeda H., 2014, MNRAS, 438, 3119
Young D., 2016, Transient Name Server Classification Report, 68, 1
Young D. R. et al., 2010, A&A, 512, A70
Yu Y.-W., Zhu J.-P., Li S.-Z., Lü H.-J., Zou Y.-C., 2017, ApJ, 840, 12
Zheng W., Patra K., Brink T., Filippenko A. V., 2019, Transient Name Server Classification Report, 1331, 1
Zhu J.-P., Liu L.-D., Yu Y.-W., Mandel I., Hirai R., Zhang B., Chen A., 2024, ApJ, 970, L42
Zieliński P., Wyrzykowski Ł., Rybicki K., Kołaczkowski Z., Bruś P., Mikołajczyk P., 2019, Contrib. Astron. Obs. Skalnate Pleso, 49, 125

APPENDIX A: 'GOLD' SUPERLUMINOUS SUPERNOVAE

The title of each subsection shows the shorthand name adopted for each SN; other given names of each SN are listed in the each section. We specify the individual sources of photometry used for each source.

A1 2005ap

SN 2005ap was was discovered by Robotic Optical Transient Search Experiment (ROTSE) and classified by Quimby et al. (2005) as a possible early Type-II SN, but Quimby et al. (2011c) later rectified the classification of SN 2005ap as an SLSN-I, given the SLSN-I class was unknown at the time of the original classification. We include photometry from Quimby et al. (2007) and from the Caltech Core Collapse Project (Gal-Yam et al. 2007; Arcavi et al. 2012). We include one spectrum from Quimby et al. (2007), obtained from

WISeREP. We note the spectrum taken on 2005 March 16 was provided to WISeREP in terms of rest wavelength, we transform this spectrum back to observed wavelength using a redshift of $z = 0.2832$.

A2 2007bi

SN 2007bi (= SNF20070406−008) was classified as a luminous SN Ic by Nugent (2007) and suggested to be a PISN by Gal-Yam et al. (2009), but later reclassified as an SLSN-R in Gal-Yam (2012) and as an SLSN-I in Nicholl et al. (2013). We include photometry from Gal-Yam et al. (2009) and Young et al. (2010). The Gal-Yam et al. (2009) photometry listed as R band is a combination of photometry from the P60, P200, and P48 telescopes, synthetic Keck photometry taken from spectra, and Catalina Sky Survey (CSS) photometry calibrated to R band. Dessart et al. (2012) argue that SN 2007bi is well reproduced by a model of delayed injection of energy by a magnetar. Yoshida, Okita & Umeda (2014) claim the light curve is well reproduced by the aspherical explosion of a $> 100\,M_\odot$ star. Moriya, Mazzali & Tanaka (2019) argue that 3 $M_\odot$ of CSM are likely to exist around the environment of SN 2007bi. We include one spectrum from Gal-Yam et al. (2009), obtained from WISeREP.

A3 2009jh

SN 2009jh (=CSS090802:144910+292510 = PTF09cwl) was discovered by the Palomar Transient Factory (PTF) and originally classified as an SN Ic, before the SLSN-I designation existed (Drake et al. 2009b; Quimby 2009). The SN was later classified as an SLSN-I by Quimby et al. (2011c). Perley et al. (2016) found an associated host galaxy at a redshift of $z = 0.3499$, which we adopt as the redshift of the SN. We include photometry from De Cia et al. (2018), which the authors correct for extinction using $E(B-V) = 0.013$. We also include photometry from Quimby et al. (2011c), which we correct for extinction. We include one spectrum from Quimby et al. (2018), obtained from WISeREP.

A4 2010gx

SN 2010gx (=CSS100313:112547−084941 = PS1-1000037 = PTF10cwr) was originally discovered by CRTS Mahabal et al. (2010) with an erratum in Mahabal & Drake (2010) and classified as an SLSN-I by Quimby et al. (2010a). A detailed study of the SN was presented in Pastorello et al. (2010), who classify this as a Type-Ic SNe. The detailed study from Quimby et al. (2018) later reclassified the source as a SLSN-I. Perley et al. (2016) found an associated host galaxy at a redshift of $z = 0.2297$, which we adopt as the redshift of the SN. We include photometry from De Cia et al. (2018), which the authors correct for extinction using $E(B-V) = 0.032$. We include photometry from Quimby et al. (2011c) and Pastorello et al. (2010), which we correct for extinction. We note that the early-time r-band photometry from Quimby et al. (2011c) appears ~ 0.2 mag dimmer than the photometry from Pastorello et al. (2010) and De Cia et al. (2018). We include an additional upper limit from Quimby et al. (2010a). There is UVOT photometry from the SOUSA archive, but not in a refereed publication and given that it does not match the u-band photometry from Pastorello et al. (2010), we do not include The Ultra-violet Optical Telescope (UVOT) photometry. We include one spectrum from Pastorello et al. (2010), obtained from WISeREP. Chen et al. (2013) found the host galaxy of SN 2010gx to be a dwarf galaxy with remarkably low metallicity, only 0.06 solar abundance, based on the T_e method.

A5 2010hy

SN 2010hy (PTF10vwg) was discovered by PTF and originally classified as a luminous SN by Kodros et al. (2010) and later as a luminous Type Ic SN by Vinko et al. (2010a). The SN was ultimately classified as an SLSN-I in a detailed study by Quimby et al. (2018). Perley et al. (2016) found an associated host galaxy at a redshift of $z = 0.1901$, which we adopt as the redshift of the SN. We include photometry from De Cia et al. (2018), which the authors correct for extinction using $E(B-V) = 0.455$. We include one spectrum from Shivvers et al. (2019), obtained from WISeREP.

A6 2010kd

SN 2010kd was classified as an early Type-II supernova by Vinko et al. (2010b), but later reclassified as an SLSN-I by Roy (2012). We include photometry from Roy (2012, chap. 6) and Kumar et al. (2020). The authors find a high intrinsic extinction value of $E(B-V) = 0.15$, in addition to a foreground $E(B-V) = 0.02$ extinction. We include one spectrum from Kumar et al. (2020), obtained from WISeREP.

A7 2010md

SN 2010md (=PTF10hgi = PSO J249.4461+06.2081) was discovered by PTF and originally classified as an SLSN-I by Quimby et al. (2013a) with a detailed study presented in Inserra et al. (2013). Perley et al. (2016) found an associated host galaxy at a redshift of $z = 0.0987$, which we adopt as the redshift of the SN. We include photometry from De Cia et al. (2018), which the authors correct for extinction using $E(B-V) = 0.071$. We include photometry from Inserra et al. (2013), which we correct for extinction. Inserra et al. (2013) transform the UVOT U band to Sloan Digital Sky Survey (SDSS) u band. There is UVOT photometry from Quimby et al. (2010b), but this is off by several magnitudes, possibly since these do not account for the host contribution; we therefore do not include it. This is one of the few SLSN-I that shows helium in its photospheric phase (Yan et al. 2020c). We include one spectrum from Quimby et al. (2018), obtained from WISeREP.

A8 2011ke

SN 2011ke (=CSS110406:135058+261642 = PS1-11xk = PTF11dij) was originally discovered by PS1 and classified as an SLSN-I (Drake et al. 2011; Quimby, Sternberg & Matheson 2011b; Smartt et al. 2011). A detailed study of the SN was presented in Inserra et al. (2013). Perley et al. (2016) found an associated host galaxy at a redshift of $z = 0.1428$, which we adopt as the redshift of the SN. We include photometry from De Cia et al. (2018), which the authors correct for extinction using $E(B-V) = 0.01$. We include photometry from Inserra et al. (2013), which we correct for extinction. Inserra et al. (2013) transform the UVOT U band to SDSS u band. We include one spectrum from Inserra et al. (2013), obtained from WISeREP.

A9 2011kg

SN 2011kg (= PTF11rks) was discovered by PTF and originally classified as an SLSN-I by Quimby et al. (2013b) with a detailed study presented in Inserra et al. (2013). Perley et al. (2016) found an associated host galaxy at a redshift of $z = 0.1924$, which we adopt as the redshift of the SN. We include photometry from De Cia et al.

(2018), which the authors correct for extinction using $E(B - V) = 0.035$; and photometry from Inserra et al. (2013), which we correct for extinction. Inserra et al. (2013) transform the UVOT U band to SDSS u band. We do not include the late-time non-detections from Inserra et al. (2013) given the multiple nearby detections from De Cia et al. (2018). Inserra et al. (2013) include two data points from Quimby et al. (2011a), for which we assume an uncertainty of 0.1 mag. We include one spectrum from Quimby et al. (2018), obtained from WISeREP.

A10 2012il

SN 2012il (=CSS120121:094613+195028 = PS1-12fo) was originally discovered by Drake et al. (2012) and classified as an SLSN-I by Smartt et al. (2012). A detailed study of the SN was presented in Inserra et al. (2013), from which we obtain the photometry. The photometry does not have the host flux subtracted, but we conclude its contribution should be negligible given the SN is in the outskirts of a dim galaxy with $r = 21.46$ mag. The host galaxy of SN 2012il was modelled by Chen et al. (2017a). We include one spectrum from Inserra et al. (2013), obtained from WISeREP.

A11 2013dg

SN 2013dg (=CSS130530: 131841 − 070443 = MLS130517: 131841 − 070443) was discovered by the CRTS and classified as an SLSN-I (Drake et al. 2013; Smartt et al. 2013). A detailed study of the SN was presented in Nicholl et al. (2014). We include photometry from Nicholl et al. (2014). We include one spectrum from Shivvers et al. (2019), obtained from WISeREP.

A12 2015bn

SN 2015bn (=PS15ae = CSS141223: 113342 + 004332 = MLS150211: 113342 + 004333) was discovered by ASAS-SN and originally classified as an SLSN-I by Le Guillou et al. (2015) and Guillou (2016). A detailed study of the SN was presented in Nicholl et al. (2016a). We include photometry from Nicholl et al. (2016b, a, 2018b). Leloudas et al. (2017) and Inserra et al. (2018b) presented polarimetry of SN 2015bn and find an increased level of polarization after ∼ 20 d, which the authors interpret as a phase transition where the original outer layer of C and O becomes a more aspherical inner cored dominated by nucleosynthesized material. Bhirombhakdi et al. (2018) present X-ray observations of SN 2015bn and conclude that leakage of energy at late times is required to reproduce the X-ray upper limits. We do not include the late-time WISE photometry from Sun et al. (2022). We include one spectrum from Nicholl et al. (2016a), obtained from WISeREP.

A13 2016ard

SN 2016ard (=PS16aqv = CSS160216: 141045 - 100935) was classified as a SLSN-I by Blanchard et al. (2018c). We include photometry from Blanchard et al. (2018c). We include one spectrum from Blanchard et al. (2018c), obtained from WISeREP.

A14 2016eay

SN 2016eay (= Gaia16apd) was discovered by *WISE* and originally classified as an SLSN-I by Elias-rosa (2016) with a detailed study presented in Nicholl et al. (2017b). The authors transform the *GaiaG* band to SDSS i band, and convert ubv bands to UBV, respectively. We include our own PSF photometry of Las Cumbres GSP images after doing difference imaging to subtract the host contribution. We do not include the late-time *WISE* photometry from Sun et al. (2022). We include one spectrum from Yan et al. (2017a), obtained from WISeREP.

A15 2016inl

SN 2016inl (= PS16fgt) was discovered by PS1 and classified as an SLSN-I by Blanchard et al. (2021c, b). We include photometry from Blanchard et al. (2021c). We include one spectrum from Blanchard et al. (2021c).

A16 2017dwh

SN 2017dwh (=PS17dbf =ATLAS17fau = CSS170425:143443+312917) was discovered by the CRTS and classified as an SLSN-I by Blanchard et al. (2019) and Blanchard, Nicholl & Berger (2018b). We include photometry from Blanchard et al. (2019). We include one spectrum from Blanchard et al. (2019).

A17 2017egm

SN 2017egm (=Gaia17biu =PS18cn = iPTF17egm) was discovered by *Gaia* and originally classified as a Type II SN by Xiang et al. (2017), but later reclassified as an SLSN-I by Dong (2017). A detailed study of the SN was presented in Nicholl et al. (2017a). Izzo et al. (2018) studied the host galaxy of SN 2017egm and report a redshift of $z = 0.03072$, which we adopt as the redshift of the SN. We include photometry from Nicholl et al. (2017a), but exclude data before MJD = 57910 from the MOSFIT model (the equivalent of Model 3 from Nicholl et al. 2017a). Lin et al. (2023) interpreted the multiple peaks in the light curve as being due to collisions from with PPISN Shells. Li et al. (2024) presented GeV emission of the SN from *Fermi*-LAT. We exclude the GSA, ATLAS, and PS1 photometry after MJD = 58105 from the MOSFIT fit, since these show a peculiar late-time rebrightening. Saito et al. (2020) find strong polarization at late times for SN 2017egm. We do not include the late-time *WISE* photometry from Sun et al. (2022). We include one spectrum from Bose et al. (2018), obtained from WISeREP.

A18 2017ens

SN 2017ens (=ATLAS17gqa = CSS170614:120409−015552) was discovered by ATLAS and classified as an SLSN-I by Chen et al. (2018). We include photometry from Chen et al. (2018). The authors show that this SN developed hydrogen features at late times. We do not include the late-time *WISE* photometry from Sun et al. (2022). We include one spectrum taken by C. R. Angus obtained from WIseREP.

A19 2017gci

SN 2017gci (= Gaia17cbp) was discovered by *Gaia* and classified as an SLSN-I by Lyman et al. (2017a), with a following detailed study in Fiore et al. (2021). We include photometry from Fiore et al. (2021), which the authors correct for extinction using $A_V = 0.36$. The authors also transform the GSA magnitudes to g band. Stevance & Eldridge (2021) find that SN 2017gci is well explained by a $30\,M_\odot$ binary system progenitor, as opposed to a single star progenitor. We do not include the late-time *WISE* photometry from Sun et al. (2022). We include one spectrum form Lyman et al. (2017b), obtained from the TNS. We recently presented *JWST* observations of SN 2017gci in Gomez et al. (2024), where we constrain the total amount of dust formed by the SN to be < 0.83 $M_{\odot}$.

A20 2018avk

SN 2018avk (=ZTF18aaisyyp = Gaia18ayq = ATLAS18pcj) was discovered by ZTF and originally classified as an SLSN-I by Nicholl et al. (2018a) with a detailed study presented in Lunnan et al. (2020). We include photometry from Lunnan et al. (2020), which the authors correct for extinction using $E(B-V) = 0.012$. We include our own PSF photometry of FLWO and Las Cumbres GSP images after doing difference imaging to subtract the host flux. We include our own Blue Channel spectrum from Nicholl et al. (2018a).

A21 2018bgv

SN 2018bgv (=ZTF18aavrmcg = Gaia18beg = PS18su = ATLAS18pko = MASTER OT J110230.30 + 553555.5) was discovered by ZTF and originally classified as an SLSN-I by Dong et al. (2018) and Dong (2018). A detailed study of the SN was presented in Lunnan et al. (2020). We include photometry from Lunnan et al. (2020), which the authors correct for extinction using $E(B-V) = 0.008$ mag. We include data from ATLAS, *Gaia*, and the CPCS (Zieliński et al. 2019). We include our own PSF photometry of FLWO and Las Cumbres GSP images after doing difference imaging to subtract the host flux. We exclude CPCS photometry after MJD = 58285 due to a prominent bump not observed in the higher quality ZTF data. We do not include the late-time *WISE* photometry from Sun et al. (2022). We include a spectrum from Dong et al. (2018) and Dong (2018).

A22 2018bsz

SN 2018bsz (=ASASSN-18km = ATLAS18pny) was discovered by ATLAS and originally classified as a SN II by Hiramatsu et al. (2018) and Clark et al. (2018), but later reclassified as an SLSN-I by Anderson et al. (2018). We include photometry from ASAS-SN, ATLAS, and Anderson et al. (2018). The authors do not subtract the host flux from the UVOT photometry, but claim its contribution should be negligible. We exclude the long rising plateau before MJD = 58250 from the MOSFIT fit. Maund et al. (2021) provide polarimetry observations of SN 2018bsz and find limits of $\lesssim 1$ per cent $-$ 2 per cent, except for one detection of 2 ± 0.5 per cent at 11.4 d post maximum. Pursiainen et al. (2022) studied the spectra of SN 2018bsz in detail and found it to be consistent with having aspherical CSM. Chen et al. (2021) found evidence for significant dust formation in SN 2018bsz. We do not include the late-time *WISE* photometry from Sun et al. (2022). We include one spectrum form Clark et al. (2018), obtained from the TNS.

A23 2018bym

SN 2018bym (=ZTF18aapgrxo = PS18aye = ATLAS18ohj = MLS180520: 184313 + 451228) was discovered by ZTF and originally classified as an SLSN-I in Fremling & Sharma (2018) with a detailed study presented in Lunnan et al. (2020). A spectrum from Blanchard et al. (2018a) shows a redshift of $z = 0.274$ based on host emission lines. We include the photometry from Lunnan et al. (2020), which the authors correct for extinction using $E(B-V) = 0.052$, plus Liverpool Telescope (LT) photometry from Chen et al. (2023a), PS1 and ATLAS photometry. We include our own PSF photometry of FLWO and Las Cumbres GSP images after doing difference imaging to subtract the host flux. We exclude the data after MJD = 58372 from the MOSFIT fit, since the SN shows a prominent late-time bump, although with a large scatter. We include one spectrum from Fremling & Sharma (2018), obtained from the TNS.

A24 2018cxa

We classified SN 2018cxa (=ZTF18abfylqx = ATLAS18rsl = MLS180611: 222835 + 113706) as an SLSN-I as part of FLEET (Gomez et al. 2021a) and determine a redshift of $z = 0.19$ based on the SN features. We include photometry from ATLAS and our own PSF photometry of FLWO and ZTF images after doing difference imaging to subtract the host flux. We include our own spectrum from LDSS3C.

A25 2018ffj

SN 2018ffj (=ZTF18abslpjy = ATLAS18tec = GRB180810.28 = MASTER OT J023059.78−172027.1) was discovered by ZTF and classified as an SLSN-I by Kostrzewa-rutkowska et al. (2018). We include photometry from Garcia-Zamora et al. (2018) and ATLAS. We include our own PSF photometry of Las Cumbres GSP and ZTF images, but do not subtract the host galaxy flux contribution, since this should be negligible. We include one spectrum from Kostrzewa-rutkowska et al. (2018), obtained from the TNS.

A26 2018ffs

SN 2018ffs (=ZTF18ablwafp = ATLAS18txu) was discovered by ZTF and classified as an SLSN-I by Gromadzki et al. (2018) and Fremling, Dugas & Sharma (2018b), and by ourselves as part of FLEET. We find a redshift of $z = 0.141$ from host emission lines. We include photometry from ATLAS and ZTF. We include our own PSF photometry of FLWO images after doing difference imaging to subtract the host flux. We include one spectrum from Fremling et al. (2018b), obtained from the TNS.

A27 2018gft

SN 2018gft (=ZTF18abshezu = ATLAS18uym) was discovered by ATLAS and classified as an SLSN-I by Fremling et al. (2018c). We include photometry from Chen et al. (2023a) and ATLAS. Additionally, we include our own PSF photometry of Las Cumbres GSP, FLWO, and LDSS3C images. At the redshift of $z = 0.232$ determined by Chen et al. (2023a), the peak magnitude of the SN is $M_r \sim -22.3$, comfortably in the SLSN-I regime. We include one spectrum from Fremling et al. (2018c), obtained from the TNS.

A28 2018hpq

SN 2018hpq (=ZTF18acapyww = Gaia18det = ATLAS18bcmq) was discovered by ZTF and classified as an SN Ic by Fremling et al. (2018e), and then reclassified as an SLSN-I by Dahiwale & Fremling (2020c) and presented in Chen et al. (2023a) sample. We include photometry from ATLAS, GSA, and ZTF, in addition to early-time upper limits from Chen et al. (2023a). We include our own PSF photometry from ZTF images after doing difference imaging to subtract the host flux. We include one spectrum from Chen et al. (2023a).

A29 2018hti

SN 2018hti (=Gaia19amt = PS19q = ATLAS18yff = MLS181110:034054+114637) was discovered by ATLAS and classified as an SLSN-I by Arcavi et al. (2018), a redshift of $z = 0.0612$ was determined by Lin et al. (2020b) from host emission lines. We include photometry from ATLAS, Lin et al. (2020b), Fiore et al. (2022), and Chen et al. (2023a), in addition to our own PSF photometry of FLWO images after doing difference imaging to subtract the host flux. We include the UVOT data from Fiore et al. (2022) as opposed to the one from Lin et al. (2020b), and include our own processed ATLAS data as opposed to the one from Fiore et al. (2022). We do not include the late-time *WISE* photometry from Sun et al. (2022). We include one spectrum from Fiore et al. (2022).

A30 2018ibb

SN 2018ibb (=ZTF18acenqto = Gaia19cvo = PS19crg = ATLAS18unu) was discovered by *Gaia* and classified as an SN Ia by Fremling et al. (2018f), but later reclassified as an SLSN-I by Pursiainen et al. (2018). More recently, Schulze et al. (2024), Nagele, Umeda & Maeda (2024), and Kozyreva et al. (2024) presented an analysis of SN 2018ibb as a PISN. The spectrum has a hint of Hα, which might be from the host galaxy. We include photometry from *Gaia*, PS1, and ATLAS and our own PSF photometry of ZTF, LDSS3C, and Las Cumbres GSP images. We co-add the late-time ZTF images after MJD = 58650 in bins of 5 d to increase the singal-to-noise ratio of those epochs. We include one spectrum from Pursiainen et al. (2018), obtained from the TNS.

A31 2018kyt

SN 2018kyt (=ZTF18acyxnyw = Gaia19afu) was discovered by ZTF and originally classified as an SLSN-I by Fremling et al. (2019b). A detailed study of the SN was presented in Yan et al. (2020c), who classify this as an SLSN-Ib/IIb. The SN shows a small amount of potential hydrogen at late times. We include photometry from ZTF, ATLAS, Chen et al. (2023a), and GSA. We do not subtract the host contribution from the GSA data, as this appears to have a negligible effect on the light curve. We include one spectrum from Fremling et al. (2019b), obtained from the TNS.

A32 2018lfd

SN 2018lfd (=ZTF18acxgqxq = Gaia19afg = ATLAS18bcjv) was discovered by ATLAS and classified as an SLSN-I by Fremling et al. (2019c). At the reported redshift of $z = 0.2686$ in Chen et al. (2023a), the peak magnitude of the SN is $M_r \sim -22.3$, comfortably in the SLSN-I regime. We include photometry from ZTF, GSA, ATLAS, Chen et al. (2023a), and our own PSF photometry of FLWO images after doing difference imaging to subtract the host flux. We include one spectrum from Chen et al. (2023a).

A33 2018lfe

SN 2018lfe (=ZTF18acqyvag = PS18cpp) was discovered by ZTF and classified as an SLSN-I by Gomez (2019) with a detailed study presented in Yin et al. (2022) and Chen et al. (2023a). We include photometry from Yin et al. (2022) and ATLAS. We include one spectrum from Yin et al. (2022).

A34 2019aamp

SN 2019aamp (= ZTF19aantokv) was discovered by ZTF and classified as an SLSN-I by Chen et al. (2023a) and Yan & ZTF SLSN group (2022). We include photometry from Chen et al. (2023a) and ATLAS. We include one spectrum from Chen et al. (2023a).

A35 2019aamq

SN 2019aamq (= ZTF19aayclnm) was discovered by ZTF and classified as an SLSN-I by Chen et al. (2023a). We include photometry from Chen et al. (2023a) and ATLAS. We include one spectrum from Chen et al. (2023a), which shows a peculiar reddening feature, maybe due to extinction.

A36 2019aamt

SN 2019aamt (= ZTF19abzoyeg) was discovered by ZTF and classified as an SLSN-I by Chen et al. (2023a). We include photometry from ATLAS and Chen et al. (2023a), plus our own PSF photometry of ZTF images after subtracting the host contribution. We include one spectrum from Chen et al. (2023a).

A37 2019aamv

SN 2019aamv (= ZTF20aagikvv) was discovered by ZTF and classified as an SLSN-I by Chen et al. (2023a). We include photometry from ATLAS and Chen et al. (2023a), plus our own PSF photometry of ZTF images. We include one spectrum from Chen et al. (2023a).

A38 2019bgu

SN 2019bgu (=ZTF19aaknqmp =PS19cma = ATLAS19dor) was discovered by ATLAS and classified as an SLSN-I by Fremling et al. (2019d). At the reported redshift of $z = 0.148$, the peak magnitude of the SN is $M_r \sim -20.7$, within the range of SLSNe. We include photometry from Chen et al. (2023a), PS1, and ATLAS. We include one spectrum from Chen et al. (2023a).

A39 2019cca

SN 2019cca (= ZTF19aajwogx) was discovered by ZTF and classified as an SLSN-I by Perley et al. (2019b). We include photometry from Chen et al. (2023a, 2019). We include one spectrum form Gal-Yam (2019b), obtained from the TNS.

A40 2019cdt

SN 2019cdt (=ZTF19aanesgt = Gaia19bll = ATLAS19ekt) was discovered by ZTF and classified as an SLSN-I by Fremling et al. (2019e). We include photometry from GSA, Chen et al. (2023a), and ATLAS. The spectrum from Fremling et al. (2019e) shows significant absorption from Fe-group elements. We include one spectrum from Fremling et al. (2019e), obtained from the TNS.

A41 2019cwu

SN 2019cwu (= ZTF19aapaeye) was discovered by ZTF and classified as an SLSN-I by Perley et al. (2019b) and Yan et al. (2019b). We include photometry from ATLAS, LT photometry from Chen et al. (2023a), and our own PSF photometry of ZTF images. The late-time spectra is consistent with either an SLSN-I or an SN Ic, but given the peak absolute magnitude of $M_g = -22$, we adopt an SLSN-I classification. We include one spectrum from Smith (2019), obtained from the TNS.

A42 2019dgr

SN 2019dgr (=ZTF19aamhast =PS19cwg = ATLAS19geq) was discovered by ZTF and classified as an SLSN-I by Chen et al. (2023a). We include photometry from Chen et al. (2023a), ZTF, PS1, and ATLAS, and our own PSF photometry of one late-time ZTF image. We include one spectrum from Chen et al. (2023a).

A43 2019dlr

SN 2019dlr (= ZTF19aaohuwc) was discovered by ZTF and classified as an SLSN-I by Yan et al. (2019b) and Perley et al. (2019c). We include photometry from Chen et al. (2023a), ATLAS, and our own PSF photometry of ZTF images. The late-time spectrum is consistent with an SLSN-I or SNe Ic, but given the peak absolute magnitude of $M_g = -21.7$, we adopt an SLSN-I classification. We include one spectrum from Perley et al. (2019c), obtained from the TNS.

A44 2019enz

SN 2019enz (=Gaia19bty =PS19cys = ATLAS19ine) 2019enz was discovered by ATLAS and classified as an SLSN-I by Short et al. (2019). The authors find a redshift of $z = 0.22$, but we find a redshift of $z = 0.255$ to be a better fit to the spectral features of the SN. We include photometry from *Gaia*, ZTF, and ATLAS. We include one spectrum from Short et al. (2019), obtained from the TNS.

A45 2019eot

SN 2019eot (=ZTF19aarphwc = ATLAS19kes) 2019eot was discovered by ZTF and classified as an SLSN-I by Fremling et al. (2019h). We include photometry from Chen et al. (2023a), ZTF, and ATLAS. We include one spectrum from Fremling et al. (2019h), obtained from the TNS.

A46 2019gfm

SN 2019gfm (=ZTF19aavouyw =PS19ave = ATLAS19may) 2019gfm was discovered by ATLAS and classified as an SLSN-I by Perley et al. (2019b). We adopt the redshift of the SDSS host galaxy of $z = 0.18167$ (Stoughton et al. 2002). We include photometry from Chen et al. (2023a), PS1, ATLAS, and ZTF. We include one spectrum from Chen (2019), obtained from the TNS.

A47 2019gqi

SN 2019gqi (=ZTF19aasdvfr = ATLAS19mas) 2019gqi was discovered by ZTF and classified as an SLSN-I by Yan et al. (2019b) and Perley et al. (2019c). We include photometry from ATLAS, Chen et al. (2023a), and two late-time upper limits from our own PSF photometry of FLWO images after doing difference imaging to subtract the host flux. The spectra is consistent with an SLSN-I or an SN Ic, but given the peak absolute magnitude of $M_r = -21.9$, we adopt an SLSN-I classification. We include one spectrum from Perley et al. (2019c), obtained from the TNS.

A48 2019hno

SN 2019hno (=ZTF19aawsqsc = ATLAS19ndu) 2019hno was discovered by ZTF and classified as an SLSN-I by Yan et al. (2019b) and Perley et al. (2019c). We include photometry from Chen et al. (2023a), ATLAS, and ZTF. We include one spectrum from Perley et al. (2019c), obtained from the TNS.

A49 2019itq

We classified SN 2019itq (=ZTF19abctjtj = PS19bsr) as an SLSN-I as part of FLEET (Gomez et al. 2021d), originally discovered by ZTF. We determine a redshift of $z = 0.481$ based on the host galaxy emission lines. We include photometry from ATLAS and our own PSF photometry of FLWO and ZTF images, without subtracting the negligible host galaxy contribution. We co-add ZTF images in bins of 5 d to increase the S/N during the decline of the SN. For ZTF images after MJD = 59000, we co-add images in bins of 30 d, but do not detect the SN and only report the upper limits.

A50 2019kcy

SN 2019kcy (=ZTF19abaeyqw = PS19dmu = ATLAS19oho) 2019kcy was discovered by ZTF and classified as an SLSN-I by Yan et al. (2019b) and Perley et al. (2019c). We include photometry from Chen et al. (2023a), PS1, ATLAS, and ZTF. We include one spectrum from Perley et al. (2019c), obtained from the TNS.

A51 2019kwq

SN 2019kwq (= ZTF19aalbrph) 2019kwq was discovered by ZTF and classified as an SLSN-I by Yan et al. (2019b) and Perley et al. (2019c). We include photometry from Chen et al. (2023a), ATLAS, and our own PSF photometry of ZTF images. We co-add individual ZTF images taken on the same calendar day to increase the S/N, for images taken after MJD = 58690, we co-add images within 5 d of each other. The late-time spectrum of SN 2019kwq is consistent with an SLSN-I or SNe Ic, but given the peak absolute magnitude of $M_g = -23.1$, we adopt an SLSN-I classification. We include one spectrum from Perley et al. (2019c), obtained from the TNS.

A52 2019kws

SN 2019kws (=ZTF19aamhhiz = ATLAS19gkz) 2019kwq was discovered by ZTF and classified as an SLSN-I by Yan et al. (2019b) and Perley et al. (2019c) with a detailed study presented in Yan et al. (2020c). The SN is one of the few with a helium-rich spectra. We include photometry from Chen et al. (2023a). We include one spectrum from Chen et al. (2023a).

A53 2019kwt

SN 2019kwt (= ZTF19aaqrime) 2019kwq was discovered by ZTF and classified as an SLSN-I by Yan et al. (2019b) and Perley et al. (2019c). We include photometry from Chen et al. (2023a), ATLAS, and our own PSF photometry of FLWO and ZTF images. We co-add the ZTF photometry before MJD = 58620 in bins of 1 d to increase the S/N of the detections during the rise. We include one spectrum from Perley et al. (2019c), obtained from the TNS.

A54 2019kwu

SN 2019kwu (= ZTF19aaruixj) 2019kwq was discovered by ZTF and classified as an SLSN-I by Yan et al. (2019b) and Perley et al. (2019c). We include photometry from Chen et al. (2023a), ATLAS plus our own PSF photometry of ZTF images. The late-time spectrum is consistent with an SLSN-I or SN Ic, but given the peak absolute magnitude of $M_g = -23.0$, we adopt an SLSN-I classification. We include one spectrum from Perley et al. (2019c), obtained from the TNS.

A55 2019lsq

SN 2019lsq (=ZTF19abfvnns =Gaia19dop = ATLAS19prf) 2019kwq was discovered by ZTF and classified as an SLSN-I by Fremling & Dahiwale (2019b). We include photometry from Chen et al. (2023a), ATLAS, and our own PSF photometry of Las Cumbres GSP images after doing difference imaging to subtract the host flux. We include one spectrum from Chen et al. (2023a).

A56 2019neq

SN 2019neq (=ZTF19abpbopt = ATLAS19sph = PS19eov) 2019kwq was discovered by ZTF and classified as an SLSN-I by Perley et al. (2019d) and Fremling & Dahiwale (2019a), with a detailed study presented in Fiore et al. (2024). We adopt the redshift of $z = 0.1059$ determined by Könyves-Tóth et al. (2020). We include photometry from Chen et al. (2023a), ATLAS, and our own PSF photometry of Las Cumbres GSP images after doing difference imaging to subtract the host flux. We include one spectrum from Könyves-Tóth et al. (2020).

A57 2019nhs

SN 2019nhs (=ZTF19abnacvf = ATLAS19typ = PS19eok) 2019kwq was discovered by ZTF and classified as an SLSN-I by Perley et al. (2019a) and Fremling & Dahiwale (2019a). We include photometry from Chen et al. (2023a), PS1, and ATLAS, in addition to a healthy amount of our own PSF photometry of Las Cumbres GSP images. We include one spectrum from Perley et al. (2019a), obtained from the TNS.

A58 2019otl

We classified SN 2019otl (=ZTF19abkfshj =ATLAS19tup = PS19fsp) as an SLSN-I as part of FLEET (Gomez et al. 2021d), originally discovered by ZTF. We determine a redshift of $z = 0.514$ based on the SN features. We include photometry from Chen et al. (2023a), ATLAS, and PS1. We include our own PSF photometry of IMACS and LDSS3C images, without subtracting the negligible host galaxy contribution. We have no early-time spectra of the source, but late-time spectra is consistent with either an SNe Ic or SLSN-I. We include our own LDSS3C spectrum.

A59 2019pud

SN 2019pud (=ZTF19abxgmzr =Gaia19eri = ATLAS19bfto) 2019pud was discovered by ATLAS and classified as an SLSN-I by Fremling, Dahiwale & Dugas (2019a). We include photometry from ZTF, *Gaia*, and ATLAS. The spectra shows some absorption from Fe-group elements and is consistent with either an SN Ic or an SLSN-I. But given the peak magnitude of $M_r = -20.7$, we adopt an SLSN-I classification. We include one spectrum from Fremling et al. (2019a).

A60 2019sgg

SN 2019sgg (= ZTF19abuyuwa) 2019sgg was discovered by ZTF and classified as an SLSN-I by Yan et al. (2019a). At the reported redshift of $z = 0.5726$, the peak magnitude of the SN is $M_r = -22.7$, comfortably in the SLSN-I regime. We include photometry from ATLAS and Chen et al. (2023a), plus our own PSF photometry of FLWO and LDSS3C images. We include one spectrum from Chen et al. (2023a).

A61 2019sgh

SN 2019sgh (= ZTF19abzqmau) 2019sgg was discovered by ZTF and classified as an SLSN-I as part of FLEET (Gomez et al. 2021d). We determine a redshift of $z = 0.344$ based on host galaxy emission lines. We include photometry from ATLAS, PS1, and Chen et al. (2023a). We include our own PSF photometry of FLWO and MMTCam images after doing difference imaging to subtract the host flux. We include our own Binospec spectrum (Gomez et al. 2021d).

A62 2019szu

SN 2019szu (=ZTF19acfwynw = Gaia19fcb = ATLAS19ynd) 2019sgg was discovered by ZTF and classified as an SLSN-I by Nicholl et al. (2019b) and Dahiwale & Fremling (2019). Aamer et al. (2024) presented a detailed study of the SN and conclude a likely PISN interpretation for SN 2019szu. We include photometry from ATLAS, GSA, and Chen et al. (2023a). We do not subtract the host flux from the *Gaia* photometry since this is from a galaxy of magnitude $m_r = 21.9$ and its contribution should not negligible. We include one spectrum from Nicholl et al. (2019b), obtained from the TNS.

A63 2019ujb

We classified SN 2019ujb (=ZTF19ackjrru =Gaia19fne = ATLAS19bach) as an SLSN-I as part of FLEET (Gomez et al. 2021d), originally discovered by ZTF. We include photometry from GSA, Chen et al. (2023a), and ATLAS. We include our own PSF photometry of FLWO images, without subtracting the negligible host galaxy contribution. We include our own Binospec spectrum (Gomez et al. 2021d).

A64 2019xaq

We classified SN 2019xaq (=ZTF19acyjzbe =Gaia19fue = ATLAS19bfnq) as an SLSN-I as part of FLEET (Gomez et al. 2021d), originally discovered by *Gaia*. We determine a redshift of $z = 0.2$ based on the presence of host emission lines. We include photometry from ATLAS, *Gaia*, and ZTF. We include our own PSF photometry of FLWO and MMTCam images, without subtracting the negligible host galaxy contribution. We include our own Binospec spectrum (Gomez et al. 2021d).

A65 2019zbv

We classified SN 2019zbv (=ZTF19adaivcf = ATLAS19bfmr) as an SLSN-I as part of FLEET (Gomez et al. 2021d), originally discovered by ZTF. We adopt the redshift based on host galaxy emission lines of $z = 0.3785$ from Chen et al. (2023a). We include photometry from ATLAS and Chen et al. (2023a). We include our own PSF photometry of FLWO images, without subtracting the negligible host galaxy contribution. We include our own Binospec spectrum (Gomez et al. 2021d).

A66 2019zeu

We classified SN 2019zeu (=ZTF19adajybt =ATLAS19bfmg = PS20dr) as an SLSN-I as part of FLEET (Gomez et al. 2021d), originally discovered by ZTF. We determine a redshift of $z = 0.39$ based on the SN features. We include photometry from ATLAS and PS1. We include our own PSF photometry of FLWO and ZTF images, without subtracting the negligible host galaxy contribution. We include our own Blue Channel spectrum (Gomez et al. 2021d).

A67 2020abjc

We classified SN 2020abjc (=ZTF20acpyldh = PS20mny) as an SLSN-I as part of FLEET (Blanchard et al. 2020a), originally discovered by ZTF. We determine a redshift of $z = 0.219$ based on host emission lines. We include photometry from ATLAS, PS1, and ZTF photometry, in addition to our own PSF photometry of FLWO and Las Cumbres GSP images. We exclude photometry between MJD = 59723 and 59750 from the MOSFIT fit due to an apparent rebrightening of the light curve. We include our own Binospec spectrum (Blanchard et al. 2020a).

A68 2020adkm

We classified SN 2020adkm as an SLSN-I (Blanchard et al. 2021a), originally discovered by ZTF. We include photometry from ATLAS and ZTF, in addition to our PSF photometry of FLWO, Las Cumbres GSP, and Binospec images. We include our own LDSS3C spectrum, which shows a possible P-Cygni profile at the location of Hα (Blanchard et al. 2021a).

A69 2020afag

SN 2020afag (= ZTF20abisijg) was discovered by ZTF and classified as an SLSN-I by Chen et al. (2023a). We include photometry from Chen et al. (2023a). We include one spectrum from Chen et al. (2023a).

A70 2020afah

SN 2020afah (= ZTF20aawkgxa) was discovered by ZTF and classified as an SLSN-I by Chen et al. (2023a). We include photometry from Chen et al. (2023a) and ATLAS. We include one spectrum from Chen et al. (2023a).

A71 2020ank

SN 2020ank (=ZTF20aahbfmf =ATLAS20dzr = PS20eyd) was discovered by ZTF and classified as an SLSN-I by Poidevin et al. (2020a) and Dahiwale & Fremling (2020a), and later presented in Kumar et al. (2021). Polarimetry observations from Lee (2020) find very low polarization, consistent with a very spherical explosion. We include photometry from Chen et al. (2023a), ATLAS, PS1, and Kumar et al. (2021). We include one spectrum from Poidevin et al. (2020b).

A72 2020aup

SN 2020aup (=ZTF20aahrxgw = ATLAS20cvq) was discovered by ZTF and classified as an SLSN-I by Chen et al. (2023a). We include photometry from Chen et al. (2023a) and ATLAS. We include one spectrum from Chen et al. (2023a).

A73 2020auv

SN 2020auv (=ZTF20aaifybu = ATLAS20eaj) was discovered by ZTF and classified as an SLSN-I by Yan et al. (2020b). We include photometry from Chen et al. (2023a) and ATLAS, as well as our own PSF photometry of FLWO images. We include one spectrum from Chen et al. (2023a).

A74 2020dlb

SN 2020dlb (=ZTF20aaoqwpo =PS20air = ATLAS20ism) was discovered by ZTF and classified as an SLSN-I by Chen et al. (2023a). We include photometry from Chen et al. (2023a), PS1, and ATLAS. We include one spectrum from Chen et al. (2023a).

A75 2020exj

SN 2020exj (=ZTF20aattyuz =PS20bxx = ATLAS20irs) was discovered by ATLAS and classified as an SLSN-I by Dahiwale & Fremling (2020d). We include photometry from Chen et al. (2023a), ATLAS, and PS1, in addition to our own PSF photometry of FLWO images. We have no early-time spectra of the source, but late-time spectra are consistent with either an SN Ic or SLSN-I. Given the peak absolute magnitude of $M_r = -20.49$ mag, we adopt an SLSN-I classification. We include one spectrum from Dahiwale & Fremling (2020d), obtained from the TNS.

A76 2020fvm

SN 2020fvm (=ZTF20aadzbcf = PS20eum) was discovered by ZTF and classified as an SLSN-I by Chen et al. (2023a). We include photometry from Chen et al. (2023a), PS1, and ATLAS. We include one spectrum from Chen et al. (2023a).

A77 2020htd

SN 2020htd (=ZTF20aauoudz =PS20ccj = ATLAS20mzx) was discovered by ZTF and classified as an SLSN-I by Chen et al. (2023a). We include photometry from Chen et al. (2023a), PS1, and ATLAS. We exclude photometry after MJD = 59070 from the MOSFIT fit due to a prominent secondary peak in the light curve. We include one spectrum from Chen et al. (2023a).

A78 2020iyj

SN 2020iyj (=ZTF20aavfbqz = ATLAS20mbx) was discovered by ZTF and classified as an SLSN-I by Chen et al. (2023a). We include photometry from Chen et al. (2023a) and ATLAS. We include one spectrum from Chen et al. (2023a).

A79 2020jii

We classified SN 2020jii (=ZTF20aawfxlt =PS20cvb = ATLAS20mmz) as an SLSN-I as part of FLEET (Gomez et al. 2020c), originally discovered by ATLAS. We include photometry from Chen et al. (2023a), PS1, and ATLAS, plus our own PSF photometry of FLWO images. We determine a redshift of $z = 0.396$ based on the SN features. We include our own Binospec spectrum (Gomez et al. 2020c).

A80 2020qef

SN 2020qef (=ZTF20ablkuio =PS20hhb = ATLAS20ulh) was discovered by ATLAS and classified as a SLSN-I by Terreran et al. (2020b) with a TNS classification report (Terreran 2020a). The authors find a spectrum similar to the SLSNe-Ib presented in Yan et al. (2020c). We include photometry from PS1, ATLAS, and Chen et al. (2023a). Instead of the ZTF photometry from Chen et al. (2023a), we include our own reduction of ZTF images with sets of images co-added in bins of 1 d. The light curve shows a peculiar late-time flattening after MJD = 59121. Therefore, we exclude detections after this date from the MOSFIT fit. We include one spectrum from Terreran (2020a), obtained from the TNS.

A81 2020qlb

SN 2020qlb (=ZTF20abobpcb = Gaia20ekn = ATLAS20vmc) was discovered by ZTF and classified as an SLSN-I by Perez-Fournon et al. (2020). We include photometry from GSA, ATLAS, ZTF, and West et al. (2023). We determine a redshift of $z = 0.1585$ from host emission lines. The light curve shows multiple light-curve bumps studied in West et al. (2023), who argue these are the result of interaction of the ejecta with CSM of varying density. We include our own Binospec spectrum.

A82 2020rmv

SN 2020rmv (=ZTF20abpuwxl = PS20nxm = ATLAS20xqi) was discovered by ZTF and classified as an SLSN-I by Terreran et al. (2020a) and Terreran (2020b). We include photometry from Chen et al. (2023a) and ATLAS, and upper limits from our own FLWO PSF photometry. We include one spectrum from Terreran (2020b), obtained from the TNS.

A83 2020tcw

SN 2020tcw (=ZTF20abzumlr = Gaia20ewr = PS20jci = ATLAS20zst) was discovered by ZTF and classified as an SLSN-I by Perley et al. (2020a). We determine a redshift of $z = 0.064$ from host emission lines of our own spectrum with higher resolution than the one presented in Perley et al. (2020a). We include photometry from GSA, ATLAS, and the ASAS-SN Sky Patrol V2.0 (Hart et al. 2023), in addition to our own PSF photometry of ZTF and FLWO images after subtracting the contribution of the host. We subtract a nominal magnitude of $g = 17.6$ from the ASAS-SN photometry to account for the zero-point contribution of the host.

A84 2020uew

SN 2020uew (=Gaia20eme = PS20ldz = ATLAS20bbum) was discovered by ATLAS and classified as an SLSN-I by Jaeger & Huber (2020). We include photometry from GSA, PS1, and ATLAS, in addition to our PSF photometry of Las Cumbres GSP, IMACS, and DECam images after subtracting the host contribution. We include one spectrum form Ihanec et al. (2020b), obtained from the TNS.

A85 2020vpg

SN 2020vpg (=ZTF20acjmsdu = PS20ikn) was discovered by ZTF and classified as an SLSN-I by Terreran (2020c). We include photometry from ATLAS, and PS1, and our own PSF photometry of ZTF images after subtracting the contribution of the host. We include one spectrum from Terreran (2020c), obtained from the TNS.

A86 2020wnt

SN 2020wnt (=ZTF20acjeflr = ATLAS20beko) was discovered by ZTF and identified by Tinyanont, Dimitriadis & Foley (2020) as an SN with a spectrum similar to a super-Chandrasekhar SN Ia, but also similar to an SN Ic or SLSN-I. The authors disfavour the SLSN-I interpretation due to the low luminosity at the time of discovery. Nevertheless, the SN evolved to a peak absolute magnitude of $M_r \sim -20.5$, within the range for SLSNe. The SN was studied in more detail by Gutiérrez et al. (2022), who argue SN 2020wnt is consistent with being powered by radioactive decay and point out the peculiar spectra of SN 2020wnt lacks the distinctive O II lines seen in SLSNe. Tinyanont et al. (2023) explain the pre-maximum peak as being due to interaction with the CSM and explain the rest of the light curve as magnetar-powered. We include photometry from ATLAS and photometry from seven different telescopes from Gutiérrez et al. (2022), in addition to our own PSF photometry of Binospec and FLWO images.

A87 2020xga

SN 2020xga (=ZTF20acilzkh =PS20jxm = ATLAS20beys) was discovered by ZTF and classified as an SLSN-I by Gromadzki et al. (2020). We include photometry from PS1, ATLAS, and ZTF. We include our own PSF photometry from IMACS, Binospec, and DECam. We include one spectrum from Gromadzki et al. (2020), obtained from the TNS.

A88 2020xgd

SN 2020xgd (=ZTF20aceqspy = PS20jxq = ATLAS20beed) was classified as an SLSN-I by Weil & Milisavljevic (2020) and Gomez et al. (2020d). We include photometry from PS1, ATLAS, and LT photometry from Chen et al. (2023a), in addition to own PSF photometry of ZTF images. We also co-add 18 ZTF r-band images between MJD = 59247 and 59253 to recover a late-time detection. We include one spectrum from Weil & Milisavljevic (2020), obtained from the TNS.

A89 2020xkv

SN 2020xkv (=ZTF20abzaacf = ATLAS20bdpf) was discovered by ZTF and classified as an SLSN-I by Chen et al. (2023a). We include photometry from ZTF, ATLAS, and Chen et al. (2023a). We include one spectrum from Chen et al. (2023a).

A90 2020znr

SN 2020znr (=ZTF20acphdcg =Gaia20fkx = PS20lkc = ATLAS20bgae) was discovered by ZTF and classified as an SLSN-I by Ihanec et al. (2020c). We include photometry from PS1, ATLAS, ZTF, and GSA. We include our own PSF photometry from FLWO, LDSS3C, and IMACS images. The light curve has an early-time bump, so we exclude detections before MJD = 59165 from the MOSFIT fit. Poidevin et al. (2022a) provide optical imaging polarimetry of SN 2020znr and find null-polarization detection. A more detailed study of SN 2020znr will be presented in Chen et al. (in preparation). We include our own LDSS3C spectrum.

A91 2020zzb

SN 2020zzb (=ZTF20acjaayt =PS21adu = ATLAS20bfng) was discovered by ZTF and classified as a SLSN-I by Yan et al. (2020a). We obtained a spectrum of the source with LDSS and confirm the classification and redshift from host emission lines. We include photometry from ATLAS and our own PSF photometry of ZTF images after doing image subtraction. We combine late-time ZTF images after MJD = 59250 taken on the same day. Additionally, we combined 16 ZTF r-band images between MJD = 59260 and 59265 to recover a late-time detection. We include our own LDSS3C spectrum.

A92 2021bnw

SN 2021bnw (=ZTF21aagpymw =Gaia21caf =PS21ajy = ATLAS21dpf) was discovered by ZTF and classified as an SLSN-I by Magee et al. (2021) and Terwel et al. (2021). Poidevin et al. (2023) recently presented polarimetry observations of SN 2021bnw and found no evidence for polarization. We include photometry from ZTF, ATLAS, PS1, and GSA. Additionally, we include our own PSF photometry of Las Cumbres GSP, FLWO, IMACS, and LDSS3C images. A more detailed study of SN 2021bnw will be presented in Fiore et al. (in preparation). We include one spectrum from Magee et al. (2021).

A93 2021een

SN 2021een (=ZTF21aakjkec =Gaia21btp = ATLAS21iyb) was discovered by ZTF and classified as a SLSN-I by Dahiwale & Fremling (2021). We include photometry from ATLAS, GSA, ZTF, as well as our own PSF photometry of Binospec and LDSS3C images. We exclude images from the CPCS due to the lack of information about their source and poor match to the rest of the photometry. We include one spectrum from Dahiwale & Fremling (2021).

A94 2021ejo

We classified SN 2021ejo (= ZTF21aaherjf) an SLSN-I (Gomez et al. 2021b), originally discovered by ATLAS. We include photometry from ZTF and our own PSF photometry of FLWO images. We include photometry from ZTF and ATLAS. We include our own Binospec spectrum.

A95 2021ek

SN 2021ek (=ZTF21aaarmti =PS21fo = ATLAS21ajr) was discovered by ZTF and classified as an SLSN-I by Gillanders et al. (2021) and Srivastav et al. (2021). We include photometry from ZTF, ATLAS, and PS1. Additionally, we include our own PSF photometry of Las Cumbres GSP, Binospec, and DECam images. We include one spectrum from Gillanders et al. (2021).

A96 2021fpl

SN 2021fpl (=ZTF21aaxwpyv =Gaia21ckf =PS21evf = ATLAS21iao) was discovered by ATLAS and classified by Deckers et al. (2021a, b) as an SLSN-I at a redshift between 0.11 and 0.12. Poidevin et al. (2023) recently presented polarimetry observations of SN 2021fpl and found evidence for polarization. We adopt a redshift of 0.121 based on the SN features. We include photometry from *Gaia*, ATLAS, PS1, and ZTF. Additionally, we include our own PSF photometry from FLWO, LDSS3C, and Las Cumbres GSP. We include our own spectrum from FAST.

A97 2021gtr

We classified SN 2021gtr (=ZTF21aagdezv = ATLAS21jbn) as an SLSN-I (Gomez et al. 2021f), originally discovered by ZTF. We include images from ATLAS, as well as our own PSF photometry from FLWO and ZTF images. We include our own Binospec spectrum (Gomez et al. 2021f).

A98 2021hpc

We classified SN 2021hpc (=ZTF21aaqawpd =PS21cui = ATLAS21lxa) as an SLSN-I (Gomez et al. 2021e), originally discovered by ATLAS. We include photometry from ZTF, ATLAS, as well as our own PSF photometry from FLWO images. We include our own Binospec spectrum (Gomez et al. 2021e).

A99 2021hpx

SN 2021hpx (=ZTF21aappdnv =Gaia21bwa = ATLAS21jis) was discovered by ATLAS and classified as an SLSN-I by Gonzalez et al. (2021). We include photometry from *Gaia*, ZTF, and ATLAS, as well as our own PSF photometry from Las Cumbres GSP, FLWO, and LDSS3C images. We include our own spectrum from Las Cumbres Observatory taken as part of the GSP. We include one spectrum from Gonzalez et al. (2021).

A100 2021kty

SN 2021kty (=PS21eya =ZTF21aavdqgf = ATLAS21nrn) was discovered by ZTF and classified as an SLSN-I by Yao et al. (2021a) after retracting a classification as a tidal disruption event (TDE; Yao et al. 2021b). We include photometry from ZTF, ATLAS, and PS1. Additionally, we include our own PSF photometry of FLWO and LDSS3C images. We include one spectrum from Yao et al. (2021a).

A101 2021mkr

SN 2021mkr (=ZTF21abbqeea =Gaia21dbn =PS21fax = ATLAS21rem) was discovered by ZTF and classified as an SLSN-I by Chu, Dahiwale & Fremling (2021a) and Poidevin et al. (2021). We exclude data between MJD = 59420 and 59500 from the MOSFIT fit due to a very prominent second peak in the light curve. We include photometry from ATLAS, ZTF, and our own PSF photometry from FLWO images. We include one spectrum from Chu et al. (2021a).

A102 2021nxq

SN 2021nxq (=ZTF21abcpsjy =PS21etq = ATLAS21rdl) was discovered by PS2 and classified as an SLSN-I by Weil, Subrayan & Milisavljevic (2021a) and Weil et al. (2021b). We include photometry from ATLAS, ZTF, and our own PSF photometry from FLWO images. We include one spectrum from Weil et al. (2021a).

A103 2021txk

We classified SN 2021txk (= ZTF21abjgzhn) as an SLSN-I and determine a redshift of $z = 0.46$ based on the SN features Gomez et al. (2021g). The SN was originally discovered by ZTF. We include photometry from ATLAS, ZTF, and our own PSF photometry from FLWO. We include our own Binospec spectrum.

A104 2021vuw

We classified SN 2021vuw (=ZTF21abrqria =Gaia21ead = ATLAS21bimf) as an SLSN-I and determine a redshift of $z = 0.2$ based on the SN features (Gomez et al. 2021i). The SN was originally discovered by ZTF. We include photometry from ATLAS, ZTF, and our own PSF photometry from FLWO images. We include our own Binospec spectrum.

A105 2021xfu

We classified SN 2021xfu (=ZTF21absyjff = ATLAS21bhce) as an SLSN-I and determine a redshift of $z = 0.32$ based on the SN features (Gomez et al. 2021h). The SN was originally discovered by ZTF. We include photometry from ATLAS, ZTF, and our own PSF photometry from FLWO images. We co-add images in bins of 5 d after MJD = 59869.0 to increase their S/N. We include our own Binospec spectrum.

A106 2021ynn

We classified SN 2021ynn (=ZTF21acaqcrw =PS21jzd = ATLAS21bjwc) as an SLSN-I. We determine a redshift of $z \approx 0.22$ by cross-matching a spectrum of SN 2021ynn taken at a phase of 42 d with one of the SLSN-I 2016eay at 46 d. The SN was originally discovered by ZTF. At this redshift, the peak absolute magnitude of the transient is $M_r \sim -20.8$ mag. Given this and its strong similarity to SN 2016eay, we adopt a SLSN-I classification. We include photometry from ZTF, PS1, ATLAS, and our own PSF photometry of FLWO and DECam images. We include our own LDSS3C spectrum.

A107 2021yrp

We classified SN 2021yrp (=ZTF21abwzpme = ATLAS21bioa) as an SLSN-I and determine a redshift of $z = 0.3$ based on the SN features (Gomez et al. 2021j). The SN was originally discovered by ZTF. We include photometry from ATLAS, ZTF, and our own PSF photometry from FLWO images. We include our own Binospec spectrum.

A108 2021zcl

SN 2021zcl (=ZTF21accwovq =PS21kev = ATLAS21bjql) was discovered by ZTF and classified as an SLSN-I by Gromadzki, Cartier & Yaron (2021). We include photometry from ZTF, PS1, and ATLAS. We include one spectrum from Gromadzki et al. (2021).

A109 2022ful

SN 2022ful (=ZTF22aadeuwu =Gaia22bon = PS22ger) was discovered by ATLAS and classified as an SN Ia by Chu et al. (2022) then reclassified as an SLSN-I by Sollerman (2022). We include photometry from ZTF, *Gaia*, ATLAS, and PS1. We exclude detections after MJD = from the MOSFIT fit due to a strong late-time flattening. We include one spectrum from Sollerman (2022), obtained from the TNS.

A110 2022le

We classified SN 2022le (=ZTF21acrbbwi = PS22cd) as an SLSN-I and determine a redshift of $z = 0.2491$ based on the host emission lines (Gomez et al. 2022b). The SN was originally discovered by ZTF. We include photometry from ATLAS, ZTF, and our own PSF photometry from FLWO and ZTF images. We include our own Binospec spectrum.

A111 2022ljr

SN 2022ljr (=ZTF22aalzjdc =ATLAS22pxh = PS22ezd) was discovered by PS2 and classified as an SLSN-I by Davis et al. (2022). We include photometry from ZTF, ATLAS, PS1, and upper limits from our own PSF photometry of FLWO images. We include one spectrum from Davis et al. (2022), obtained from the TNS.

A112 2022lxd

SN 2022lxd (=ZTF22aaljlzq = ATLAS22rdp) was discovered by ZTF and classified as an SLSN-I by Angus (2022). We include photometry from ZTF and ATLAS, and upper limits from our own PSF photometry of FLWO images. We include one spectrum from Angus (2022), obtained from the TNS.

A113 2022npq

SN 2022npq (=PS22fqn =ATLAS22vfs = ZTF22aarqrxf) was discovered by PS2 and classified as an SLSN-I by Ayala et al. (2022b, a). We include photometry from ZTF, ATLAS, PS1, and our own PSF photometry of FLWO images. We include one spectrum from Ayala et al. (2022a), obtained from the TNS.

A114 2022pjq

SN 2022pjq (=PS22ggy =ATLAS22xpx = ZTF22aausnwr) was discovered by ZTF and classified as an SLSN-I by Fulton et al. (2022c). We include photometry from PS1, and ATLAS, and our own PSF photometry of ZTF images. We include our own LDSS3C spectrum.

A115 2019aamu

SN 2019aamu (= ZTF19acvxquk) was discovered by ZTF and classified as an SLSN-I by Chen et al. (2023a). We include photometry from Chen et al. (2023a), ATLAS, and our own PSF photometry of ZTF images. We include one spectrum from Chen et al. (2023a).

A116 2019vvc

SN 2019vvc (=ZTF19acucxij =Gaia19fnw = ATLAS19bcfc) was discovered by ZTF and classified as an SLSN-I by Chen et al. (2023a). We note the authors quote ZTF19acucxij as the name of the ZTF source, but this name is not available in any of the ZTF alert brokers. We include photometry from Chen et al. (2023a), and ATLAS. We include one spectrum from Chen et al. (2023a).

A117 2022abdu

SN 2022abdu (= ATLAS22bmme) was discovered by ATLAS and classified as an SLSN-I by Gromadzki et al. (2022). We include photometry from ATLAS. We include one spectrum from Gromadzki et al. (2022), obtained from the TNS.

A118 2022ued

SN 2022ued (=ZTF22abexkqi =ATLAS22bete = PS22knc) was discovered by ATLAS and classified as an SN Ib by Perley et al. (2022b). Nevertheless, we also find good spectral matches to SNe Ic and SLSNe-I, and at the reported redshift of $z = 0.1087$, the peak absolute magnitude is $M_r \sim -20.4$, within the SLSNe-I regime. We include photometry from ZTF and ATLAS. We include one spectrum from Perley et al. (2022b), obtained from the TNS.

A119 2018lzv

SN 2018lzv (= ZTF18aazgrfl) was discovered by ZTF and classified as an SLSN-I by Perley, Yan & ZTF SLSN group (2022a). We include photometry from Chen et al. (2023a). We include one spectrum from Chen et al. (2023a).

A120 2018gbw

SN 2018gbw (= ZTF18acslpji) was discovered by ZTF and classified as an SLSN-I by Chen et al. (2023a). We include photometry from Chen et al. (2023a). We include one spectrum from Chen et al. (2023a).

A121 DES14S2qri

DES14S2qri was discovered by DES and classified as a 'gold' SLSN-I by Angus et al. (2019). We include photometry form Angus et al. (2019). We exclude the first three data points from the MOSFIT fit before MJD = 56982 due to an early-time flattening. We include one spectrum from Angus et al. (2019).

A122 DES14X2byo

DES14X2byo was discovered by DES and classified as a 'gold' SLSN-I by Angus et al. (2019). We include photometry form Angus et al. (2019). We include one spectrum from Angus et al. (2019).

A123 DES14X3taz

DES14X3taz was discovered by DES and classified as a 'gold' SLSN-I by Angus et al. (2019). We include photometry form Angus et al. (2019). We exclude the first data points before MJD = 57035 from the MOSFIT fit since these are from a pre-cooling shock (Smith et al. 2016). We include one spectrum from Angus et al. (2019).

A124 DES15E2mlf

DES15E2mlf was discovered by DES and classified as a 'gold' SLSN-I by Angus et al. (2019). We include photometry form Angus et al. (2019). We exclude the first g-band data point before MJD = 57328 since this is from a precursor of the SN Pan et al. (2017). We include one spectrum from Angus et al. (2019).

A125 DES15X1noe

DES15X1noe was discovered by DES and classified as a 'gold' SLSN-I by Angus et al. (2019). We include photometry form Angus et al. (2019). We exclude the first z-band data point before MJD = 57350, since this is too bright to be consistent with a smooth rise. We include one spectrum from Angus et al. (2019).

A126 DES15X3hm

DES15X3hm was discovered by DES and classified as a 'gold' SLSN-I by Angus et al. (2019). We include photometry form Angus et al. (2019). We include one spectrum from Angus et al. (2019).

A127 DES16C2aix

DES16C2aix was discovered by DES and classified as a 'gold' SLSN-I by Angus et al. (2019). We include photometry form Angus et al. (2019). We include one spectrum from Angus et al. (2019).

A128 DES16C3dmp

DES16C3dmp was discovered by DES and classified as a 'gold' SLSN-I by Angus et al. (2019). We include photometry form Angus et al. (2019). Angus et al. (2019) report a small bump during the rise in the bluer bands, which is why we exclude the data before MJD = 57705 from the MOSFITfit. We include one spectrum from Angus et al. (2019).

A129 DES17X1amf

DES17X1amf was discovered by DES and classified as a 'gold' SLSN-I by Angus et al. (2019). We include photometry form Angus et al. (2019). We exclude the data before MJD = 58018, since these are from an early bump. We include one spectrum from Angus et al. (2019).

A130 DES17X1blv

DES17X1blv was discovered by DES and classified as a 'gold' SLSN-I by Angus et al. (2019). We include photometry form Angus et al. (2019). We exclude the first z-band point before MJD = 58030 since this appears to be from a pre-cooling peak. We include one spectrum from Angus et al. (2019).

A131 iPTF13ajg

iPTF13ajg was discovered by PTF and classified as an SLSN-I by Vreeswijk et al. (2014). We include photometry from Vreeswijk et al. (2014). The light curve shows what could be a flattening or bump in Rs band after MJD = 56600. We include one spectrum from Vreeswijk et al. (2014).

A132 iPTF13ehe

iPTF13ehe was discovered by PTF and classified as an SLSN-I by Yan et al. (2015), who find the supernova shows late-time hydrogen emission. We include photometry from Yan et al. (2015), who do not subtract the host contribution from the photometry. Wang et al. (2016) modelled the SN and argues for a triple power source (Radioactive decay + Magnetar + CSM Interaction). We include one spectrum from Yan et al. (2015).

A133 iPTF15eov

iPTF15eov was discovered by PTF and classified as an SN Ic by Taddia et al. (2019), but noted to be significantly luminous. Gullin (2019) present an analysis of the SN and conclude it is closer to an SLSN-I. The peak absolute magnitude of $M_r \sim -21.2$ is well within the range for SLSN-I. We include photometry from Taddia et al. (2019). We include one spectrum from Taddia et al. (2019).

A134 iPTF16eh

iPTF16eh was classified as an SLSN-I by Lunnan et al. (2018b). We include photometry from Lunnan et al. (2018b). We include one spectrum from Lunnan et al. (2018b).

A135 LSQ12dlf

LSQ12dlf was discovered by Public ESO Spectroscopic Survey of Transient Objects (PESSTO) classified as an SLSN-I by Nicholl et al. (2014). We include photometry from Nicholl et al. (2014). We include one spectrum from Nicholl et al. (2014).

A136 LSQ14bdq

LSQ14bdq was discovered by PESSTO classified as an SLSN-I by Nicholl et al. (2015a). We include photometry from Nicholl et al. (2015a). The supernova has an early-time bump before MJD = 56740, which we exclude from the MOSFIT fit. We include one spectrum from Nicholl et al. (2015a).

A137 LSQ14mo

LSQ14mo was classified as an SLSN-I by Chen et al. (2017b). We include photometry from Chen et al. (2017b) and UVOT photometry from the SOUSA. Polarimetry data of the SN was presented in Leloudas et al. (2015a). Additionally, we include our own PSF photometry of Las Cumbres GSP images after doing difference imaging to subtract the host flux. We include a spectrum from Chen et al. (2017b), obtained from WISeREP.

A138 OGLE15qz

OGLE15qz was discovered by OGLE and classified as an SLSN-I by Kostrzewa-Rutkowska et al. (2015). We include photometry from OGLE, and from Kostrzewa-Rutkowska et al. (2015), the latter already corrected for extinction. We include a spectrum obtained from WISeREP.

A139 PS110awh

PS1-10awh (= PSc090022) was discovered by MDS and classified as an SLSN-I by Chomiuk et al. (2011) and presented in Lunnan et al. (2018c). The authors correct the photometry for extinction. We include photometry from Lunnan et al. (2018c), plus y-band photometry from Chomiuk et al. (2011). The SN was reported as a spectroscopically classified SLSN-I as part of the PS1 MDS (Hosseinzadeh et al. 2020; Villar et al. 2020). We include one spectrum from Chomiuk et al. (2011).

A140 PS110bzj

PS1-10bzj (= PSc110405) was discovered by MDS and classified as an SLSN-I by Lunnan et al. (2013) and presented in Lunnan et al. (2018c). The authors correct the photometry for extinction. The SN was reported as a spectroscopically classified SLSN-I as part of the PS1 MDS (Hosseinzadeh et al. 2020; Villar et al. 2020). We include one spectrum from Lunnan et al. (2013).

A141 PS110ky

PS1-10ky (= PSc060270) was discovered by MDS and classified as an SLSN-I by Chomiuk et al. (2011) and presented in Lunnan et al. (2018c). We include the photometry from Lunnan et al. (2018c), which the authors correct for extinction. The SN was reported as a spectroscopically classified SLSN-I as part of the PS1 MDS (Hosseinzadeh et al. 2020; Villar et al. 2020). We include one spectrum from Chomiuk et al. (2011).

A142 PS110pm

PS1-10pm (= PSc030129) was discovered by MDS and classified as an SLSN-I by McCrum et al. (2015) and presented in Lunnan et al. (2018c). The authors correct the photometry for extinction. We include photometry from Lunnan et al. (2018c), but exclude the late-time William Herschel Telescope (WHT) nd GNemini-Northdata from McCrum et al. (2015), since these do not have the host galaxy host subtracted. The SN was reported as a spectroscopically classified SLSN-I as part of the PS1 MDS (Hosseinzadeh et al. 2020; Villar et al. 2020). We include one spectrum from McCrum et al. (2015).

A143 PS111afv

PS1-11afv (= PSc160103) was discovered by MDS and classified as an SLSN-I by Lunnan et al. (2014) and presented in McCrum et al. (2015) and Lunnan et al. (2018c). We include photometry from Lunnan et al. (2018c), which the authors correct for extinction. The SN was reported as a spectroscopically classified SLSN-I as part of the PS1 MDS (Hosseinzadeh et al. 2020; Villar et al. 2020). We include one spectrum from Lunnan et al. (2018c).

A144 PS111aib

PS1-11aib (= PSc180279) was discovered by MDS and classified as an SLSN-I by Lunnan et al. (2014) and presented in McCrum et al. (2015) and Lunnan et al. (2018c). We include photometry from Lunnan et al. (2018c), which the authors correct for extinction. The light curve shows a possible early-time bump. The SN was reported as a spectroscopically classified SLSN-I as part of the PS1 MDS (Hosseinzadeh et al. 2020; Villar et al. 2020). We include one spectrum from Lunnan et al. (2018c).

A145 PS111ap

PS1-11ap (= PSc120031) was discovered by MDS and classified as an SLSN-I by Lunnan et al. (2018c), reported as a spectroscopically classified SLSN-I as part of the PS1 MDS (Hosseinzadeh et al. 2020; Villar et al. 2020). We include photometry from McCrum et al. (2014) and from Lunnan et al. (2018c). Photometry from Lunnan et al. (2018c) is already corrected for extinction. We include one spectrum from McCrum et al. (2014).

A146 PS111bdn

PS1-11bdn (= PSc340195) was discovered by MDS and classified as an SLSN-I by Lunnan et al. (2014) and presented in Lunnan et al. (2018c). We include photometry from UVOT and from Lunnan et al. (2018c), which the authors correct for extinction. The SN was reported as a spectroscopically classified SLSN-I as part of the PS1 MDS (Hosseinzadeh et al. 2020; Villar et al. 2020). We include one spectrum from Lunnan et al. (2018c).

A147 PS112bqf

PS1-12bqf (= PSc440176) was discovered by MDS and classified as an SLSN-I by Lunnan et al. (2014) and presented in Lunnan et al. (2018c). We include photometry from Lunnan et al. (2018c), which the authors correct for extinction. This is one of the lowest luminosity objects in the Lunnan et al. (2018c) sample. The SN was reported as a spectroscopically classified SLSN-I as part of the PS1 MDS (Hosseinzadeh et al. 2020; Villar et al. 2020). We include one spectrum from Lunnan et al. (2018c).

A148 PS112cil

PS1-12cil (= PSc460103) was discovered by MDS and classified as an SLSN-I by Lunnan et al. (2018c). The authors correct the photometry for extinction. The light curve has a pronounced second peak after MJD = 56333, we therefore exclude these data from the MOSFIT fit. We also exclude the first y-band data point from the MOSFIT fit due to it being unusually bright. The SN was reported as a spectroscopically classified SLSN-I as part of the PS1 MDS (Hosseinzadeh et al. 2020; Villar et al. 2020). We include one spectrum from Lunnan et al. (2018c).

A149 PS113or

PS1-13or (= PSc480552) was discovered by MDS and classified as an SLSN-I by Lunnan et al. (2018c). We include photometry from Lunnan et al. (2018c), which the authors correct for extinction. The SN was reported as a spectroscopically classified SLSN-I as part of the PS1 MDS (Hosseinzadeh et al. 2020; Villar et al. 2020). We include one spectrum from Lunnan et al. (2018c).

A150 PS114bj

PS1-14bj (= PSc590123) was discovered by MDS and classified as an SLSN-I by Lunnan et al. (2016). We include photometry from Lunnan et al. (2018c), which the authors correct for extinction. The redshift in Lunnan et al. (2018c) has a typo quoted as $z = 0.5125$, where it should be $z = 0.5215$. The SN was reported as a spectroscopically classified SLSN-I as part of the PS1 MDS (Hosseinzadeh et al. 2020; Villar et al. 2020).

A151 PS15cjz

PS15cjz (= DES15S2nr) was discovered by DES and classified as a 'gold' SLSN-I by Angus et al. (2019). We include photometry from PS1 and Angus et al. (2019). We exclude the detections before MJD = 57257 from the MOSFIT fit due to a early-time bump. We include one spectrum from Angus et al. (2019).

A152 PTF09atu

PTF09atu was discovered by PTF and classified as an SLSN-I by Perley et al. (2016), the authors find an associated host galaxy at a redshift of $z = 0.5015$. We include photometry from De Cia et al. (2018), as opposed to the original presentation of the data from Quimby et al. (2011c). The photometry from De Cia et al. (2018) is already corrected for extinction using $E(B-V) = 0.042$. We include one spectrum from Quimby et al. (2018).

A153 PTF09cnd

PTF09cnd was discovered by PTF and classified as an SLSN-I by Quimby et al. (2011c) and presented in Perley et al. (2016), who find an associated host galaxy at a redshift of $z = 0.2584$. We include photometry from De Cia et al. (2018), which the authors correct for extinction using $E(B-V) = 0.019$. We include one spectrum from Quimby et al. (2018).

A154 PTF10uhf

PTF10uhf was discovered by PTF and classified as an SLSN-I by Quimby et al. (2018). Perley et al. (2016) found an associated host galaxy at a redshift of $z = 0.2882$. We include photometry from De Cia et al. (2018), which the authors correct for extinction using $E(B-V) = 0.016$. We include one spectrum from Quimby et al. (2018).

A155 PTF10vqv

PTF10vqv was discovered by PTF and classified as an SLSN-I by Quimby et al. (2018). Perley et al. (2016) found an associated host galaxy at a redshift of $z = 0.4518$. We include photometry from De Cia et al. (2018), which the authors correct for extinction using $E(B-V) = 0.055$. We include one spectrum from Quimby et al. (2018).

A156 PTF12dam

PTF12dam was discovered by PTF and classified as an SLSN-I by Nicholl et al. (2013). Perley et al. (2016) found an associated host galaxy at a redshift of $z = 0.1073$. We include photometry from De Cia et al. (2018), which the authors correct for extinction using $E(B-V) = 0.03$. We also include photometry from Nicholl et al. (2013) and Chen et al. (2015), which we correct for extinction. We include one spectrum from Quimby et al. (2018).

A157 PTF12mxx

PTF12mxx was discovered by PTF and classified as an SLSN-I by Quimby et al. (2018). Perley et al. (2016) found an associated host galaxy at a redshift of $z = 0.3296$. We include photometry from De Cia et al. (2018), which the authors correct for extinction using $E(B-V) = 0.039$. We include one spectrum from Quimby et al. (2018).

A158 SCP06F6

SCP06F6 (= J143227.42+333225.1) was discovered by Barbary et al. (2009) and classified as a new class of transient, and subsequently as an SLSN-I by Quimby et al. (2011c). Chatzopoulos, Wheeler & Vinko (2009) model the light curve of SCP06F6 with either a pair-instability model or a CSM interaction model. All photometry is in the Vega magnitude system. We exclude the first z-band data point before MJD = 53750 due to an early-time excess. We include one spectrum from Barbary et al. (2009).

A159 SNLS06D4eu

SNLS 06D4eu was classified as an SLSN-I by Howell et al. (2013). All the photometry is presented in the Vega magnitude system. We exclude the first three detections before MJD = 53950 from the MOSFIT model due to an early-time excess. We include one spectrum from Howell et al. (2013).

A160 SNLS07D2bv

SNLS 07D2bv was classified as an SLSN-I by Howell et al. (2013). All the photometry is presented in the Vega magnitude system. We include one spectrum from Howell et al. (2013).

A161 2018lzx

SN 2018lzx (= ZTF18abszecm) was discovered by ZTF and classified as an SLSN-I by Chen et al. (2023a) and Yan et al. (2022a). We include photometry from Chen et al. (2023a) and ATLAS. We include one spectrum from Chen et al. (2023a).

A162 2019aamr

SN 2019aamr (= ZTF19abdlzyq) was discovered by ZTF and classified as an SLSN-I by Chen et al. (2023a). We include photometry from Chen et al. (2023a), ATLAS, and our own PSF photometry of early-time ZTF images. We include one spectrum from Chen et al. (2023a).

A163 2019aams

SN 2019aams (= ZTF19abnqqdp) was discovered by ZTF and classified as an SLSN-I by Chen et al. (2023a). We include photometry from Chen et al. (2023a) and ATLAS. We include one spectrum from Chen et al. (2023a).

A164 2019aamx

SN 2019aamx (= ZTF19abcvwrz) was discovered by ZTF and classified as an SLSN-I by Chen et al. (2023a). We include photometry from Chen et al. (2023a) and ATLAS. We include one spectrum from Chen et al. (2023a).

A165 2019qgk

SN 2019qgk (= ZTF19abuolvj) was discovered by ZTF and classified as an SLSN-I by Chen et al. (2023a). We include photometry from from Chen et al. (2023a) and ATLAS. We include one spectrum from Chen et al. (2023a).

A166 2019xdy

SN 2019xdy (=ZTF19acsajxn = PS19jja) was discovered by ZTF and classified as an SLSN-I by Chen et al. (2023a). We include photometry from ATLAS, PS1, and upper limits from Chen et al. (2023a), additionally we include our own PSF photometry of ZTF images. Given the high cadence of ZTF observations, we co-add the images in bins of 1 h, or 1 d. We include one spectrum from Chen et al. (2023a).

A167 2020kox

SN 2020kox (=ZTF20aavqrzc = ATLAS20nev) was discovered by ZTF and classified as an SLSN-I by Chen et al. (2023a). We include photometry from Chen et al. (2023a), ATLAS, and our own PSF photometry of late-time ZTF r-band images. We include one spectrum from Chen et al. (2023a).

A168 2020zbf

SN 2020zbf (= ATLAS20bfee) was discovered by ATLAS and classified as an SLSN-I by Ihanec et al. (2020a) and Lunnan & Schulze (2021), with a detailed study in Gkini et al. (2024). We include photometry from ATLAS. We include one spectrum from Ihanec et al. (2020a).

APPENDIX B: 'SILVER' SUPERLUMINOUS SUPERNOVAE

B1 2019unb

We presented SN 2019unb (=ZTF19acgjpgh =Gaia19fbu =PS19isr = ATLAS19bari) as an SLSN-like LSN in Gomez et al. (2022a). The SN was originally was discovered by ZTF and classified by Dahiwale & Fremling (2020b) with a detailed study presented in Yan et al. (2020c), and in Prentice et al. (2019, 2021). We include additional photometry from ATLAS and Chen et al. (2023a). We assign a silver label given that this is an LSN. We include one spectrum from Dahiwale & Fremling (2020b).

B2 2019hge

We presented SN 2019hge (=ZTF19aawfbtg =Gaia19est =ATLAS19och = PS19elv) as an SLSN-like LSN in Gomez et al. (2022a). The SN was discovered by ZTF, classified by Yan et al. (2020c) and presented in Prentice et al. (2021). We include additional photometry from ATLAS and Chen et al. (2023a), but exclude detections after MJD = 58770 from the MOSFIT fit due to a late-time re-brightening of the light curve. We assign a silver label given that this is an LSN. We include one spectrum from Dahiwale, Dugas & Fremling (2019a).

B3 2019gam

We presented SN 2019gam (=ZTF19aauvzyh = ATLAS19lsz) as an SLSN-like LSN in Gomez et al. (2022a). The SN was discovered by ZTF and classified by Yan et al. (2020c). We include additional photometry from ATLAS, and late-time LT and Spectral Energy Distribution Machine (SEDM) photometry from Chen et al. (2023a). We assign a silver label given that this is an LSN. We include one spectrum from Chen et al. (2023a).

B4 PTF12gty

We presented PTF12gty as an SLSN-like LSN in Gomez et al. (2022a). The SN was originally discovered by PTF, classified by Quimby et al. (2018) and Barbarino et al. (2021), and presented in De Cia et al. (2018). We assign a silver label given that this is an LSN. We include one spectrum from Quimby et al. (2018).

B5 2016aj

SN 2016aj (= PS16op) was classified as an SLSN-I by Young (2016). We include PS1 photometry and one epoch of UVOT photometry from the SOUSA archive. We do not correct the UVOT photometry for the contribution of the host, since the host magnitude is below the PS1 detection limit and is therefore likely negligible in the UV. We assign a silver label since the photometry available is very sparse and there are no data during the rise. We include one spectrum from Young (2016).

B6 OGLE15xx

OGLE15xx was discovered by OGLE and classified as an SN Ib/c by Wyrzykowski et al. (2015a), but the spectrum and peak magnitude match those of an SLSN-I. We include OGLE photometry and exclude the first detection before MJD = 57375 due to a pre-explosion bump. We assign a silver label given there is only one band of photometry available. We include a spectrum obtained from WISeREP.

B7 1991D

We presented 1991D as an SN with spectra consistent with either a Type Ib SN or an SLSN in Gomez et al. (2022a). The SN was originally classified by Benetti et al. (2002) and presented in Matheson et al. (2001). We assign a silver label given that this is an LSN. We include one spectrum from Matheson et al. (2001).

B8 2006oz

SN 2006oz (= SDSS-II SN 15557) was classified by Leloudas et al. (2012) as an SLSN-I. We include photometry from Leloudas et al. (2012). We exclude photometry before MJD = 54036 from the MOSFIT fit since these appear to be from an initial bump. Leloudas et al. (2012) pointed out this bump could be powered by a recombination wave in the circumstellar medium. Alternatively, Ouyed & Leahy (2013) explain the bump as part of a dual-shock quark nova. We assign a silver label given the lack of photometry after peak. We include one spectrum from Leloudas et al. (2012), obtained from WISeREP.

B9 2009cb

We presented SN 2009cb (=CSS090319:125916+271641 = PTF09as) as an LSN in Gomez et al. (2022a). The SN was originally discovered by PTF, classified by Quimby et al. (2018), and presented in De Cia et al. (2018). We assign a silver label given that this is an LSN. We include one spectrum from Quimby et al. (2018).

B10 2011kl

We presented SN 2011kl (= GRB111209A) as an SLSN-like LSN in Gomez et al. (2022a). The SN was originally classified by Greiner et al. (2015), Mazzali et al. (2016), and Kann et al. (2019). We assign a silver label given that this is an LSN. We include one spectrum from Greiner et al. (2015).

B11 2012aa

We presented SN 2012aa (=PSN J14523348−0331540 = Howerton-A20) as an SN with spectra consistent with either a Type Ibc SN or an SLSN in Gomez et al. (2022a). The SN was originally discovered by CRTS, classified by Roy et al. (2016), and studied in Yan et al. (2017b) and Shivvers et al. (2019). We assign a silver label given that this is an LSN. We include one spectrum from Shivvers et al. (2019).

B12 2013hy

We presented SN 2013hy (= DES13S2cmm) as an SLSN-like LSN in Gomez et al. (2022a). The SN was originally discovered by DES and classified by Papadopoulos et al. (2015) and Angus et al. (2019). We assign a silver label given that this is an LSN. We include one spectrum from Angus et al. (2019).

B13 2018beh

We presented SN 2018beh (=ZTF18aahpbwz =ASASSN-18ji =PS18ats = ATLAS18nvb) as an SLSN-like LSN in Gomez et al. (2022a). Here, we include additional photometry from ATLAS. The SN was originally classified by Mcbrien et al. (2018) and Dahiwale & Fremling (2020c). We assign a silver label given that this is an LSN. We include one spectrum from Mcbrien et al. (2018).

B14 2018don

We presented SN 2018don (=ZTF18aajqcue =PS18aqo = ATLAS18nxb) as an SLSN-like LSN in Gomez et al. (2022a). The SN was originally discovered by ZTF, classified by Lunnan et al. (2020), and presented in Fremling, Sharma & Dahiwale (2019i). We include additional photometry from ATLAS, and late-time LT images from Chen et al. (2023a). We assign a silver label given that this is an LSN. We include one spectrum from Fremling et al. (2019i).

B15 2019J

We presented SN 2019J (=ZTF19aacxrab =PS18crs = ATLAS19cay) as an SLSN-like LSN in Gomez et al. (2022a). The SN was originally classified by Fremling et al. (2019f). We adopt a redshift of $z = 0.1346$ determined by Chen et al. (2023a). We include additional photometry from Chen et al. (2023a). We assign a silver label given that this is an LSN. We include one spectrum from Chen et al. (2023a).

B16 2019dwa

We presented SN 2019dwa (=ZTF19aarfyvc = Gaia19bxj) as an SN with spectra consistent with either a Type Ic SN or an SLSN in Gomez et al. (2022a). The SN was originally discovered by ZTF, classified by Fremling et al. (2019g), and presented in Prentice et al. (2021). We include additional photometry from ATLAS. We assign a silver label given that this is an LSN. We include one spectrum from Fremling et al. (2019g).

B17 2019ieh

SN 2019ieh (=ZTF19abauylg =Gaia19cxd =PS19bil = ATLAS19nsv) was discovered by ZTF and classified as an SN Ic-BL by Zheng et al. (2019) and as an SN Ic by Dahiwale, Fremling & Sharma (2019b). We adopt the redshift from Zheng et al. (2019), derived from host emission lines. At this redshift, the SN peaks at a magnitude of $M_r \sim -19.3$, which makes this an LSN. We include photometry from ZTF, ATLAS, GSA, and PS1.

We include one spectrum from Zheng et al. (2019), obtained from the TNS. We assign a silver label given that this is an LSN.

B18 2019obk

We presented SN 2019obk (=ZTF19abrbsvm =PS19eqz = ATLAS19tvm) as an SLSN-like LSN in Gomez et al. (2022a). The SN was originally discovered by ZTF and classified by Yan et al. (2020c). We include additional photometry from ATLAS and Chen et al. (2023a). We assign a silver label given that this is an LSN. We include one spectrum from Chen et al. (2023a).

B19 2019pvs

We presented and classified SN 2019pvs (=ZTF19abuogff = PS19fbe) as an SLSN-like LSN in Gomez et al. (2022a). The SN was originally discovered by ZTF and classified in Gomez et al. (2021d). We include additional photometry from ATLAS. We assign a silver label given that this is an LSN. We include one spectrum from Gomez et al. (2022a).

B20 2021lwz

We presented SN 2021lwz as an SLSN-like LSN in Gomez et al. (2022a). The SN was originally discovered by ATLAS and classified by Perley et al. (2021). We include additional photometry from ATLAS. We assign a silver label given that this is an LSN. We include one spectrum from Perley et al. (2021).

B21 DES14C1rhg

We presented DES14C1rhg as an SLSN-like LSN in Gomez et al. (2022a). The SN was originally discovered by DES and classified by Angus et al. (2019). We assign a silver label given that this is an LSN. We include photometry and one spectrum from Angus et al. (2019).

B22 DES15C3hav

We presented DES15C3hav as an SLSN-like LSN in Gomez et al. (2022a). The SN was originally discovered by DES and classified in Angus et al. (2019). We assign a silver label given that this is an LSN. We include photometry and one spectrum from Angus et al. (2019).

B23 OGLE15xl

We presented OGLE15xl as an SLSN-like LSN in Gomez et al. (2022a). The SN was originally discovered by OGLE and classified by Le Breton et al. (2015). We assign a silver label given that this is an LSN. We include one spectrum from Le Breton et al. (2015).

B24 PTF10iam

We presented PTF10iam as an SLSN-like LSN in Gomez et al. (2022a). The SN was originally classified by Arcavi et al. (2016). We assign a silver label given that this is an LSN. We include one spectrum from Arcavi et al. (2016).

B25 PTF12hni

We presented PTF12hni as an SN with spectra consistent with either a Type Ic SN or an SLSN in Gomez et al. (2022a). The SN was originally discovered by PTF and classified by Quimby et al. (2018) and presented in De Cia et al. (2018). We assign a silver label given that this is an LSN. We include one spectrum from Quimby et al. (2018).

B26 PTF10bjp

PTF10bjp was discovered by PTF and classified as an SLSN-I by Quimby et al. (2018). Perley et al. (2016) found an associated host galaxy at a redshift of $z = 0.3584$. We include photometry from De Cia et al. (2018), which the authors correct for extinction using $E(B-V) = 0.055$. We assign a silver label given there is only one band of photometry available. We include one spectrum from Quimby et al. (2018).

B27 2017jan

SN 2017jan (= OGLE17jan) was discovered by OGLE and classified as an SLSN-I by Angus et al. (2017). We include photometry from OGLE (Wyrzykowski et al. 2014) between MJD = 58005 and 58200, excluding noisy late-time photometry and an apparent early-time bump. We assign a silver label given there is only one band of photometry available. We include one spectrum from Angus et al. (2017), obtained from the TNS.

B28 OGLE16dmu

OGLE16dmu was discovered by OGLE and classified as an SLSN-I by Prentice et al. (2016) and presented in Cikota et al. (2018). We assign a silver label given there is only one band of photometry available. We include photometry from OGLE. We include a spectrum from Cikota et al. (2018).

B29 OGLE15sd

OGLE15sd was discovered by OGLE and classified as an SLSN-I by Wyrzykowski et al. (2015b). We include photometry from OGLE. We assign a silver label given that there is only one band of photometry available. We include a spectrum obtained from WISeREP.

B30 SSS120810

SSS120810:231802−560926 was originally discovered by Wright et al. (2012) and classified as an SLSN-I by Inserra et al. (2012). A detailed study of the SN was presented in Nicholl et al. (2014) and a study of its host galaxy in Leloudas et al. (2015b). We include photometry from Nicholl et al. (2014). We assign a silver label given the lack of photometry before peak.

B31 2020myh

We classified SN 2020myh (=ZTF20abgbxby = ATLAS20pxs), originally discovered by ATLAS, as a SLSN-I as part of FLEET (Gomez et al. 2020c). We determine a redshift of $z = 0.283$ based on host emission lines. We include photometry from ATLAS and ZTF. We have no early-time spectra of the source, but one low S/N late-time spectrum consistent with either an SNe Ic or an SLSN-I, but given the peak absolute magnitude of $M_r \sim -21.3$, we adopt an SLSN-I classification. We include photometry from ZTF and ATLAS. We assign a silver label given the lack of photometry before peak. We include our own Binospec spectrum from Gomez et al. (2020c).

B32 CSS160710

CSS160710:160420+392813 (= MLS160616:160420+392813) was discovered by the CRTS and classified as an SLSN-I by Drake et al. (2016). We include photometry from the CRTS and MLS, and our own PSF photometry of Las Cumbres GSP images. We assign a silver label given there is only one band of photometry available.

B33 LSQ14an

LSQ14an was classified as an SLSN-I by Inserra et al. (2017). We include photometry from Inserra et al. (2017). Additionally, we include our own PSF photometry of Las Cumbres GSP images after doing difference imaging to subtract the host flux. We assign a silver label given the lack of photometry before peak. We include one spectrum from Inserra et al. (2017).

B34 PTF10bfz

PTF10bfz was discovered by PTF and classified as an SLSN-I by Quimby et al. (2018). Perley et al. (2016) found an associated host galaxy at a redshift of $z = 0.1701$. We include photometry from De Cia et al. (2018), which the authors correct for extinction using $E(B-V) = 0.016$. The spectra from Quimby et al. (2018) show a systematic blueshift of $\sim 12\,000$ km s^{-1} that might be the result of an asymmetrical explosion or a viewing angle effect. We assign a silver label given the lack of photometry before peak. We include one spectrum from Quimby et al. (2018).

B35 2016els

SN 2016els (= PS16dnq) was classified as an SLSN-I by Fraser et al. (2016) and Mattila et al. (2016). We include PS1 photometry and UVOT photometry from the SOUSA archive. There is no photometry available before peak. We assign a silver label given the lack of photometry before peak. We include one spectrum from Fraser et al. (2016), obtained from WISeREP.

B36 2016wi

SN 2016wi (=PS16yj = iPTF15esb) was classified as an SLSN-I by Yan et al. (2017b). We include photometry from PS1 and Yan et al. (2017b). The light curve shows three distinct bumps at early times, which we include in the MOSFIT fit. We assign a silver label given the lack of photometry before peak. We include one spectrum from Fraser et al. (2016), obtained from WISeREP.

B37 2018gkz

SN 2018gkz (=ZTF18abvgjyl = PS18ced) was discovered by ZTF and classified as an SLSN-I by Yan (2020). We include photometry from PS1 and Chen et al. (2023a), in addition to our own PSF photometry of ZTF images after doing difference imaging to subtract the host flux. We assign a silver label given the lack of photometry before peak. We include one spectrum from Fremling et al. (2018d), obtained from the TNS.

B38 iPTF16bad

iPTF16bad was classified as an SLSN-I by Yan et al. (2017b). Gal-Yam (2019a) show that iPTF16bad lacks hydrogen at early times, but that tentative hydrogen features emerge at late times. We include photometry from Yan et al. (2017b). We assign a silver label given the lack of photometry before peak. We include one spectrum from Fraser et al. (2016).

B39 2018fd

We classified SN 2018fd (=ZTF18accdszm = PS18df = MLS171011: 091036 + 354318), originally discovered by CRTS, as an SLSN-I as part of FLEET (Gomez et al. 2021a). We find a redshift of $z = 0.263$ based on host emission lines. We include CRTS C-band photometry, but do not subtract any host galaxy contribution from the CRTS photometry since the host galaxy contribution should be minimal given its magnitude of $m_r = 22.13$ mag. We include our own PSF photometry of FLWO images after doing difference imaging to subtract the host flux. There is no photometry before peak. We assign a silver label given the lack of photometry before peak. We include our own spectrum from Binospec (Gomez et al. 2021a).

B40 PS113gt

PS1-13gt (= PSc480107) was discovered by MDS and classified as an SLSN-I by Lunnan et al. (2014) and presented in Lunnan et al. (2018c). We include photometry from Lunnan et al. (2018c), who correct the photometry for extinction. This SN shows signs of reddening, since it has a red continuum and O II features that require high temperatures (Lunnan et al. 2018c). There is no photometry at or before peak. The SN was reported as a spectroscopically classified SLSN-I as part of the PS1 MDS (Hosseinzadeh et al. 2020; Villar et al. 2020). We assign a silver label given the lack of photometry before peak. We include one spectrum from Lunnan et al. (2018c).

B41 DES16C2nm

DES16C2nm was discovered by DES and classified as an SLSN-I by Smith et al. (2018) and presented as a 'gold' SLSN-I at a very high redshift of $z = 1.998$ by Angus et al. (2019). We include photometry form Angus et al. (2019). We assign a silver label given the lack of photometry before peak. We include one spectrum from Angus et al. (2019).

B42 2011kf

SN 2011kf (= CSS111230:143658+163057) was originally classified as an SLSN-I by Prieto et al. (2012). A detailed study of the SN was presented in Inserra et al. (2013). We include photometry from Inserra et al. (2013), which does not have the host contribution subtracted, but we conclude this should be negligible. There is no photometry available before peak. We assign a silver label given the lack of photometry before peak. We include one spectrum from Inserra et al. (2013), obtained from WISeREP.

B43 PS112bmy

PS1-12bmy (= PSc440420) was discovered by MDS and classified as an SLSN-I by Lunnan et al. (2014) and presented in Lunnan et al. (2018c). We include photometry from Lunnan et al. (2018c), who correct the photometry for extinction. There is no photometry available before peak. The SN was reported as a spectroscopically classified SLSN-I as part of the PS1 MDS (Hosseinzadeh et al. 2020; Villar et al. 2020). We assign a silver label given that there are no data before peak. We include one spectrum from Lunnan et al. (2018c).

B44 PS111bam

PS1-11bam (= PSc330114) was discovered by MDS and classified as an SLSN-I by Berger et al. (2012) and presented in Lunnan et al. (2018c). We include photometry from Lunnan et al. (2018c), which the authors correct for extinction. The SN was reported as a spectroscopically classified SLSN-I as part of the PS1 MDS (Hosseinzadeh et al. 2020; Villar et al. 2020). We assign a silver label given the lack of photometry before peak. We include one spectrum from Berger et al. (2012).

B45 1999as

SN 1999as was classified as an SN Ia by Knop et al. (1999), but the authors noted that the source was blue, with broad absorption features, and about 2 mag brighter than a typical SN Ia. The source was later presented in Deng et al. (2001) as the most LSN discovered at the time. Hatano et al. (2001) classified SN 1999as as a Type Ic hypernova. Moriya et al. (2019) finally present a comparison between SN 1999as and SN 2007bi, and classify SN 1999as as an SLSN-I. We assign a silver label given the lack of data before peak. We include photometry and one spectrum from Kasen (2004).

B46 2002gh

SN 2002gh was discovered by Cartier et al. (2022) two decades after the actual SN explosion. The authors classify the object as one of the most luminous SLSN-I ever discovered with $M_V = -22.4$ mag. Although we note that given the high redshift of $z = 0.3653$, applying an additional cosmological K-correction of $+\ (2.5 \times \log(1 + z))$ brings the peak magnitude down to a less extreme value of $M_V = -22.2$ mag. We include photometry from Cartier et al. (2022). We assign a silver label given the lack of data before peak. We include one spectrum from Cartier et al. (2022).

B47 iPTF13bjz

iPTF13bjz was discovered by PTF and classified as an SLSN-I by De Cia et al. (2018). We include photometry from De Cia et al. (2018), which the authors correct for extinction using $E(B - V) = 0.019$. We assign a silver label given that the light curve only has r-band data and no data during the decline. We include one spectrum from Schulze et al. (2021).

B48 PS110ahf

PS1-10ahf (= PSc080079) was discovered by MDS and classified as an SLSN-I by McCrum et al. (2015) and presented in Lunnan et al. (2018c). We include photometry from Lunnan et al. (2018c), who correct the photometry for extinction. Even though McCrum et al. (2015) present late-time data, these are not included since they are not corrected for the flux contribution of the host. There are two late-time detections that appear to suggest a second peak in the light curve. The spectrum shows some significant absorption bluewards of ∼ 2800Å. The SN was reported as a spectroscopically classified SLSN-I as part of the PS1 MDS (Hosseinzadeh et al. 2020; Villar et al. 2020). We assign a silver label given the lack of photometry after peak. We include one spectrum from McCrum et al. (2015).

B49 2017beq

SN 2017beq (=PS17bek = iPTF17beq) was classified as an SLSN-I by Gal-Yam et al. (2017), the authors provide two points of photometry. We include an additional data point from Cikota et al. (2018). We assign a silver label since there are only a total of three photometry points available. We include one spectrum, obtained from WISeREP.

B50 2018lzw

SN 2018lzw (= ZTF18abrzcbp) was discovered by ZTF and classified as an SLSN-I by Chen et al. (2023a), Yan, Schulze & ZTF SLSN group (2022b). We include photometry from Chen et al. (2023a), ATLAS, and our own upper limits from pre-explosion ZTF images. We assign a silver spectrum since there is no data during the rise. We include one spectrum from Chen et al. (2023a).

B51 PTF10aagc

PTF10aagc was discovered by PTF and classified as an SLSN-I by Quimby et al. (2018). Perley et al. (2016) found an associated host galaxy at a redshift of $z = 0.206$. We include photometry from De Cia et al. (2018), which the authors correct for extinction using $E(B - V) = 0.023$. The spectra from Quimby et al. (2018) shows hydrogen and helium, but the spectrum does not look like an SLSN-II. Yan et al. (2015) suggest PTF10aagc is an SLSN-I with ejecta that interacts with an H-rich CSM at late times. We assign a silver label given the spectral uncertainties. We include one spectrum from Quimby et al. (2018).

B52 2020abjx

SN 2020abjx (=ZTF20aceicyy = ATLAS20bfww) was discovered by ZTF and classified as an SLSN-I by Yan et al. (2020a). At the reported redshift of $z = 0.39$, the peak magnitude of the SN is $M_r = -22.3$, comfortably in the SLSN-I regime. Nevertheless, we assign a silver label given the single noisy available spectrum. We include photometry from ZTF and ATLAS, as well as our own PSF photometry of LDSS3C images. We include our own spectrum from Binospec.

B53 2021rwz

SN 2021rwz (=ZTF21abezyhr =PS21hfp = ATLAS21tkh) was discovered by ZTF and classified as a SLSN-I by Weil et al. (2021c) and Weil & Milisavljevic (2021). We include photometry from ZTF, ATLAS, and PS1. Additionally, we include our own PSF photometry of FLWO images. We assign a silver label given the highly noisy single spectrum available from Weil & Milisavljevic (2021).

B54 2017hbx

SN 2017hbx (= Gaia17cna) was discovered by *Gaia* and classified as an SN Ic by Neill (2017). We include photometry from GSA, and upper limits from ATLAS. The redshift of $z = 0.1652$ reported by Neill (2017) is accurate to ∼ 0.02. The spectrum is consistent with either an SLSN-I or an SN Ic, but we assign a SLSN-I classification given the peak absolute magnitude of $M_G \sim -21.3$. We assign a silver label given the uncertain redshift. We include one spectrum from Neill (2017).

B55 iPTF13dcc

iPTF13dcc (= CSS130912:025702−001844) was classified as an SLSN-I by Vreeswijk et al. (2017). We include photometry from Vreeswijk et al. (2017). The light curve shows a flat profile at early time which is hard to fit with our current model. The authors explain the complex light-curve structure by invoking CSM interaction, as did Liu et al. (2018a). We assign a silver label given the lack of photometry before peak. We include one spectrum from Schulze et al. (2021), obtained from WISeREP.

B56 2022aawb

SN 2022aawb (= ZTF22abvcnnl) was discovered by ZTF and classified as an SLSN-I by Poidevin et al. (2022c, d). We include data from ATLAS and ZTF. We include one spectrum from Poidevin et al. (2022c), obtained from the TNS. We assign a silver label given the very low S/N spectrum.

B57 2022gyv

SN 2022gyv (=ZTF22aadqgoa = PS22diw) was classified as an SLSN-I by Poidevin et al. (2022b). We include photometry from ATLAS, ZTF, and PS1. We exclude the first i-band detection from the MOSFIT fits since this is well before the nominal SN explosion. We assign a silver label given the slightly uncertain redshift measurement of $z = 0.38 - 0.40$. We include one spectrum from Poidevin et al. (2022b).

B58 DES14C1fi

DES14C1fi was discovered by DES and classified as a 'silver' SLSN-I by Angus et al. (2019). We include photometry and one spectrum from Angus et al. (2019).

B59 DES14E2slp

DES14E2slp was discovered by DES and classified as a 'silver' SLSN-I by Angus et al. (2019). We include photometry and one spectrum from Angus et al. (2019).

B60 2019aamw

SN 2019aamw (= ZTF19acujvsi) was discovered by ZTF and classified as an SLSN-I by Chen et al. (2023a). We include photometry from Chen et al. (2023a) and ATLAS. We assign a silver label given the very noisy spectra available. We include one spectrum from Chen et al. (2023a).

B61 DES15S1nog

DES15S1nog was discovered by DES and classified as a 'silver' SLSN-I by Angus et al. (2019) and as a possible SLSN-I by Casas et al. (2016). We include photometry and one spectrum from Angus et al. (2019).

B62 DES17C3gyp

DES17C3gyp was discovered by DES and classified as a 'silver' SLSN-I by Angus et al. (2019). We include photometry from Angus et al. (2019). We exclude the two detections before MJD = 58100 from the MOSFIT fit, since these are much earlier than the nominal explosion date. We include one spectrum from Angus et al. (2019).

B63 iPTF13bdl

iPTF13bdl was discovered by PTF and classified as an SLSN-I by De Cia et al. (2018). We include photometry from De Cia et al. (2018), which the authors correct for extinction using $E(B - V) = 0.042$. The light curve shows a large scatter, making it hard to constrain its physical parameters. We assign a silver label given the uncertain light curve. We include one spectrum from De Cia et al. (2018).

B64 2020fyq

SN 2020fyq (=ZTF20aapaecd = PS20arv = ATLAS20kwv) was discovered by ZTF and classified as a SLSN-I by Chen et al. (2023a). We include photometry from Chen et al. (2023a), PS1, and ATLAS. We assign a silver label given the similarly to LSNe given the peak magnitude of $M_r \sim -19.9$ and spectrum consistent with an SN Ic. We include one spectrum from Chen et al. (2023a).

B65 PS111tt

PS1-11tt (= PSc150381) was discovered by MDS and classified as an SLSN-I by Lunnan et al. (2014) and presented in McCrum et al. (2015). The latter authors provide photometry corrected for extinction. The first data point might be indicative of a precursor according to Lunnan et al. (2018c). We assign a silver label since there is only one spectrum available of the source with low S/N with significant absorption bluewards of ~ 2800 Å, nevertheless this is consistent with an SLSN-I. The SN was reported as a spectroscopically classified SLSN-I as part of the PS1 MDS (Hosseinzadeh et al. 2020; Villar et al. 2020). We include one spectrum from Lunnan et al. (2018c).

B66 SNLS07D3bs

SNLS-07D3bs was classified as an uncertain SLSN-I by Prajs et al. (2017), given the low S/N spectrum used for classification. At the redshift of $z = 0.757$ provided by Fremling et al. (2018c), the peak magnitude of the SN is $M_r \sim -21.1$, within the SLSN-I regime. The spectra of the source are not available for download and only late-time spectra exist, hence the silver label.

B67 2020onb

We classified SN 2020onb (=ZTF20abjwjrx = Gaia20dub = ATLAS20bkdh), originally discovered by ZTF, as an SLSN-I as part of FLEET (Gomez et al. 2020c). We determined a redshift of $z = 0.153$ based on host galaxy emission lines. We include photometry from ATLAS, GSA, and Chen et al. (2023a). The spectra at early times are significantly redder than normal SLSN-I. It is possible the spectra are heavily reddened by extinction in the host galaxy, hence why we assign a silver label. We include our own Binospec spectrum from Gomez et al. (2020c).

B68 DES16C3ggu

DES16C3ggu was discovered by DES and classified as a 'gold' SLSN-I by Angus et al. (2019). We include DES photometry from Angus et al. (2019). We exclude the first g-band point before MJD = 57740 from the MOSFIT fit, since this is well before the expected SN explosion. We assign a silver label given the lack of photometry after peak. We include one spectrum from Angus et al. (2019).

B69 PTF10nmn

PTF10nmn was discovered by PTF and classified as an SLSN-I by Quimby et al. (2018). Perley et al. (2016) found an associated host galaxy at a redshift of $z = 0.1237$. We include photometry from De Cia et al. (2018), which the authors correct for extinction using $E(B - V) = 0.14$. We assign a silver label given the very sparse photometry. We include one spectrum from Quimby et al. (2018).

B70 iPTF13cjq

iPTF13cjq was discovered by PTF and classified as an SLSN-I by De Cia et al. (2018). At the reported redshift of $z = 0.3962$, the peak magnitude of the SN is $M_r = -21.6$, in the SLSN-I regime. We include photometry from De Cia et al. (2018), which the authors correct for extinction using $E(B - V) = 0.042$. The light curve has peculiar flat early-time photometry with no data before the peak. Therefore, we assign a silver label. We include one spectrum from Schulze et al. (2021), obtained from WISeREP.

B71 iPTF16asu

We presented iPTF16asu as an SLSN-like LSN in Gomez et al. (2022a). The SN was originally classified by Whitesides et al. (2017) and presented in Taddia et al. (2019). We assign a silver label given that this is a LSN. We include one spectrum from Taddia et al. (2019).

APPENDIX C: 'BRONZE' SUPERLUMINOUS SUPERNOVAE

C1 1999bz

SN 1999bz (= AAVSO 1359+69) was classified as an SN Ic by Berlind, Calkins & Jha (1999). We adopt a redshift of $z = 0.0846$, established from a spectrum of the host galaxy by Kirshner et al. (1983). At this redshift, the peak magnitude of the SN is $M_C \sim -20.4$, within the range of SLSN-I. We include a single unfiltered photometry point from Pearce, Napoleao & Baransky (1999) and assume an uncertainty of 0.1 mag. We assign a bronze label given the near total absence of photometry and single noisy spectrum available.

C2 2011ep

SN 2011ep (= CSS110414:170342+324553) was discovered by the CRTS and classified as an SN Ic-BL by Graham et al. (2011a) and as an SN Ic by Graham et al. (2011b). Given the peak absolute magnitude of $M_C \sim -21.9$, the transient instead might be an SLSN-I. An analysis of the host galaxy of SN 2011ep was presented in Schulze et al. (2018), who also considered SN 2011ep to be a likely SLSN-I. Nevertheless, there are no public spectra of the source and we are unable to confirm this classification, hence the bronze label. We include photometry from CRTS, without subtracting any host flux, since we find this to be negligible.

C3 2014bl

SN 2014bl (= PSN J13253881+2557339) was discovered by the CRTS and discovered by Li et al. (2014a, b) and classified as a Type Ic SN at a $z = 0.0377$. The SN is somewhat luminous with a peak magnitude of $M \sim -19$. There is only one spectrum with low S/N of uncertain classification. The photometry is only from CRTS, which we correct for extinction using $E(B - V) = 0.0152$. We subtract a nominal host magnitude of $m_C = 19.36$ from all photometry. We assign a bronze label given the sparse photometry and uncertain spectral classification.

C4 2018jfo

SN 2018jfo (=ZTF18achdidy = MLS181220:112339+255952) was discovered by ZTF and classified as an SLSN-I by Fremling et al. (2019c). The authors report a redshift of $z = 0.163$, which makes the peak magnitude of the SN $M_r \sim -20.8$, within the range of SLSN-I. Nevertheless, we assign a bronze label since there are no public spectra of the source and we are unable to confirm this classification. We include photometry from CRTS, ATLAS, and our own PSF photometry from ZTF images.

C5 2018fcg

SN 2018fcg (=ZTF18abmasep =Gaia18cms = ATLAS18ucc) was discovered by ZTF and classified as an SLSN-I by Fremling et al. (2018a) and Lunnan et al. (2018a). We presented SN 2018fcg as a Ic-like LSN in Gomez et al. (2022a). We include additional photometry from Chen et al. (2023a). We assign a bronze label given that SN 2018fcg most closely resembles a Type Ic SN.

C6 2018hsf

SN 2018hsf (=ZTF18acbvpzj = ATLAS18yer) was discovered by ZTF and classified as an SN Ic-BL by Fremling et al. (2018f). We include photometry from ZTF and ATLAS, plus our own PSF photometry of ZTF images after subtracting the host. At the quoted redshift of $z = 0.119$, the peak absolute magnitude is $M_r \sim -19.8$, within the range of SLSNe. Nevertheless, the source has no public spectra and we therefore assign a bronze label.

C7 2019une

We classified SN 2019une (=ZTF19acmbjmp =ATLAS19balq = PS20bus), originally discovered by ZTF, as an SLSN-I as part of FLEET. We include photometry from ATLAS, ZTF, PS1, and our own PSF photometry of FLWO images after doing difference imaging to subtract the host flux. Even though the spectrum resembles that of an SLSN-I, the redshift is too uncertain to provide a confident classification, and we therefore assign a bronze label.

C8 2020aewh

SN 2020aewh (= ZTF20acwmyzx) was discovered by ZTF and originally classified as an SLSN-I by Yan et al. (2023) with a detailed study presented in Yan et al. (2021). We include photometry from ATLAS and ZTF, as well as one late-time detection from PSF photometry of IMACS images. Nevertheless, we assign a bronze label given that there are no public spectra of the source.

C9 2021uvy

SN 2021uvy was discovered by ZTF and classified as an SLSN-I by Poidevin et al. (2021), as an SN Ib/c by Ridley et al. (2021), and as a peculiar SN Ib by Chu et al. (2021b). We presented SN 2021uvy as a Ic-like LSN in Gomez et al. (2022a). We assign a bronze label given the spectra most closely resembles a Type Ic SN. We include additional photometry from ATLAS. We exclude detections after MJD = 59476 due to a very prominent secondary peak.

C10 2020wfh

SN 2020wfh (=ZTF20acitbmf =PS20kqu = ATLAS20bdjz) was discovered by ZTF and classified as a SLSN-I by Yan et al. (2020a). At the reported redshift of $z = 0.33$, the peak magnitude of the SN is $M_r = -22.1$, in the SLSN-I regime. Nevertheless, we assign a bronze label since there are no public spectra of the source and we are unable to confirm this classification. We include photometry from PS1 and ATLAS, as well as our own PSF photometry of FLWO and ZTF images after subtracting the host contribution.

C11 2021ybf

SN 2021ybf was discovered by ZTF and classified as an SLSN-I by Bruch et al. (2021). We presented SN 2021ybf as a Ic-like LSN in Gomez et al. (2022a). We assign a bronze label given the spectra most closely resembles a Type Ic SN. We include additional photometry from ATLAS.

C12 2022ojm

SN 2022ojm (= ZTF22aapjqpn) was discovered by ZTF and classified as an SLSN-I by Perez-Fournon et al. (2022). We include photometry from ZTF and ATLAS. We assign a bronze label given the very uncertain redshift estimate of either $z \sim 0.28$ to ~ 0.48.

C13 PSNJ000123

PSN J000123+000504 was discovered by Kostrzewa-Rutkowska et al. (2013) and classified as a possible SLSN-I based on the light curve alone. We assign a bronze label given that there is no spectra from the supernova. We include photometry from Kostrzewa-Rutkowska et al. (2013), which the authors correct for extinction.

C14 CSS140925

CSS140925:005854+181322 was discovered by the CRTS and classified as a Type I by Campbell et al. (2014), and the host galaxy study presented in Schulze et al. (2018) as an SLSN-I. Based on the reported redshift of $z = 0.46$, the peak absolute magnitude of the SN is $M_C = -23.12$. Nevertheless, there are no public spectra of the source and we are unable to confirm this classification. We include photometry from the CRTS and Las Cumbres GSP. Given the lack of spectra and sparse photometry we assign a bronze label.

C15 ASASSN15no

ASASSN-15no was discovered by ASAS-SN and presented in Benetti et al. (2018) as an SN with features of SLSN-I, normal SNe Ib/c, but also signs of interaction, such as hydrogen emission lines. The nature of this source appears very distinct from normal SLSNe, and we therefore assign a bronze label.

C16 DES16C3cv

DES16C3cv was discovered by DES and classified as a 'silver' SLSN-I by Angus et al. (2019). We presented DES16C3cv as a Ic-like LSN in Gomez et al. (2022a) at a redshift of $z = 0.727$. We assign a bronze label given the spectra and light curve most closely resemble a Type Ic SN.

C17 LSQ14fxj

LSQ14fxj was classified as an SLSN-I by Smith et al. (2014), with an erratum from Galbany et al. (2014). Margutti et al. (2018) present *Swift*–X-ray Telescope (XRT) observations of the source, which are all upper limits. The light curve has very sparse optical data with only one detection from Galbany et al. (2014), which is why we assign a bronze label. We include one spectrum from WISeREP.

C18 MLS121104

MLS121104:021643+204009 (= LSQ12fzb) was discovered by the CRTS and classified as an SN SLSN-Ic by Fatkhullin & Gabdeev (2012) and later classified as an SLSN-I by Lunnan et al. (2014). Nevertheless, there are no public spectra of the source, so we are unable to confirm this classification. There is only one epoch of photometry from the CRTS. Given the lack of spectra and photometry, we assign a bronze label.

C19 PS112zn

PS1-12zn (= PSc380044) was included in the SLSN-I host galaxy sample of Lunnan et al. (2014). However, Lunnan et al. (2018c) later excluded it from their sample since the SN spectrum lacks the O II and broad UV features typical in SLSNe. Since the spectrum does not cover Hα, the authors cannot rule out a hydrogen-rich event. We therefore assign a bronze label. At the given redshift, the peak magnitude of the is $M_r \sim -21.0$, consistent with an SLSN. We include photometry from Hosseinzadeh et al. (2020) and Villar et al. (2020), excluding data before MJD = 56010, before the nominal SN explosion.

C20 SDSS17789

SDSS-II SN 17789 was classified as an SLSN by Sako et al. (2018) as part of the SDSS-II Supernova Survey. The authors do not specify if the source is hydrogen rich or poor, and there is no public spectra of the source. We include photometry from Sako et al. (2018). Given the lack of public information on the source, we assign a bronze label.

C21 UID30901

UID30901 was presented in Hueichapan et al. (2022) as an SLSN-I discovered in the UltraVISTA survey. We include photometry from Hueichapan et al. (2022). Nevertheless, we assign a bronze label since there are no spectra of the SN or the host galaxy.

C22 SN1000

SN1000+0216 was classified as an SLSN-I by Cooke et al. (2012). Given that the SN was discovered only after stacking long baselines of photometry, only a late-time spectrum exists, which makes it hard to verify the SLSN nature of the source and we assign a bronze label.

The peak absolute magnitude of $M_r \sim -21.6$ is within the SLSN range. We include photometry from Cooke et al. (2012).

C23 SN2213

SN2213−1745 was classified as an SLSN-I by Cooke et al. (2012). Given that the SN was discovered only after stacking long baselines of photometry, only a late-time spectrum exists, which makes it hard to verify the SLSN nature of the source and we assign a bronze label. The peak absolute magnitude of $M_r \sim -21.1$ is within the SLSN range. We include photometry from Cooke et al. (2012).

APPENDIX D: NOT SUPERLUMINOUS SUPERNOVAE

D1 2009bh

SN 2009bh (= PTF09q) was classified as a possible SLSN-I by Quimby et al. (2018) and as an SN Ic by Kasliwal et al. (2009). The peak absolute magnitude of $M_R \sim -18.6$ is not consistent with being an SLSN-I. Moreover, there is only one photometry data point publicly available.

D2 2019fiy

SN 2019fiy (=ZTF19aauiref = PS19agg) was classified as an SLSN-I by Yan et al. (2019b) and Perley et al. (2019c), as well as included in the SLSN-I sample from Chen et al. (2023a). Yan et al. (2019b) claim a tentative redshift of $z = 0.67$ due to the low S/N spectrum, but also find a match to lower redshift SNe. A redshift of $z = 0.67$ would make SN 2019fiy the most luminous SLSN-I ever discovered by a large margin, we find a spectral match to an SN Ia at $z \sim 0.13 - 0.14$, a much more likely redshift and classification.

D3 2019hcc

SN 2019hcc (=Gaia19cdu = ATLAS19mgw) was classified as an SLSN-I by Frohmaier et al. (2019). However, the peak absolute magnitude of the SN is ~ -17.7, much too faint to be consistent with an SLSN. The source has since been reclassified as a Type II SN (Inserra et al., in preparation).

D4 2021ahpl

SN 2021ahpl (=ZTF21aalkhot =Gaia22asc =PS22bca = ATLAS22fga) was classified as an SLSN-I by Smith et al. (2022). We include photometry from ZTF, GSA, PS1, and ATLAS. And our own PSF photometry from FLWO and Las Cumbres GSP images. We exclude three possibly spurious detections from ZTF and GSA $sim400$ d before explosion. Nevertheless, the peak absolute magnitude of this SN is $M_r \sim -19.7$ and the spectrum does not resemble a normal SLSN, and we therefore argue this is likely a transient of a different nature.

D5 2020jhm

SN 2020jhm (=ZTF20aayprqz =PS20dfm = ATLAS20luz) was classified as an SLSN-I at a redshift of $z = 0.06$ by Perley et al. (2020b), which would make the SN peak magnitude $M_r = -20.3$. Instead, we find a good spectral match to an SN Ia at $z = 0.05$, with a corresponding peak magnitude of $M_r = -19.9$, within the typical magnitudes of SNe Ia. The light curve also appears very similar to typical SNe Ia.

D6 2022aig

SN 2022aig (=ZTF22aaagqvw = ATLAS22cpm) was classified as a relatively luminous SN Ic at a redshift of $z = 0.4$ by Aamer et al. (2022). Nevertheless, we determine a redshift of $z = 0.31$ from host emission lines in a late-time LDSS3C spectrum. At this redshift, the peak magnitude is $M_r \sim -18.9$ and therefore no longer superluminous.

D7 2022csn

SN 2022csn (=ZTF22aabimec =Gaia22ayp =PS22bju = ATLAS22ggz) was classified as an SLSN-I by Srivastav et al. (2022a, b), but later reclassified as a TDE by Arcavi & Pellegrino (2022). We update the redshift of $z = 0.15$ quoted by Srivastav et al. (2022a) to $z = 0.147$, determined from narrow host emission lines from our own late-time Binospec spectrum.

D8 2022czy

SN 2022czy (=PS22bvf = ATLAS22gtw) was classified as an SLSN-I by Fulton et al. (2022a, b) and Hinkle (2022), but later reclassified as a TDE by Blanchard et al. (2022a, b) on the basis of a broad Hα emission component.

D9 2022vxc

SN 2022vxc (=ZTF22abcvfgs =Gaia22ebz = PS22kdy) was classified as an SLSN-I by Harvey et al. (2022a, b). We include photometry from ZTF, ATLAS, *Gaia*, and PS1, and our own PSF photometry of FLWO and Las Cumbres GSP images. The light curve of SN 2022vxc shows a peculiar triangular-shape, which we are unable to reproduce using standard models. While this object has a spectrum consistent with an SLSN interpretation, its light-curve nature is too distinct to be considered within the standard SLSN population. We include one spectrum from Harvey et al. (2022a), obtained from the TNS.

D10 PTF11mnb

PTF11mnb was classified as a possible SLSN-I by Quimby et al. (2018) since the spectra are consistent with both an SLSN-I or a SN Ic. The source was presented in a detailed study by Taddia et al. (2018), who conclude this is an SN Ic, a 2005bf analogue with a double-peaked light curve. The peak absolute magnitude of $M_r \sim -18.5$ is most consistent with the SN Ic interpretation.

This paper has been typeset from a TEX/LATEX file prepared by the author.